Max-Planck-Institut
für Meteorologie

MAX-PLANCK-GESELLSCHAFT

Evaluation of the tropospheric chemistry general circulation model ECHAM5–MOZ and its application to the analysis of the chemical composition of the troposphere with an emphasis on the late RETRO period 1990–2000

Sebastian Rast et al.

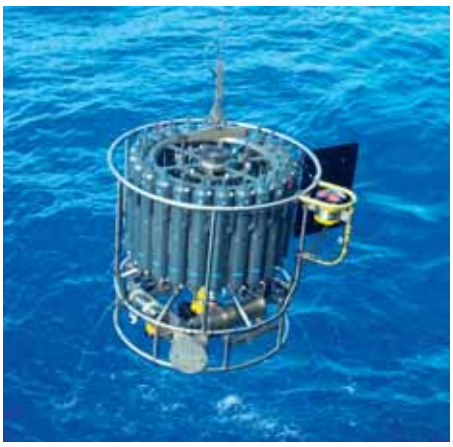

Berichte zur Erdsystemforschung 114
2014

Reports on Earth System Science

Hinweis

Die Berichte zur Erdsystemforschung werden vom Max-Planck-Institut für Meteorologie in Hamburg in unregelmäßiger Abfolge herausgegeben.

Sie enthalten wissenschaftliche und technische Beiträge, inklusive Dissertationen.

Die Beiträge geben nicht notwendigerweise die Auffassung des Instituts wieder.

Die "Berichte zur Erdsystemforschung" führen die vorherigen Reihen "Reports" und "Examensarbeiten" weiter.

Notice

The Reports on Earth System Science are published by the Max Planck Institute for Meteorology in Hamburg. They appear in irregular intervals.

They contain scientific and technical contributions, including Ph. D. theses.

The Reports do not necessarily reflect the opinion of the Institute.

The "Reports on Earth System Science" continue the former "Reports" and "Examensarbeiten" of the Max Planck Institute.

Anschrift / Address

Max-Planck-Institut für Meteorologie
Bundesstrasse 53
20146 Hamburg
Deutschland

Tel.: +49-(0)40-4 11 73-0
Fax: +49-(0)40-4 11 73-298
Web: www.mpimet.mpg.de

Layout:

Bettina Diallo, PR & Grafik

Titelfotos:
vorne:
Christian Klepp - Jochem Marotzke - Christian Klepp
hinten:
Clotilde Dubois - Christian Klepp - Katsumasa Tanaka

Berichte zur Erdsystemforschung 114 2014

Evaluation of the tropospheric chemistry general circulation model ECHAM5–MOZ and its application to the analysis of the chemical composition of the troposphere with an emphasis on the late RETRO period 1990–2000

Sebastian Rast et al.

Hamburg 2014

Reports on Earth System Science 114 2014

ISSN 1614-1199

Evaluation of the tropospheric chemistry general circulation model ECHAM5–MOZ and its application to the analysis of the chemical composition of the troposphere with an emphasis on the late RETRO period 1990–2000

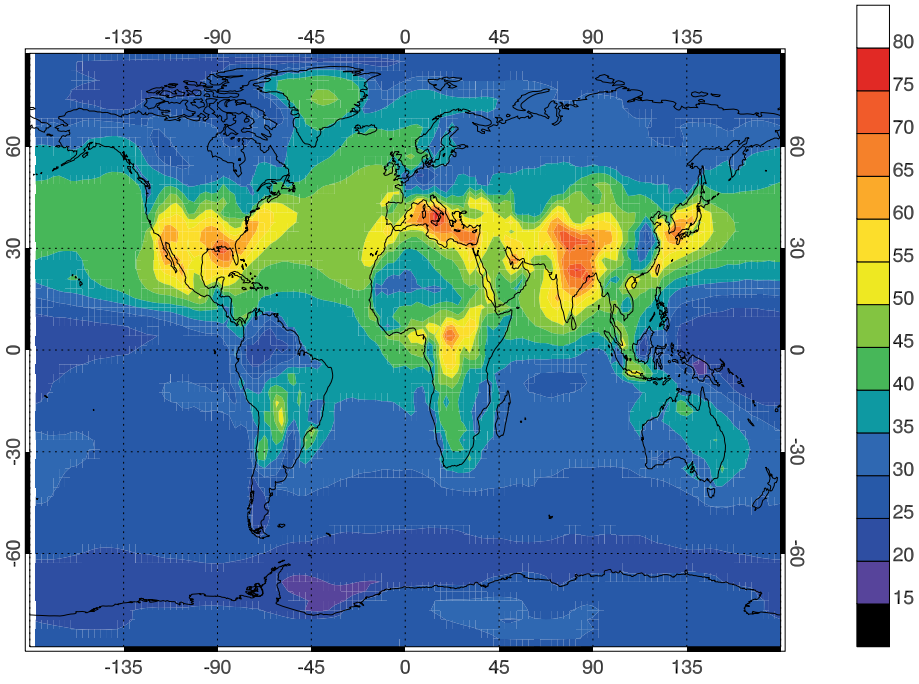

Sebastian Rast et al.

Hamburg 2014

Evaluation of the tropospheric chemistry general circulation model ECHAM5–MOZ and its application to the analysis of the chemical composition of the troposphere with an emphasis on the late RETRO period 1990–2000

S. Rast[1], M.G. Schultz[2], I. Bey[3], T. van Noije[4], A.M. Aghedo[5], G.P. Brasseur[6], T. Diehl[7], M. Esch[1], L. Ganzeveld[8], I. Kirchner[9], L. Kornblueh[1], A. Rhodin[10], E. Roeckner[1], H. Schmidt[1], S. Schröder[2], U. Schulzweida[1], P. Stier[11], K. Thomas[2], S. Walters[12]

[1] Max Planck Institute for Meteorology, Hamburg, Germany

[2] ICG-2, Research Centre Jülich, Germany

[3] Center for Climate Systems Modeling (C2SM), ETH Zürich, Switzerland

[4] Royal Netherlands Meteorological Institute (KNMI), De Bilt, The Netherlands

[5] former member of Max Planck Institute for Meteorology, Hamburg, Germany

[6] Climate Service Center, Hamburg, Germany

[7] Goddard Earth Sciences and Technology Center, University of Maryland Baltimore County, Baltimore, USA

[8] Centre for Water and Climate, Wageningen University, Wageningen, The Netherlands,

[9] Institute for Meteorology, Freie Universität Berlin, Berlin, Germany,

[10] Deutscher Wetterdienst, Offenbach, Germany

[11] Atmospheric, Oceanic and Planetary Physics, Department of Physics, University of Oxford, Oxford, UK

[12] NCAR, Boulder, Colorado, USA,

May 20, 2014

Abstract

The Tropospheric Chemistry General Circulation model ECHAM5-MOZ was developed between 2001 and 2005 and was used to investigate the variability and trends of ozone, CO and NO_x in the second half of the 20th century in the framework of the RETRO project. The multi–decadal simulation of the period of 1960 to 2000 was one of the first of that kind. The model captures many features of the seasonal cycle and vertical gradients of trace gas concentrations measured on the ground or from balloons, aircraft or satellite. We diagnose a significant high bias in the simulated ozone concentrations in the 1990s, which can in part be attributed to an overestimated stratosphere troposphere exchange and possibly underestimated dry deposition of ozone. Wintertime CO concentrations in the northern hemisphere are underestimated by up to 30%. The observed interannual variability of the tropospheric NO_2 column, surface CO concentrations and ozone is generally captured by the simulation, but the model fails to capture the surface ozone increase observed at several stations around the world during the 1980s and 1990s. The increase in the tropospheric ozone column between the 1960s and 1990s is consistent with model simulations of preindustrial conditions. The global ozone burden and chemical formation and loss are continuously rising during the entire 41-year simulation period. The dry deposition flux increases until the early 1980s and shows a more irregular behavior afterwards. Until around 1980 regionally averaged precursor emissions correlate well with surface ozone changes. Thereafter, the emission trend in Europe and North America is reversed, while ozone levels remain high. Asian emissions and ozone concentrations continue to rise, but the slope of the correlation changes.

1 Introduction

This paper describes and evaluates the chemistry general circulation model ECHAM5-MOZ including the emission data sets which were developed in the REanalysis of the TROpospheric composition over the past 40 years (RETRO) project. ECHAM5-MOZ is based on the ECHAM5 general circulation model (*Roeckner et al.*, 2003) complemented by the chemistry module MOZART version 2 (*Horowitz et al.*, 2003). While the coupling between climate and chemistry has been accounted for in many stratospheric models (cf. *Eyring et al.*, 2005, and references therein), there are (situation of 2008) fewer models which include a fully interactive coupling of the climate system with tropospheric chemistry (*Feichter et al.*, 1996; *Roelofs et al.*, 1997; *Mickley et al.*, 1999; *Shindell et al.*, 2001a,b; *Liao et al.*, 2003; *Hauglustaine et al.*, 2004; *Stier et al.*, 2005; *Jöckel et al.*, 2006; *Pozzoli et al.*, 2008a). In our implementation, changes in the trace gas composition of the atmosphere do not influence the general circulation. Consequently, studies of effects of climate change on the trace gas composition can be performed without the simulation of large ensembles.

The RETRO (REanalysis of the TROpospheric chemical composition over the last 40 years) project had as objective to analyse and interprete the long–term trends and interannual variability of the chemical composition of the troposphere. ECHAM5-MOZ was among the three complex global chemistry transport models participating in this modeling effort. Together with a second model, it was the only one simulating the whole period of 40 years.

Of the short-lived gaseous species that may affect climate, tropospheric ozone is the most important one. For example, tropospheric ozone contributes directly to the greenhouse effect and is estimated to have caused a radiative forcing of about 30% of that of CO_2 since the beginning of the industrial era (*IPCC*, 2007, chapter 2, p. 136). In addition, tropospheric ozone has major impacts on human health, ecosystems, and the agricultural production (*Chen et al.*, 2008; *Wang et al.*, 2004; *Fuhrer et al.*, 1997, and references therein). Thus, reliable estimates of future ozone levels contribute to make the climate prediction more accurate and to assess the effect of climate change on ecosystems and public health.

While the quantitative understanding of the global tropospheric ozone budget has improved significantly over the last decade (cf. the recent multi-model studies performed by *Stevenson et al.* (2006); *Fiore et al.* (2009); *Wild* (2007); *Wu et al.* (2007)), less is known about the processes that control the interannual variability and trends of surface ozone concentrations (*Schultz et al.*, 2007; *Koumoutsaris et al.*, 2008; *Parrish et al.*, 2012, 2013; *Schultz et al.*, 2011).

The paper is organized as follows. In section 2, we provide a description of the ECHAM5-MOZ model and the simulation set-up. Section 3 contains a description of the emission data sets used in this study. In section 4 we summarize our model evaluation with emphasis on the 1990s where most observations are available. Section 5 discusses the simulated variability of tropospheric ozone and its precursor species and includes an analysis of the global budgets of ozone and OH. We relate the simulated ozone trend and variability to the changes in emissions and discuss some aspects of the uncertainties in these emissions. The final section contains the conclusions.

Although the whole RETRO period from 1960 to 2000 was simulated with ECHAM5-MOZ, the evaluation is based on the period after 1990 for which the measurements and emissions are considered to be the most accurate. In the trend analysis, we use longer time periods. The model was constrained to observed temperature, pressure, divergence, and vorticity in order to reduce the effect of differences in trace gas species transport on species concentration between simulation and observation at synoptic scale.

2 Model Description and Simulation Set-up

The tropospheric chemistry general circulation model ECHAM5-MOZ was developed between 2001 and 2005 on the basis of the general circulation model ECHAM5 (version 5.3.02) (*Roeckner et al.*, 2003, 2006; *Hagemann et al.*, 2005) and the MOZART version 2.4 chemistry transport model (*Horowitz et al.*, 2003). The model was developed as part of the European research project REanalysis of the TROpospheric composition over the past 40 years (RETRO). It is part of the Hamburg Earth System Model version 1 which includes additional feedback processes with the aerosol system (*Stier et al.*, 2005)(ECHAM5-HAMMOZ: *Pozzoli et al.* (2008a,b)) and the terrestrial and marine biosphere *Kloster et al.* (e.g. 2007).

The simulation described in this paper constitutes one of three multi-decadal global simulations performed in the framework of this project. The other two simulations were run with the LMDz-INCA model (*Hauglustaine et al.*, 2004; *Folberth et al.*, 2006) and the TM (*Heimann*, 1995) version 4, respectively. Selected results from this model were already published elsewhere (*Stevenson et al.*, 2006; *Dentener et al.*, 2006a,b; *Shindell et al.*, 2006; *Auvray et al.*, 2007; *Aghedo et al.*, 2007; *Pozzoli et al.*, 2008a,b), no detailed model description and evaluation has been available until now.

This section provides a general overview about the model components and describes the setup of the model simulation. Details of the parameterizations can be found in section A. Additional information on the emission inventories is given in section B.

The dynamical core of ECHAM5 solves the prognostic equations for divergence, vorticity, temperature, and the logarithm of the surface pressure in the spectral space. Physical processes as advection of tracers and water vapor, convective and stratiform clouds, vertical diffusion, radiation and chemistry are calculated on an associated gaussian grid. For the simulations described in this paper, the model resolution was T42 (triangular spectral truncation at wave number 42) and the associated gaussian grid corresponds to a resolution of approximately $2.8° \times 2.8°$. The vertical coordinate system is a hybrid sigma-pressure system with 31 vertical levels, the highest level being at 10 hPa. The model time step was 20 minutes.

The chemical mechanism with 63 transported species and 168 reactions and the backward Eulerian solver are adopted from the MOZART 2.4 model as described by *Horowitz et al.* (2003). The photolysis rates are computed by interpolation from a multivariate table that was originally provided by the use of the Tropospheric Ultraviolet and Visible radiation model (TUV, version 3.0) (*Madronich et al.*, 1998). The cloud effects on photolysis rates are taken into account by the use of a correction factor as proposed by *Brasseur et al.* (1998), but the ozone column above does not depend on the year. The heterogeneous reaction of N_2O_5 on sulfate aerosols is included using the same aerosol distribution of *Tie et al.* (2001) and a reaction probability $\gamma = 0.04$ (*Tie et al.*, 2003) for all years. The parameterizations of lightning NO_x and dry and wet deposition were taken from other sources (*Grewe et al.*, 2001; *Ganzeveld et al.*, 1995; *Stier et al.*, 2005, respectively) with some modifications as described in section A. Upper boundary conditions for O_3, NO_x, HNO_3 and N_2O_5 are prescribed via relaxation to monthly mean zonal climatologies as in MOZART and did not vary with the years.

In order to reproduce the actual weather in the past 40 years as accurately as possible, we applied a relaxation technique (*Jeuken et al.*, 1996; *Machenhauer et al.*, unknown year) (see also section A.3) to constrain temperature, vorticity, divergence, surface pressure and sea surface temperature to the archived fields from the European Centre for Medium Range Weather Forecast (ECMWF) 40-year reanalysis (ERA-40) (*Uppala et al.*, 2005). The model simulations analyzed below were run as a 41-year continuous simulation with a 5-year spin-up phase starting nominally in 1955 but using repeated meteorological fields for 1959 and emissions for the year 1960.

3 Emissions

Tables 1 – 3 summarize the global annual mean emissions for every decade of the model simulations described in this study. Most of the emission data are from the RETRO inventories for anthropogenic and vegetation fire emissions (*Pulles et al.*, 2007; *Endresen et al.*, 2003; *Grewe et al.*, 2002; *Schultz et al.*, 2008a). Interactively computed emissions from the terrestrial vegetation and from lightning are also included. The former are calculated with version 1 of the model of emissions of gases and aerosols from nature (MEGAN) (*Guenther et al.*, 2006) and the latter are computed with the parametrization of *Grewe et al.* (2001). Natural (soil) NO_x emissions are from the ORCHIDEE model described by *Lathière et al.* (2006); *Lathière* (2002), while soil and ocean CO emissions are from the Global Emissions Inventory Activity (GEIA) version 1 data set as used by *Horowitz et al.* (2003). Methane emissions were obtained from P. Bergamaschi (personal communication, 2004). We do not list these as they only serve to create a spatial pattern near the surface. Methane concentrations in the model are constrained with a zonal mean surface climatology in the planetary boundary layer. Hydrogen emissions were obtained by linear scaling of the carbon monoxide emissions using the emission factors given by *Novelli et al.* (1999) and *Andreae et al.* (2001) for anthropogenic, natural and vegetation fire emissions, respectively. Global H_2 emissions range from 20 Tg in 1960 to 35 Tg in 1997. The maximum in 1997 is related to the extensive vegetation fires in Indonesia.

Most emissions were applied as a flux condition at the surface in the diffusion equation, but biomass burning, aircraft, and lightning emissions are distributed according to prescribed height profiles (*Lamarque et al.*, 2010; *Schultz et al.*, 2008a). More detailed information on the emission inventories and parameterizations used in this study can be found in section B, the RETRO project report (*RETRO-1.6*, 2007), available on http://retro.enes.org/pub_reports.shtml[1], and the article by *Schultz et al.* (2008a).

Global annual NO_x emissions from all industrial and residential sectors were 27.29 Tg(N) in 1990, including 2.99 Tg(N) from international ship traffic and 0.49 Tg(N) from aircraft (Table 1). These values are similar to the emissions of the MOZART2 model (24.36 Tg(N), *Horowitz et al.* (2003)) and they also agree well with the 1990 data from the EDGAR 3.2 inventory (*Olivier et al.*, 2000) (26.17, 2.61 and 0.57 Tg(N), for land surface, ship and aircraft emissions, respectively). However, the regional and sectoral distribution of these emissions differ between the three data sets. Average NO_x emissions from vegetation fires between 1985 and 1995 were 5.00 Tg(N) with a minimum of 3.78 Tg(N) in 1988 and a maximum of 6.87 Tg(N) in 1992. *Horowitz et al.* (2003) list 9.81 Tg(N) and EDGAR 3.2 gives 4.04 Tg(N). Biogenic NO_x emissions in RETRO are larger than those applied by *Horowitz et al.* (2003) (9.4 versus 6.6 Tg(N)) due to the use of a different data source. Changes in fertilizer-induced NO_x release were not taken into account in the RETRO simulations.

Global NO_x emissions peaked around 1990 and remained relatively constant since then. While the emissions in Europe and North America tended to decrease after 1990, they experienced a continuous rise on the other continents, most notably in Asia (see discussion on regional changes in section 6). The RETRO inventory suggests that NO_x emissions almost doubled between 1960 and the year 2000, and most of the increase occurred before 1980, i.e. before the wide-spread introduction of catalysts in cars.

Global carbon monoxide emissions follow a similar pattern as the NO_x emissions but show much less of a trend (the interannual variability of CO emissions is larger, because of the greater contribution from biomass burning). According to the RETRO inventory, the change in global CO emissions between 1960 and 2000 was about 20 %. Industrial and residential activities accounted for 534 Tg(CO) in 1990, while vegetation fires were estimated as 452 Tg(CO). The first value is in very close agreement with EDGAR 3.2 (532 Tg(CO)) and about 5 % lower than the estimate of *Horowitz et al.* (2003). Vegetation fire emissions in EDGAR 3.2 are substantially

[1]last accessed 2014-05-08

Table 1: Global emissions of NO_x from the RETRO emissions inventories. Lightning emissions are computed interactively in the ECHAM5-MOZ model, biogenic emissions from *Lathière et al.* (2006). Units are Tg(N)/year.

Sector	1960	1970	1980	1990	2000
Industrial combustion	1.68	2.43	3.21	3.13	2.84
Power generation	2.58	4.31	5.41	6.53	8.13
Residential combustion	1.45	2.13	3.24	3.69	3.31
Surface traffic	4.23	7.28	9.97	10.46	9.66
International ship traffic	1.44	2.57	3.12	2.99	3.53
Aircraft	0.02	0.07	0.24	0.49	0.72
Vegetation fires	4.87	5.62	5.89	6.04	5.05
Biogenic	9.36	9.34	9.36	9.34	9.36
Lightning	3.50	3.43	3.72	3.69	3.50
Total	25.61	33.69	40.19	42.18	41.87

Table 2: Global emissions of carbon monoxide from the RETRO emissions inventories. Natural emissions are from GEIA version 1 and from MEGAN. Units are Tg(CO)/year.

Sector	1960	1970	1980	1990	2000
Industrial combustion	1.9	2.3	2.8	2.8	2.2
Power generation	0.7	1.1	1.5	1.9	2.3
Residential combustion	185.3	201.3	241.1	283.8	279.6
Surface traffic	131.0	212.1	249.0	244.6	191.9
International ship traffic	0.4	0.8	1.0	0.9	1.1
Vegetation fires	316.1	363.9	405.4	425.2	358.9
Vegetation, soil and ocean	278.2	274.9	277.8	276.5	277.6
Total	913.6	1056.4	1178.6	1235.7	1113.6

less than RETRO (307 Tg(CO)), while those of MOZART2 were slightly larger (486.6 Tg(CO)). Natural emissions of CO include emissions from soils, vegetation and oceans. Terrestrial emissions were adopted from *Müller* (1992) (160 Tg(CO)), while ocean emissions were estimated as 20 Tg(CO) based on discussions with GEIA colleagues and similar to *Horowitz et al.* (2003). Due to an error in the simulation setup, vegetation emissions of CO calculated by the MEGAN model (mean of 97 Tg/yr) were applied on top of these prescribed emissions.

The RETRO emissions of non-methane volatile organic compounds are dominated by the emissions from the terrestrial vegetation. There is no significant trend of these emissions over the 41-year period considered in this study (see Fig. 23). On average, isoprene emissions contribute 429 Tg(C) per year and monoterpene emissions contribute 155 Tg(C) per year. The remaining part consists of 105 Tg(C) methanol, 27 Tg(C) acetaldehyde, 14 Tg(C) formaldehyde, 19 Tg(C) acetone and 20 Tg(C) alkanes and alkenes. *Guenther et al.* (2006) give a range of 440–660 Tg(C) for global isoprene emissions. The RETRO values are close to the lower end of this range. Industrial and residential non methane volatile organic compounds (NMVOC) emissions in 1990 add up to 123 Tg(C), which is close to the EDGAR3.2 estimate of 131 Tg(C), but a factor of 3 larger than the value of *Horowitz et al.* (2003) (45.2 Tg(C)). The NMVOC vegetation fire emissions listed in Table 3 contain only the compounds which were used in the chemical mechanism. These emissions were derived from the individual compound emission factors of *Andreae et al.* (2001). According to their compilation of emission factors from field and chamber measurements, the sum of NMVOC emissions from the ECHAM5-MOZ compounds is between 40 % and 45 % of the total NMVOC mass emitted, depending on the vegetation class. While this might lead to

Table 3: Global emissions of non methane volatile organic compounds from the RETRO emissions inventories. Biogenic emissions were calculated in the ECHAM5-MOZ model with the MEGAN module. Units are Tg(C)/year.

Sector	1960	1970	1980	1990	2000
Industrial combustion	0.19	0.23	0.35	0.38	0.34
Power generation	0.08	0.12	0.16	0.22	0.29
Extraction of fossil fuels	2.10	3.33	6.34	7.25	8.97
Residential combustion	12.43	12.53	15.43	18.16	18.39
Surface traffic	23.84	35.80	39.48	32.85	20.56
International ship traffic	< 2	< 2	< 2	< 2	< 2
Solvent use	14.04	17.76	23.67	30.31	31.22
Waste treatment and disposal	19.68	23.13	27.87	32.42	35.39
Vegetation fires	29.13	33.69	38.57	40.79	34.48
Biogenic	771.91	746.42	774.84	763.02	772.66
Total	873.20	872.78	926.36	925.01	921.95

underestimated chemical CO production from the degradation of these hydrocarbons, this effect is considered minor, partly because several of the hydrocarbon species not accounted for in this study will rapidly form soluble species which can condensate on smoke aerosols and are thus inactive with respect to the tropospheric ozone chemistry. The amount of NMVOC emissions from vegetation fires in the RETRO inventory is similar to the value of *Horowitz et al.* (2003) (47.3 Tg(C)) and again larger than the EDGAR3.2 estimate of 22 Tg(C) for 1990.

4 Model results for the 1990s

4.1 Overview

Figure 1 displays the yearly average of the surface ozone volume mixing ratio for 2000. Compared to the model ensemble mean analysed by *Dentener et al.* (2006a) (hereinafter: D2006) our simulation shows a similar spatial pattern but overall higher ozone concentrations. We find a mean volume mixing ratio of 38.5 ppbv (D2006: 33.7 ppbv) in the northern hemisphere and 36.4 ppbv (D2006: 23.7 ppbv) in the southern hemisphere. The model ensemble average obtained in D2006 agrees with observations within 5 ppbv in the United States, China, and Central Europe but has a positive bias of 10-15 ppbv over Africa, India and the Mediterranean. These are also the regions where ECHAM5-MOZ exhibits the largest bias. The reason for this bias is not clear but a combination of inaccuracies in the description of the boundary layer dynamics and too high biogenic emissions may be at the origin of this problem. The ozone trend at the surface in the 1990ies is a consequence of the increasing emissions of ozone precursers (Southern and Eastern Asia) but also of trends in fire and biogenic emissions. The latter depend on temperature and increase in a warmer climate.

The monthly mean CO volume mixing ratio at 500 hPa presented in Figure 2 exhibits higher values than the model ensemble average analysed by *Shindell et al.* (2006) and is therefore more similar to the MOPITT retrieval. Nevertheless, the CO volume mixing ratio is too low over the North Atlantic and parts of Asia in April. On the other hand, *Emmons et al.* (2004) report a high bias of up to 20% of the MOPITT data in regions with generally low CO concentration in the lower troposphere explaining thus a part of the difference between simulation and satellite retrieval. The volume mixing ratio maximum over Africa is shifted to the South in our simulation compared to the satellite retrieval and the outflow from Africa seems to be very strong in the model. In October, the maximum of the CO volume mixing ratio over Africa is located too far

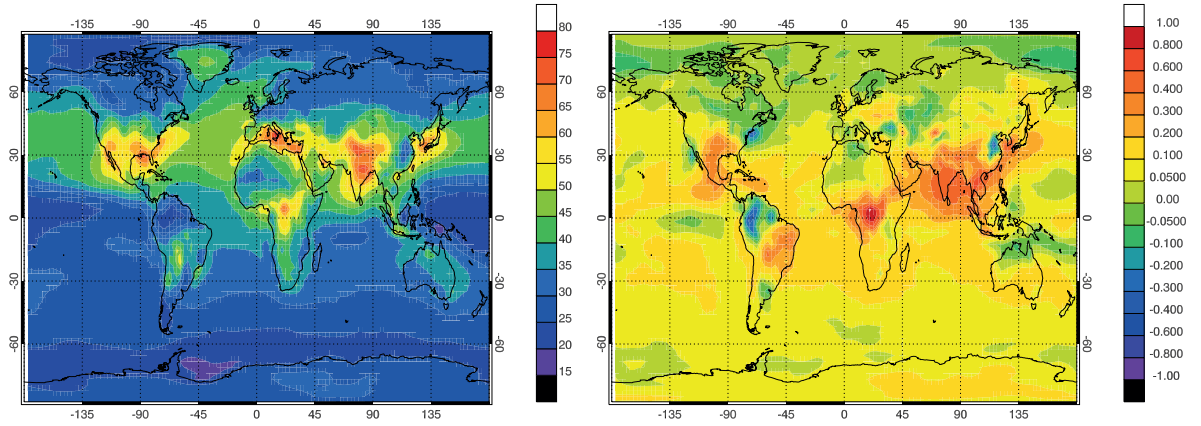

Figure 1: Mean surface volume mixing ratio in ppbv of ozone for 2000 (left), and its linear trend for the 1990ies in ppbv/year calculated from monthly mean ozone volume mixing ratios (right).

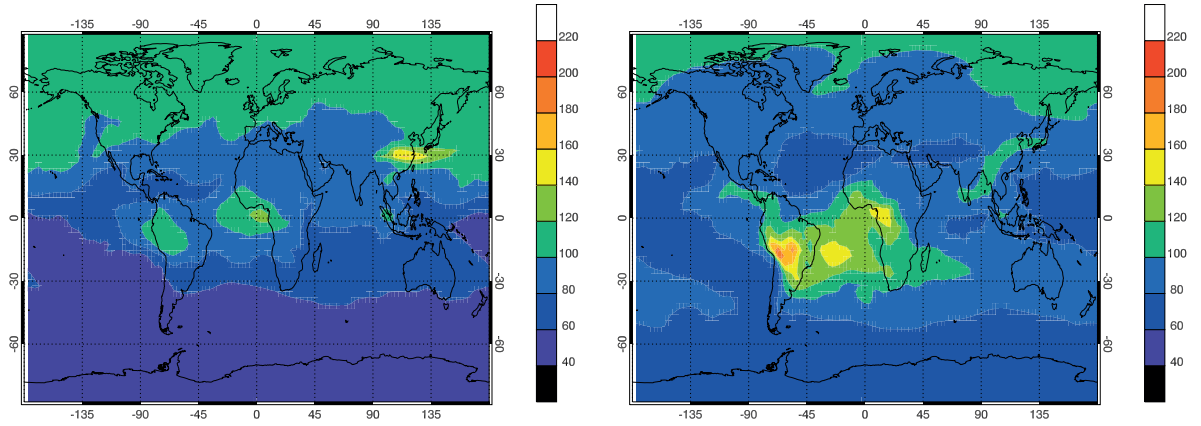

Figure 2: Mean volume mixing ratio of CO in ppbv at 500 hPa for April 2000 (left) and October 2000 (right).

in the North and a third local maximum appears over the South Atlantic which is not present in the MOPITT retrieval. The CO volume mixing ratio maximum over South America is shifted southward compared to the satellite retrieval. Again, our simulation results are closer to the observations than the multi-model mean in the northern hemisphere in terms of the spatial volume mixing ratio patterns.

4.2 Carbon monoxide

We compare our simulation results to the CO measurements made by the Earth System Research Laboratory Global Monitoring Division (ESRL-GMD, formerly CMDL)(*Novelli et al.*, 1998). Our comparison is based on the monthly mean values reported by the ESRL-GMD and only includes measurements under base line conditions. For the model evaluation we computed for each station the mean bias, the modified normalized mean bias (MNMB) and the Pearson correlation coefficient R^2 for all years where both observations and model data are available. The MNMB of model values $f = (f_i)_{i=1,N}$ and observations $o = (o_i)_{i=1,N}$ both being larger than 0 is defined as:

$$\mathrm{MNMB}(f,o) = \frac{1}{N}\sum_{i=1}^{N}(f_i - o_i)/(f_i + o_i) \tag{1}$$

It relates the difference between each pair of simulated and observed values to their mean.

Table 4: Geographic location and data availability of surface CO measurements within the NOAA ESRL GMD network. We report also the modified normalized mean bias (MNMB, eq. 1), the relative bias, and the Pearson correlation all calculated from monthly mean values.

Station	location	measurement period (missing period)	MNMB	rel. bias	r^2
Alert	82.45°N 297.48°E 210m	1992/4 - 2000/12	−0.11	−0.18	0.61
Baltic Sea	55.42°N 17.07°E 28m	1992/8 - 2000/12 (1995/4 - 1995/6)	0.0	0.02	0.12
Cape Meares	45.48°N 236.03°E 30m	1992/1 - 1998/3	0.09	0.26	0.0
Terceira Island	38.77°N 332.63°E 40m	1994/10 - 2000/12	−0.10	−0.17	0.53
Sede Boker	31.13°N 34.88°E 400m	1995/12 - 2000/12	−0.12	−0.20	0.29
Sand Island	28.21°N 182.62°E 7m	1992/1 - 2000/12	−0.13	−0.22	0.80
Mauna Loa	19.53°N 204.42°E 3397m	1990/1 - 2000/12	−0.10	−0.17	0.53
Cape Kumukahi	19.52°N 205.18°E 3m	1990/1 - 2000/12	−0.12	−0.2	0.71
Mahe Island	4.67°S 55.17°E 7m	1990/11 - 2000/12 (1994/3 - 1994/6) (2000/9 - 2000/10)	0.0	0.01	0.69
Easter Island	27.15°S 250.55°E 50m	1994/1 - 2000/12	−0.02	−0.03	0.73
Cape Grim	40.68°S 144.68°N 94m	1991/6 - 2000/12	0.13	0.32	0.63
South Pole	89.98°S 335.20°E 2810m	1993/4 - 2000/12	0.09	0.20	0.91

The MNMB is antisymmetric with respect to a permutation of simulated values f_i and their observed counterparts o_i. There is no factor 2 in eq. (1) in order to confine the MNMB between -1 and 1. However, the observation are considered to be free of any bias. Consequently, our analysis will mostly be based on the relative bias of the model results with respect to the observations.

The results for 12 selected stations are reported in Tab. 4. We chose the stations in order to cover both, northern and southern hemisphere. The interannual variability will be discussed in section 5.1.

The absolute value of the relative bias does not exceed 0.32 for the stations reported in Tab. 4. From the low relative bias of −0.034 calculated over all 12 stations listed in Tab. 4, we conclude that the average global surface volume mixing ratio of CO is rather well captured by the model. Nevertheless, regional and seasonal deviations indicate that the emissions and the transport is not always correctly described in this simulation.

Fig. 3 shows the latitudinal distribution of the climatological averages from the model and the observations for all 47 stations for February in which the highest CO volume mixing ratios occur in the northern hemisphere and for August in which the lowest values are observed. In February, the CO volume mixing ratio of the simulation and the measurements agrees very well in the southern hemisphere, but is too low by about 28% in the northern hemisphere. In August, the simulation overestimates the CO volume mixing ratio in the southern hemisphere by 27%, but exhibits a good agreement in the northern hemisphere. The overestimate at Cape Grim and South Pole is likely a result of an error in the simulation setup (see section 3). We show the mean seasonal cycle of the CO concentration at the stations listed in Tab. 4 in Fig. 4.

We find that the CO volume mixing ratio at high latitude stations is underestimated by up to 30% in January-June (e.g. Alert). The seasonal cycle has a lower amplitude in the simulation and shows the summer minimum of CO concentration too early in the year (Alert, Baltic Sea, Cape Meares, Terceira Island, Sede Boker, to a lesser extent this also applies to the other stations in the northern hemisphere). The underprediction of CO in the northern hemisphere during spring is a known problem in many global chemistry transport model simulations *Horowitz et al.* (e.g. 2003); *Shindell et al.* (e.g. 2006). In the original MOZART model, the underestimation of the CO mole fraction in spring is less pronounced but a considerable overestimation of nearly 50%

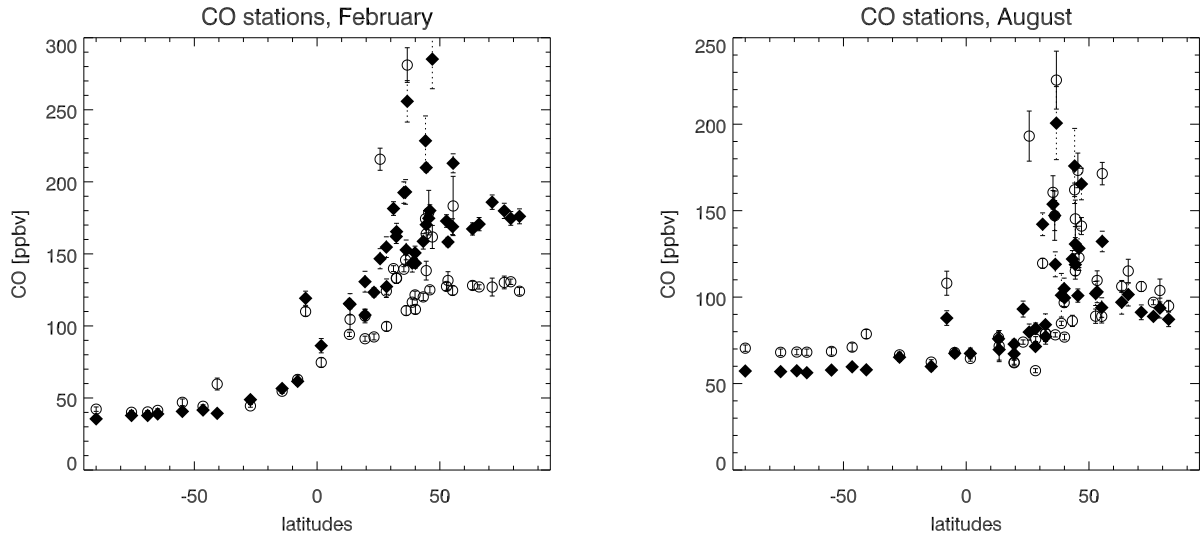

Figure 3: Latitudinal distribution of the climatological average of the CO volume mixing ratio for February (left) and August (right). Simulation result: open circles; CMDL measurements: filled diamonds. Error bars denote the one-σ standard deviation.

is seen in autumn (September to November). Such an overestimation during autumn is not apparent in our simulation for the northern hemispheric stations. CO concentrations in the Southern hemisphere are well reproduced by ECHAM5-MOZ ($r^2 \geq 0.63$, see Table 4).

We conclude that the interhemispheric gradient of CO volume mixing ratios is too weak near the surface in our model and that the seasonal cycle has a too low amplitude.

There are indications that emissions of biogenic volatile organic compounds (VOC) which are precursors of CO are biased high in MEGAN version 1. A sensitivity study without biogenic emissions led to an excellent agreement of CO volume mixing ratios in the southern hemisphere.

We compare vertical CO profiles averaged over various regions from aircraft measurements (cf. *Emmons et al.*, 2000) with their simulated counterparts (see Figs. 5, 6 and Fig. 26 of the Appendix C). The field campaigns usually cover a period of one or two months, albeit the actual period of measurements in some of the regions may be much shorter. We compare the measurements over the period from 1988 to 1999 to simulated monthly means averaged over the 10-year period 1991-2000 as well as to simulated monthly means for the specific year of the individual aircraft experiment. The largest deviations of the model values from the measurement is found in regions which are close to the emission sources. In particular, the bias is up to 72 % in the case of the TRACE-A campaign at the Brazilian coast and Africa in the biomass burning outflow regions. The outflow from the Asian continent is overestimated near the coast of Japan during PEM-West-A (1991) but it is underestimated over the China Sea during PEM-West-B (1994) by -42 %. This may be a direct consequence of an underestimation of both anthropogenic and biomass burning emissions over East Asia for the later period as previously suggested by *Pozzoli et al.* (2008a). Observed CO concentrations are well reproduced by the simulation in the northern latitudes (e.g. ABLE campaigns in the early 1990s) and the underestimation seems to be restricted to high latitudes in winter.

We did not perform a detailed comparison of the model results with CO retrievals from the MOPITT instrument, but we demonstrated that our model has higher CO volume mixing ratios than the mean of the models used in the analysis by *Shindell et al.* (2006) at 500 hPa and is therefore closer to the retrieval than the mean model.

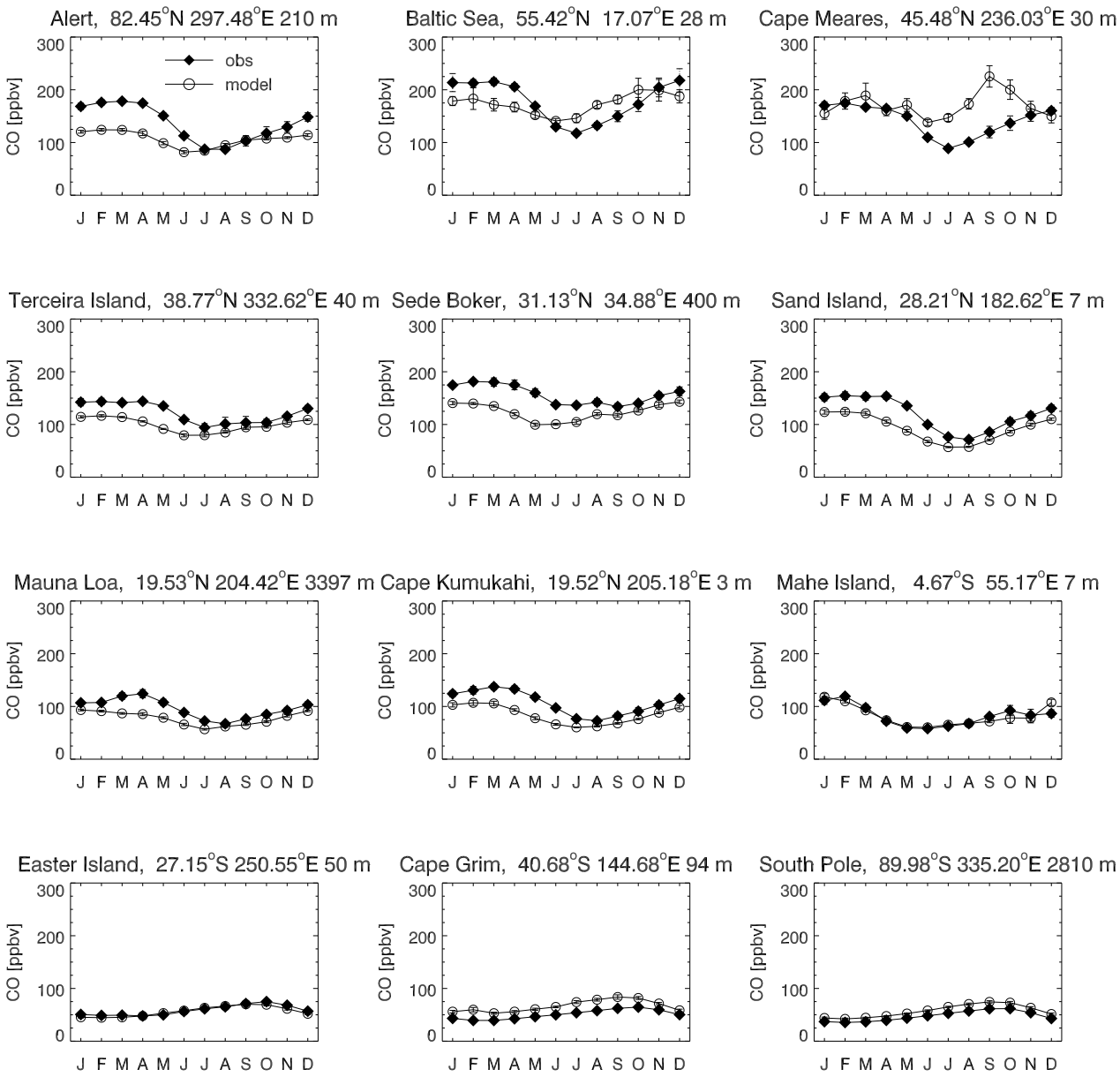

Figure 4: Comparison of the mean seasonal cycle of CO measured at various locations of the NOAA ESRL-GMD measurement network (*Novelli et al.*, 1998) and the simulated mean seasonal cycle over the years with measurements (see Table 4 for the exact months and years for each station). Simulation result: open circles; CMDL measurements: filled diamonds.

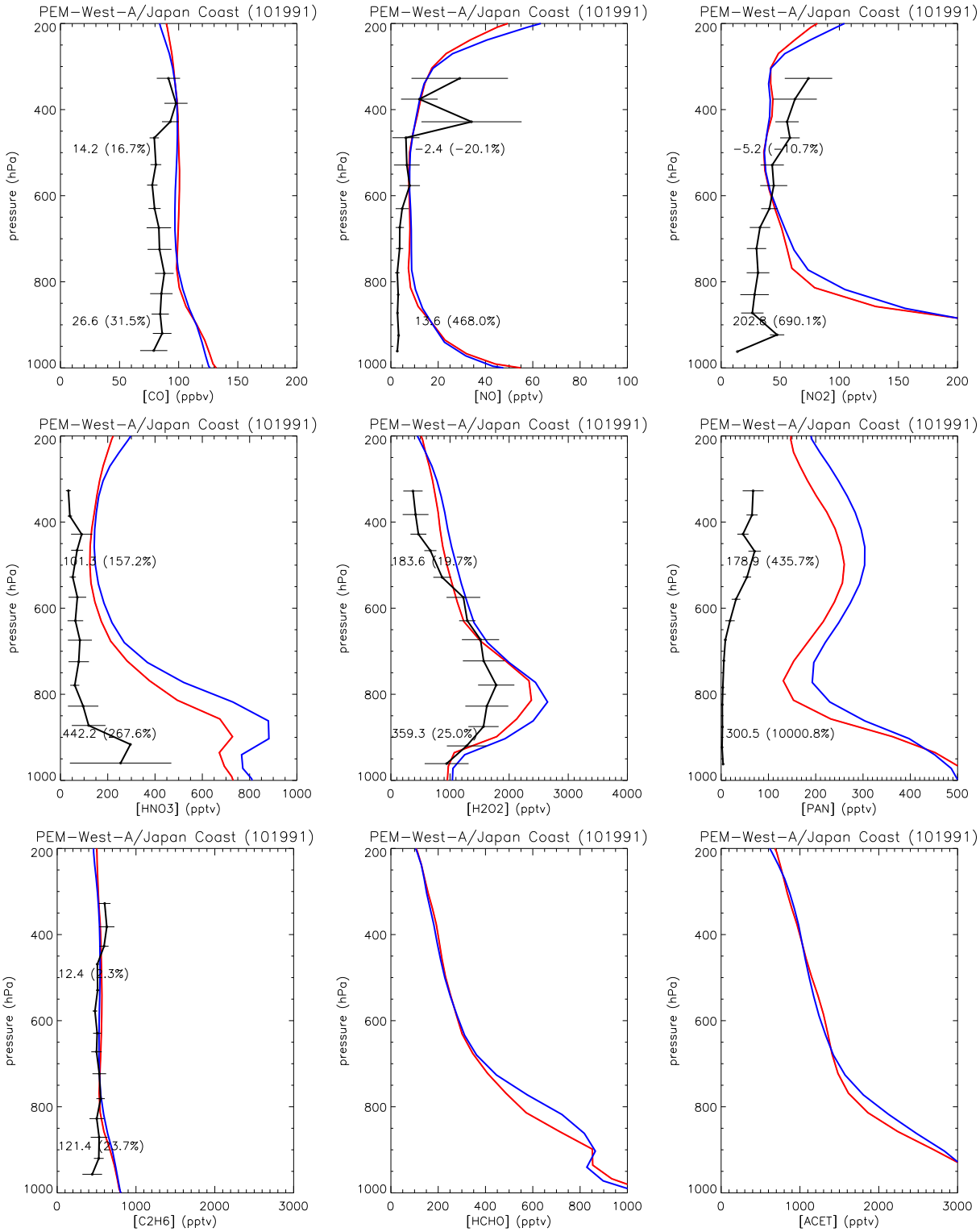

Figure 5: Vertical profiles of the PEM-West-A region for various species. Aircraft measurements: Black line with error bars, simulated 10-year monthly mean (red), monthly mean of specific year of campaign (blue). The numbers in the indiviual panels give the absolute and relative biases at the respective altitudes compared to the red line.

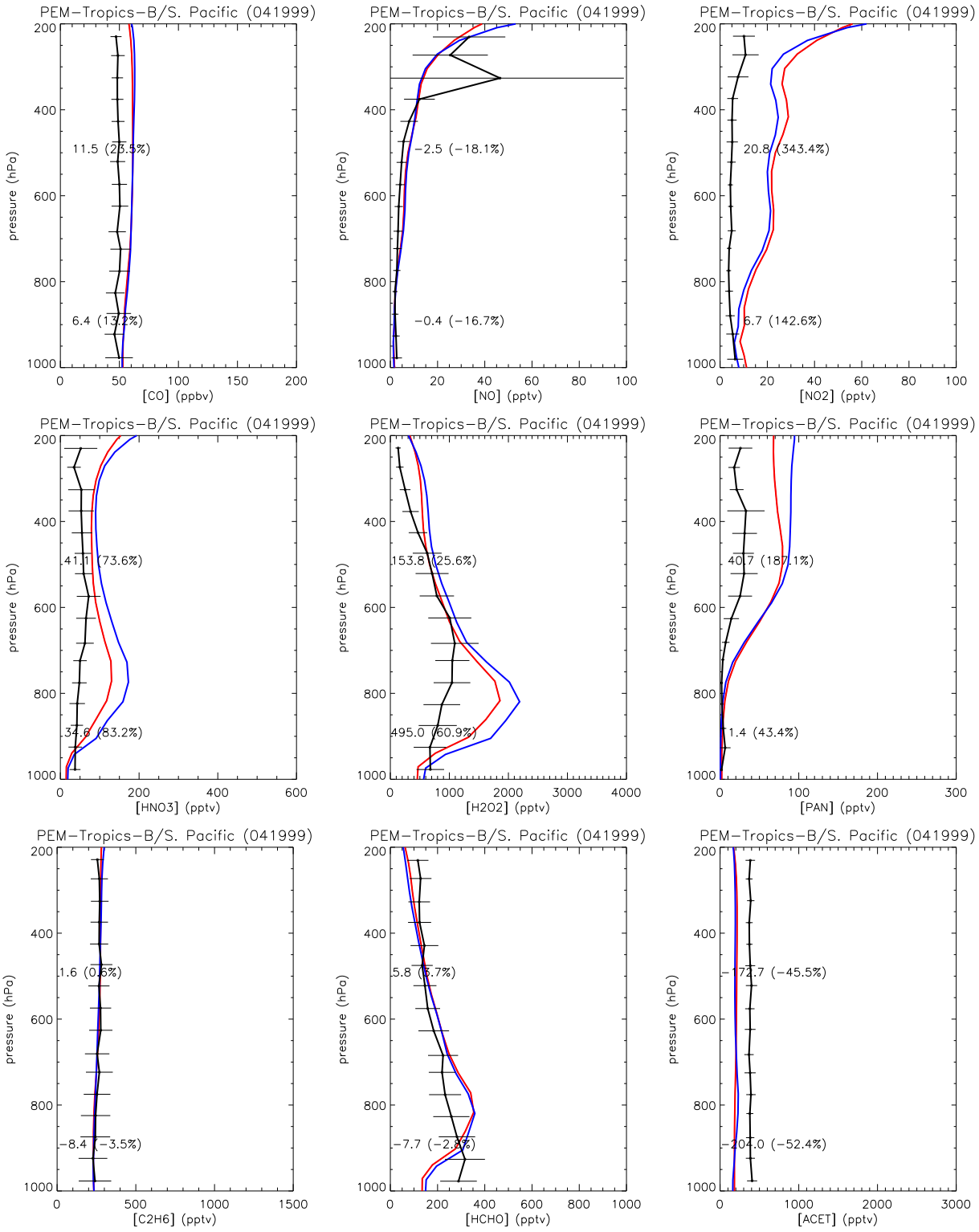

Figure 6: Vertical profiles of the PEM-Tropics-B/S. Pacific region for various species. Aircraft measurements: Black line with error bars, simulated 10-year monthly mean (red), monthly mean of specific year of campaign (blue). The numbers in the indiviual panels give the absolute and relative biases at the respective altitudes compared to the red line.

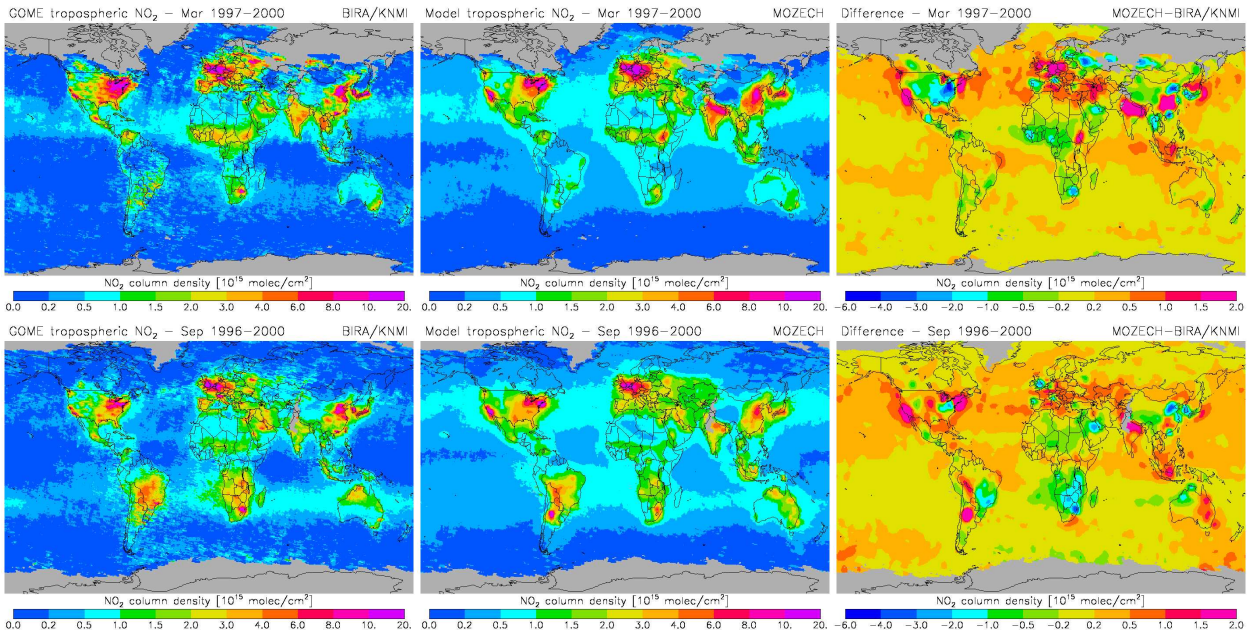

Figure 7: Monthly mean tropospheric NO_2 column density from the BIRA/KNMI retrieval (left) and the ECHAM5-MOZ (abbreviated by MOZECH) long-term simulation (middle) for March (averaged over the years 1997-2000, top) and for September (averaged over the years 1996-2000, bottom). The difference between the simulated and retrieved column density is shown on the right.

4.3 NO_x

Tropospheric column NO_2 retrievals from GOME

The Global Ozone Monitoring Experiment (GOME) instrument was launched on board the second European Remote Sensing (ERS-2) satellite in April 1995. We use the retrieval product developed in a joint effort by BIRA and KNMI (*Boersma et al.*, 2004) to evaluate the tropospheric NO_2 column for 1996-2000 from our model simulation and we include two independent retrievals of data from 2000 for comparison. The simulated tropospheric NO_2 columns were sampled at 10:30h local time and averaged to monthly means. The averaging kernel of the BIRA/KNMI retrieval was applied to the simulation results. Details of the procedure are given by *van Noije et al.* (2006a).

Fig. 7 shows global maps of the retrieved and simulated tropospheric NO_2 column densities for March and September, respectively. We selected these months in order to visualize the impact from biomass burning emissions in the tropics. The spatial patterns are well reproduced by the model in the different seasons, but the model overestimates the NO_2 column densities over India and underestimates them over South Africa in September.

The difference maps calculated after smoothing both data sets to a common horizontal resolution of $5° \times 5°$ (Fig. 7, right column) confirm these findings and reveal that the model also underestimates the NO_2 column near large industrial regions (e.g. near some megacities in China and industrialized regions of the eastern US). On the other hand, ECHAM5-MOZ generally overestimates the retrieval in less industrialized regions with fire emissions.

Annual mean anomalies for the years 1997, 1999 and 2000 are shown in Fig. 25. While the model qualitatively captures most of the relevant anomaly features, it overestimates the observed interannual variability over the biomass burning regions of Northern and Central Africa and the effect of the enhanced fire activity over Indonesia in 1997. The global spatial correlation between the observed and simulated annual mean fields (not shown) is 0.92. This correlation is at the

top of the range calculated by *van Noije et al.* (2006a) for 17 different atmospheric chemistry models.

In Fig. 8, we compare the evolution of the NO_2 abundance in the model and the BIRA/KNMI retrieval from March 1996 to December 2000 over ten continental regions of relatively high pollution. For the year 2000, the corresponding seasonal cycles from the GOME retrieval developed at Bremen University (*Richter et al.*, 2002, 2005) and at Dalhousie University in collaboration with the Smithsonian Astrophysical Observatory (SAO) (*Martin et al.*, 2003) are shown for comparison. The retrievals differ in fitting procedures, chemistry transport model, estimation of the stratospheric background, the radiative transfer code, and other details described by *van Noije et al.* (2006a). The analyzed regions include industrial regions (the eastern United States, Europe, eastern China, India, and South Africa) as well as regions dominated by biomass burning (South America, Northern and Central Africa, Indonesia, and Northern Australia).

Over the eastern United States and over eastern China, the simulated time series are in good agreement with the BIRA/KNMI retrieval except for the year 2000. In the case of the eastern United States, this is partly due to cancellation of errors in the west and east of the analyzed region. The strong enhancement in the BIRA/KNMI and Bremen retrievals over eastern China in January 2000 is based on an unusually small number of observations during this month. Over Europe the model yields larger NO_2 columns than the BIRA/KNMI retrieval during wintertime. However, the Bremen retrieval is higher than the model.

In some regions, the Bremen and Dalhousie/SAO retrievals disagree with the one by BIRA/KNMI. For example, the BIRA/KNMI retrieval shows much higher values over South Africa, where the simulated amount of NO_2 is about a factor of 2 lower. However, when comparing with the Bremen and Dalhousie/SAO retrievals the discrepancy between the simulation and the measurements is much smaller. Over India, on the other hand, the model yields significantly higher NO_2 columns than all three retrievals.

Compared to the simulations analyzed by *van Noije et al.* (2006a), the seasonal cycle of NO_2 column densities obtained by our simulation is much closer to that observed in the BIRA/KNMI retrieval in the case of Latin America and Northern and Southern equatorial Africa. Our simulation overestimates the NO_2 columns over Central Africa in 1998 and 1999 during the dry season. The timing of particular fire events, such as the Indonesian fires during the El Niño of 1997/1998, is well reproduced by the model, although the NO_2 column is strongly overestimated during the period of pollution.

We conclude that the spatio-temporal variation of the NO_2 column is generally well represented by the model compared to satellite retrieval products. Nevertheless, the sensitivity of the NO_2 columns to emissions causes deviations on a regional scale. Furthermore, the uncertainties in the various retrieval products have to be taken into account in such comparisons.

4.4 Vertical ozone profiles

Vertically resolved ozone concentrations are available from the World Ozone and Ultraviolet Radiation Data Centre (WOUDC, `http://www.woudc.org`[2]) which archives measurements since 1960 and the Southern Hemisphere Additional Ozone Stations (SHADOZ) since 1998 (*Thompson et al.*, 2003a,b). We chose eleven stations with reasonable sampling statistics and covering a wide range of latitudes (Tab. 5). Nevertheless, the higher latitudes in the Southern hemisphere are underrepresented.

The ozone sonde measurements were first interpolated to a vertical pressure grid with a spacing of 10 hPa using the Akima spline interpolation. This spline avoids oscillations in the interpolation polynomial (*Akima*, 1970). We calculate the median and the 25 and 75 percentiles for each month where data are available. Model results were sampled at the time of observation (last 3-hourly value before launch) and interpolated onto the same vertical grid.

[2]last accessed 2014-05-08

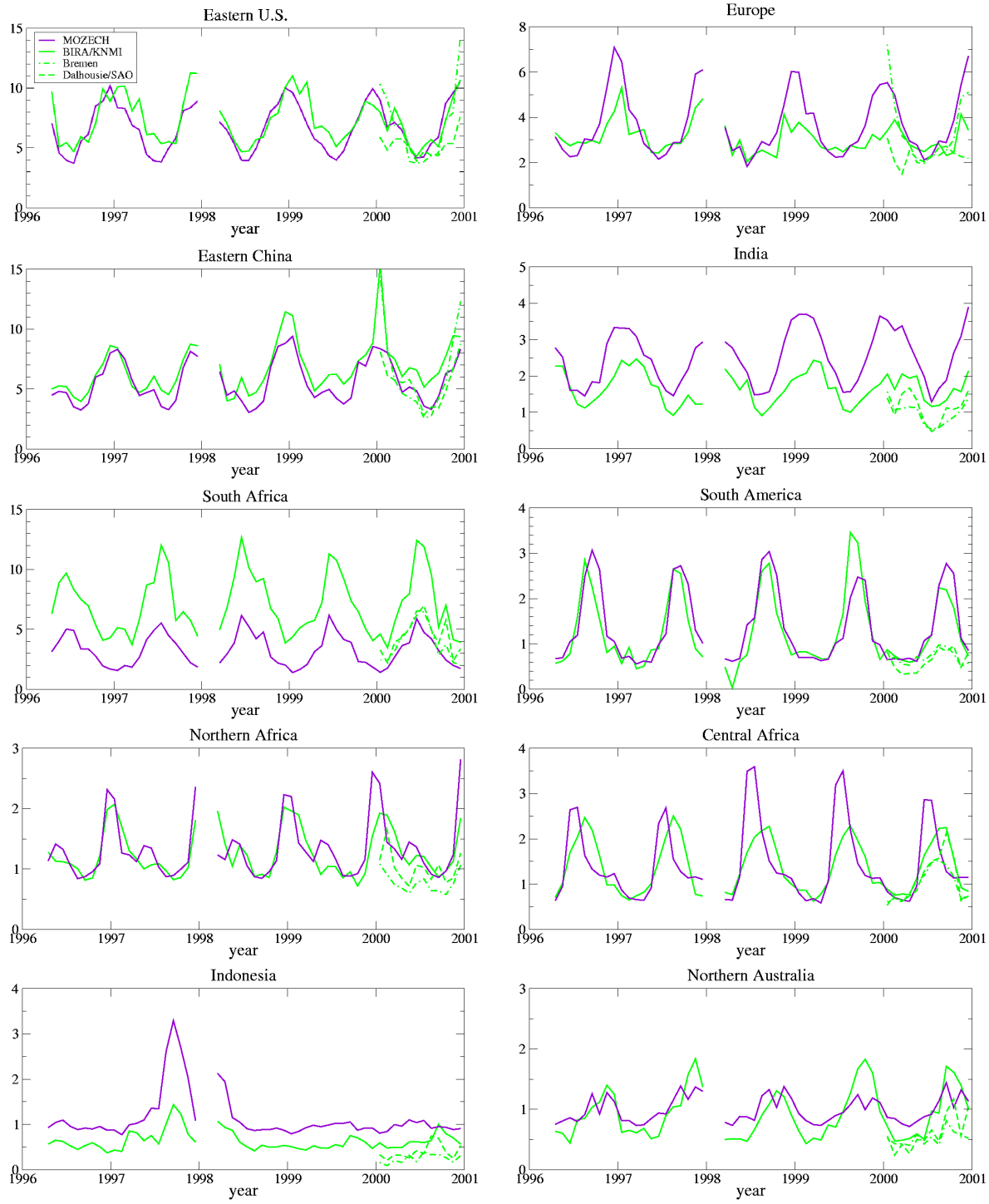

Figure 8: Time series of the tropospheric NO_2 column density over different regions of the world from April 1996 to December 2000. The data points are the monthly means from the BIRA/KNMI retrieval (green line) and the ECHAM5-MOZ (abbreviated by MOZECH) long-term simulation (blue line). For the year 2000 the alternative retrievals from Bremen and Dalhousie are included as dashed and dash-dotted lines, respectively. The definition of the regions can be found in Tab. 14.

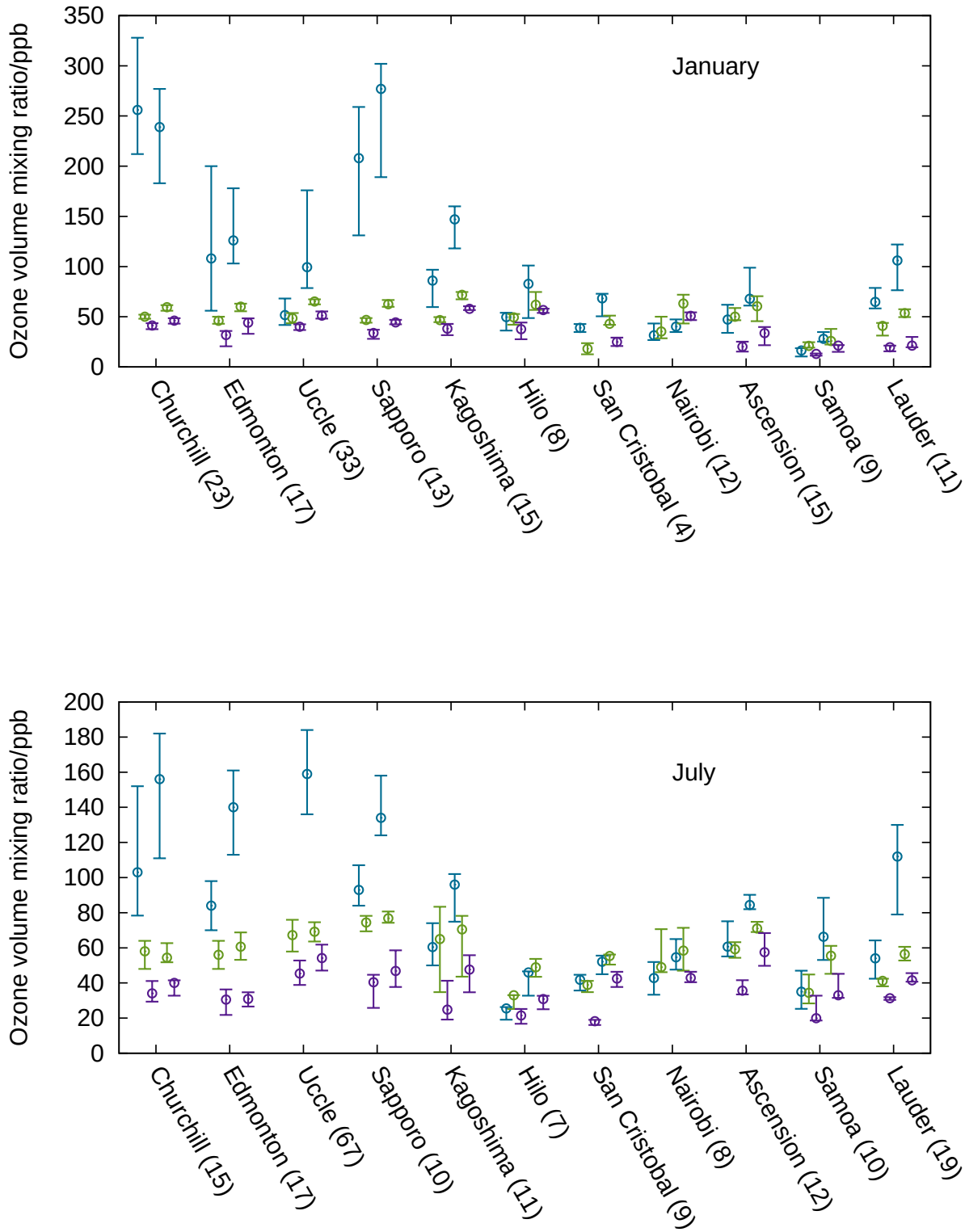

Figure 9: Median, 25 and 75 percentiles of ozone volume mixing ratio for ozone sonde measurements (left of station names) and simulation (right of station names) at 250 (light blue), 500 (green), and 850 hPa (dark blue) for January (top) and July (bottom). At some stations, certain altitudes may be missing, e.g. the measurements at 850 hPa at Nairobi. The model orography is a bit lower and values are available there. The samplesize is given in parenthesis behind station names. The geographical location of the ozone sonde stations and measurement periods are listed in Tab 5.

Table 5: Geographical location of the ozone sonde stations and measurement period used in the ECHAM5-MOZ evaluation. (WOUDC).

Station name	country	measurement period (missing period)	longitude	latitude
Churchill	Canada	1997/01-2000/09 (1999/12)	94.07° W	58.74°
Edmonton	Canada	1997/01-2000/12	114.1° W	53.55° N
Uccle	Belgium	1997/04-2000/12	4.35° E	50.8° N
Sapporo	Japan	1997/01-1999/12	141.3° E	43.1° N
Kagoshima	Japan	1997/01-2000/12	130.6° E	31.6° N
Hilo	Hawaii	1999/01-2000/12	155.04° W	19.43° N
San Cristóbal	Galapagos	1998/03-2000/12 (1998/05-1998/08)	89.60° W	0.92° S
Nairobi	Kenya	1998/01-2000/12 (1998/07-1998/08) (2000/03-2000/04)	36.8° E	1.27° S
Ascension		1998/01-2000/12 (1998/04,1999/12) (2000/09-2000/10)	14.42° W	7.98° S
Pago Pago	American Samoa	1998/01-2000/12 (1998/08)	170.56° W	14.23° S
Lauder	New Zealand	1997/01-2000/09	169.68° E	45.044° S

In Fig. 9, we present the median, 25, and 75 percentiles of the measured and simulated ozone volume mixing ratio at 250, 500, and 850 hPa for the months of January and July.

The ozone volume mixing ratio does not obey a symmetric distribution, neither in the observations nor in the simulations. Large asymmetries occur at the pressure level of 250 hPa (e.g. measurements performed at Churchill or Edmonton in January or simulated values for Edmonton, Uccle, or Ascension in January) and to a lesser extent at 850 hPa (e.g. measurements performed at Sapporo or Samoa in July or simulated values for Edmonton or Samoa in July). We interprete the asymmetries as a consequence of ozone intrusion events at the 250 hPa altitude level and occasional advection of particularly ozone rich or poor air at the 850 hPa altitude level. The difference between the 75 percentile and the 25 percentile agrees well between observations and simulation at 500 hPa and 850 hPa.

The relative bias is smallest at 500 hPa except at Hilo and San Cristóbal in July. There is a high bias in the simulated ozone volume mixing ratios at 250 hPa for all stations indicating that too much ozone is transported from the stratosphere into the upper troposphere. The high bias of the model found at the 850 hPa aggravates towards the surface (not shown here) and may reach 0.6 in extreme cases in the lowest model level. This indicates problems to simulate the complex interaction between transport and chemistry in the planetary boundary layer over complex terrain.

In Fig. 10 we show a zonal slice of the simulated ozone volume mixing ratio mean over March, April, May (1998-2000) and September, October, November (1998-2000). The ozone wave one pattern (*Thompson et al.*, 2003b) is well reproduced in position and amplitude by the simulation, but there is some overall high bias in the ozone concentrations. The most important difference between model and observations is the altitude of the local maximum near 100°E. In the observations, this is near the surface, while the model places it at about 600 hPa. The simulation shows a local volume mixing ratio maximum near the surface between 60 and 70°W that is not present in the observations. This is presumably caused by excessive pollution outflow from the South American continent. Due to the low model resolution the Andes do not represent

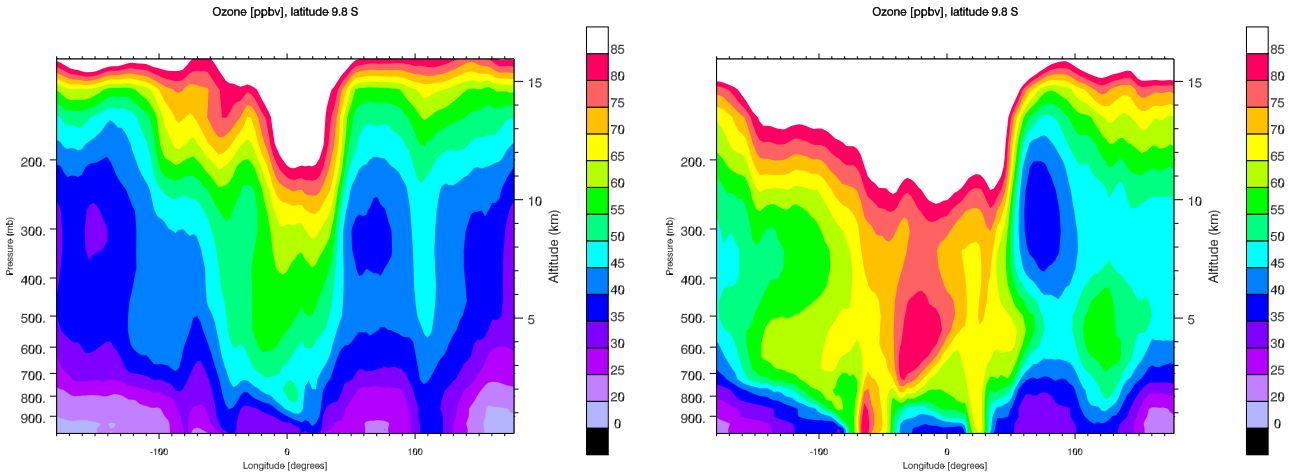

Figure 10: Zonal slice at 9.7°S of the March, April, May (left) and September, October, November (right) mean value for the years 1998-2000 of the ozone volume mixing ratio. Longitude is in degrees East.

Table 6: Geographical location and modified normalized mean bias (MNMB, eq. 1) at 250, 500, and 850 hPa for selected MOZAIC measurement airports.

Airport	geogr. location	MNMB
Brussels	50.90 N 4.48 E	0.28/0.13/0.11
Beijing	40.08 N 116.6 E	0.21/0.16/0.11
Teheran	35.69 N 51.31 E	0.30/0.12/0.09
Atlanta	33.64 N 84.43 W	0.36/0.20/0.15
Shanghai	31.14 N 121.8 E	0.26/0.16/0.15
Bangkok	31.68 N 100.75 E	– /0.20/0.27
Windhoek	22.49 S 17.46 E	0.25/0.17/0.22
São Paolo	23.43 S 46.47 W	0.29/0.21/0.22
Johannesburg	26.14 S 28.24 E	0.30/0.17/0.18

a strong enough transport barrier.

In Fig. 11, we present the simulated and measured seasonal cycle of ozone volume mixing ratios at 500 hPa for the ozone sonde stations listed in Tab. 5. The phase of the simulated seasonal cycle is in good agreement with the ozone sonde measurements at all stations.

4.5 MOZAIC aircraft observations

Measurements of ozone and water vapour by Airbus in-service aircraft (MOZAIC) began in 1994. They offer the possibility to get a climatology of upper tropospheric/lower stratospheric ozone concentrations and relatively frequent profiles at certain locations over a long time period (*Marenco et al.*, 1998). The measurement devices which have been deployed on up to five commercial aircrafts are cross checked regularly and have a common calibration standard. Thus, we have a homogeneous data set for the various geographical locations. We use monthly mean concentrations for nine selected airports at different altitudes (see Tab. 6 and Fig. 12).

The model shows the same high bias as in the evaluation with O_3 sonde measurements, but an often even stronger bias in the upper troposphere at about 250 hPa. The simulated amplitude of the seasonal cycle in the northern hemisphere is too low while it is larger than in the measurements in the southern hemisphere except at Johannesburg.

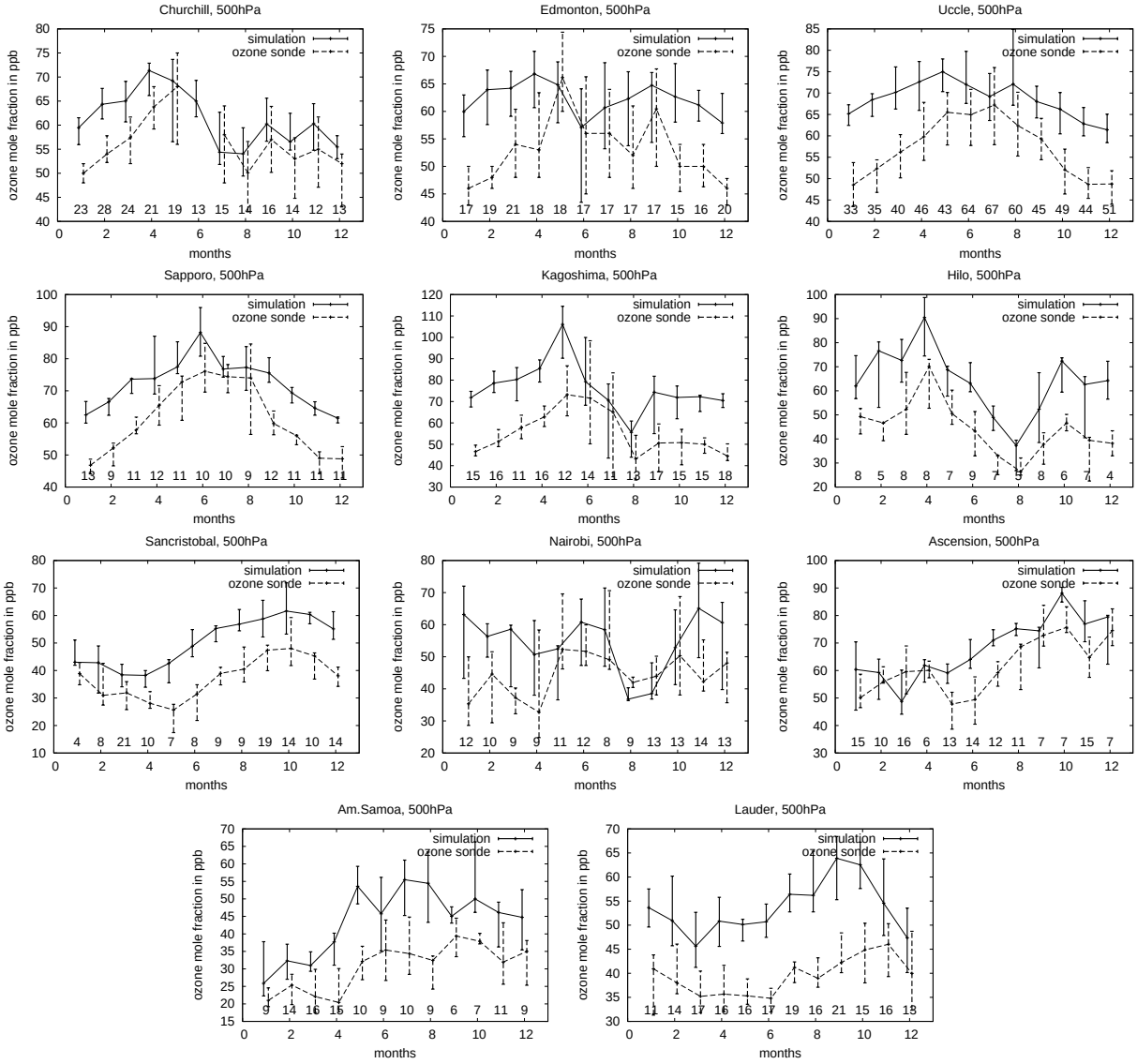

Figure 11: Median, 25 and 75 percentiles of simulated (full lines) and measured (dashed lines) seasonal cycle of ozone volume mixing ratios at 500 hPa. The numbers at the bottom give the sample size. The measurement periods and location of the ozone sonde station are listed in Table 5. Note the different scales.

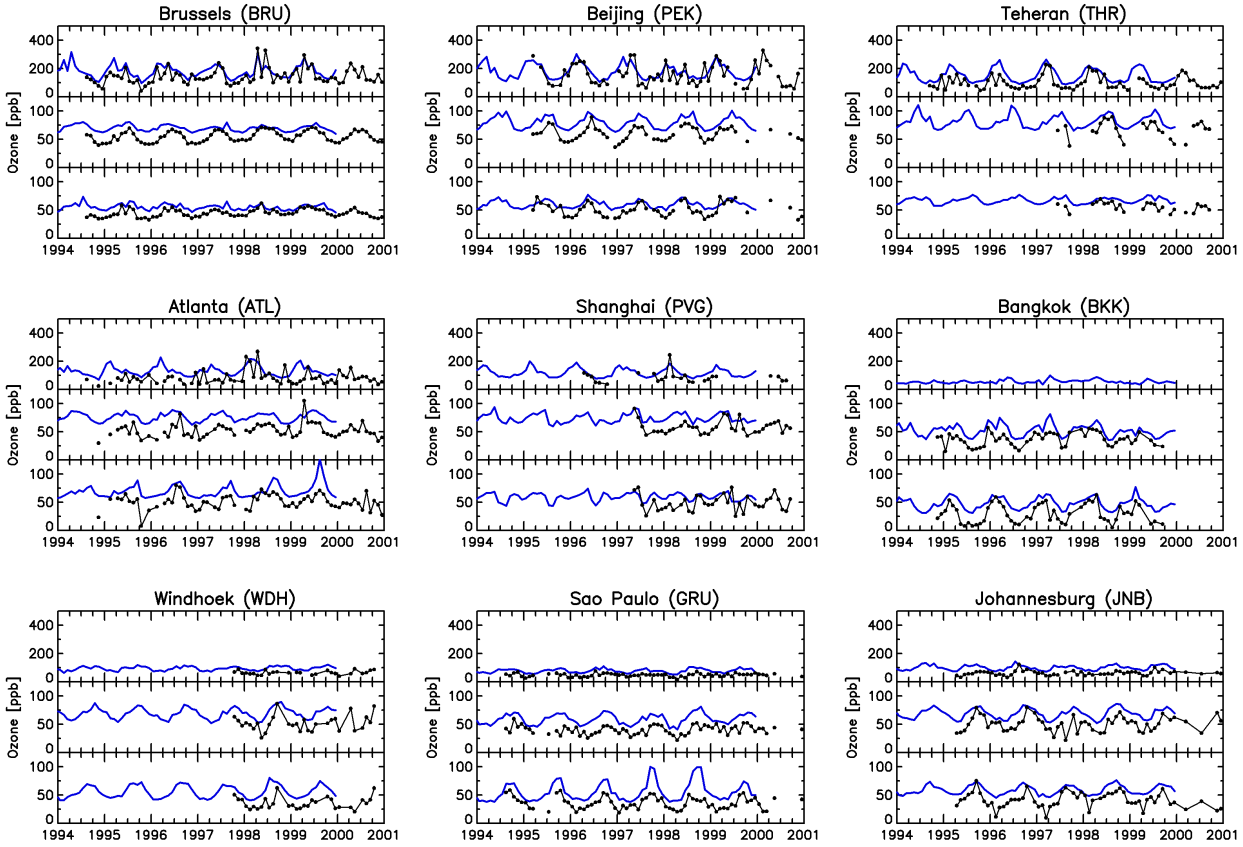

Figure 12: MOZAIC (black) and ECHAM5-MOZ (blue) monthly ozone mole fractions at various height levels for the nine airports Brussels, Beijing, Teheran, Atlanta, Shanghai, Bangkok, Windhoek, São Paolo, Johannesburg from top left to bottom right. The nominal pressures (pressure reduced to a sea level pressure of 1013 hPa) are 250, 500, 850 hPa.

4.6 Surface ozone concentrations

In the following, we compare our simulation results with annual and seasonal mean values for a number of surface sites with reasonably long measurement series (Table 7). This list of stations is biased towards the US and Europe, where most of the long time series exist. Recently, more data have become available from other regions (cf. World Data Center for Greenhouse Gases), but these measurements usually begin after the year 2000 and are therefore not used in this study. We group the data sets into four main categories: (1) Global low-altitude background sites, (2) Global mountain sites, (3) EMEP rural sites and (4) CASTNET rural sites. EMEP is the Co-operative Programme for Monitoring and Evaluation of the Long-range Transmission of Air pollutants in Europe (data repository at `http://www.nilu.no/projects/CCC/emepdata.html`[3]) and CASTNET is the Clean Air Status and Trends Network of the US (data repository at `http://epa.gov/castnet/javaweb/index.html`[4]). Other data are taken from the World Data Center for Greenhouse Gases (WDCGG) in Japan (`http://ds.data.jma.go.jp/gmd/wdcgg/`[5]) and the US National Park Service (`http://www.nature.nps.gov/air/Monitoring/network.cfm`[6]). We evaluate the model bias in surface ozone concentrations and include some description of the typical seasonal and diurnal cycles. The interannual variability and possible trend at these sites are analysed in section 5.3.

Comparing coarse-resolution simulations from global models with surface ozone observations is not straightforward, because often the surface sites are influenced by local orographic meteorology or the advection of regional pollution which are not resolved in the model. Another problem, in particular for older data, is the quality of the data reported for some stations. Scanning through a multitude of data sets from different networks and data centers, we found several occasions of obviously wrong data and also many instances where the observations appear at least questionable. We therefore applied a statistical filter to remove outliers and other data points with a high probability of being in error (e.g. near a series of missing values) before calculating monthly, seasonal and annual mean values for the model evaluation. Where we include wind sector filtering in the analysis, all wind data are taken from the model simulation. Several stations do not provide observed wind direction and speed and the model wind is supposedly more representative of the larger scale circulation.

4.6.1 Global low-altitude background sites

Table 8 summarizes the decadal mean concentrations and the model bias for the 14 low altitude surface sites listed in Table 7. Eight out of the fourteen stations show acceptable agreement (bias below 6 ppbv) with the observations. These are either high latitude sites or stations with frequent advection of marine air from westerly directions (Westerland, Mace Head and Cape Grim). At all of these sites, the model reproduces the diurnal cycle in all seasons and the seasonal cycle rather well, and it generally also captures the variability of the data with respect to wind direction. As an example we show the detailed analysis for Mace Head in Figure 13. Similar plots for all sites analyzed in this study can be found at ftp://ftp.retro.enes.org/pub/documents/trend_eval. As an interesting side-aspect we note that the wind sector analysis for Spitsbergen and Barrow reveals a clear signal of halogen-induced ozone depletion in spring (NW winds). This is absent from the model results due to the lack of halogen chemistry.

The reasons for the larger discrepancy between model results and observations at other stations are manifold. For example, in Zingst the shape of the diurnal cycle agrees well, but the model shows a larger diurnal cycle amplitude in spring and summer. The observations

[3]last accessed 2014-05-08
[4]last accessed 2014-05-08
[5]last accessed 2014-05-08
[6]last accessed 2014-05-08

Table 7: List of stations with surface ozone measurements used in the model evaluation of this study. For additional EMEP and CASTNET rural sites which were used only as mean values we provide the station information in section C.3. All data sets were screened for obvious outliers and observations were paired with the corresponding 3-hourly model results. Vertical model levels were chosen according to the average pressure at the station altitude. Station altitudes are given in m. The references refer to previous studies which have used these data in trend or variability analyses: C2005: Carslaw, 2005; D2007: Derwent et al., 2007; J2007: Jaffe and Ray, 2007; K2008: Koumoutsaris et al., 2008; O2006: Oltmans et al., 2006; P2009: Parrish et al., 2009; S2004: Simmonds et al., 2004. Note that we included South Pole in the list of low-altitude sites in spite of its actual altitude of 2810 m.

Code	Site name	Data source	Latitude	Longitude	Altitude	Years	Ref.
Global background sites, altitude < 700 m							
no42	Spitsbergen, Norway	EMEP	78.90 N	11.88 E	474	1990–2000	
brw	Barrow, Alaska	NOAA	71.32 N	156.60 W	11	1973–2000	J2007, K2008, O2006
dena	Denali National Park	US NPS	63.73 N	148.96 W	661	1987–2000	J2007, O2006
ice	Vestmannaeyjar, Iceland	NOAA	63.25 N	20.15 W	100	1992–1997	
de01	Westerland, Germany	EMEP	54.93 N	8.31 E	12	1990–2000	
de09	Zingst, Germany	EMEP	54.43 N	12.73 E	1	1991–2000	
ie31	Mace Head, Ireland	EMEP	53.17 N	9.50 W	15	1990–2000	C2005, D2007, K2008, O2006, P2009, S2004
ryo	Ryori, Japan	GAW	39.03 N	141.82 E	260	1990–2000	
tkb	Tsukuba, Japan	GAW	36.04 N	140.13 E	25	1988–2000	
bmw	Tudor Hill, Bermuda	NOAA	32.27 N	64.88 W	30	1988–1998	O2006
smo	Tutuila, Samoa	NOAA	14.25 S	170.57 W	42	1975–2000	O2006
bar	Baring Head, Australia	GAW	41.42 S	174.87 E	85	1991–2000	O2006
cgo	Cape Grim, Australia	GAW	40.68 S	144.68 E	94	1982–1989	O2006
spo	South Pole	NOAA	89.98 S	24.80 W	2810	1975–2000	O2006
Global mountain sites, altitude ≥ 700 m							
glr468	Glacier NP	CASTNET	48.51 N	114.00 W	976	1989–2000	J2007, O2006
hpb	Hohenpeissenberg, Germany	GAW	47.80 N	11.20 E	985	1980–2000	
jfj	Jungfraujoch, Switzerland	GAW	46.55 N	7.99 E	3580	1986–2000	K2008
zug	Zugspitze, Germany	GAW	47.42 N	10.98 E	2960	1995–2000	O2006
yell	Yellowstone National Park, US	US NPS	44.56 N	110.39 W	2361	1987–2000	J2007
crmo	Craters of the Moon, US	US NPS	43.46 N	113.56 W	1815	1992–2000	J2007
pnd165	Pinedale, US	CASTNET	42.93 N	109.79 W	2388	1989–2000	J2007
cnt169	Centennial, US	CASTNET	41.36 N	106.24 W	3178	1989–2000	J2007
lavo	Lassen Volcanic National Park, US	US NPS	40.54 N	121.58 W	1756	1987–2000	J2007, O2006
romo	Rocky Mountain National Park, US	US NPS	40.28 N	105.55 W	2743	1987–2000	J2007
nwr	Niwot Ridge, US	NOAA	40.05 N	105.58 W	3475	1990–1998	
gth161	Gothic, US	CASTNET	38.96 N	106.99 W	2926	1989–2000	J2007
shn418	Shenandoah, Big Meadows, US	CASTNET	38.52 N	78.43 W	1073	1988–2000	
cany	Canyonlands National Park, US	US NPS	38.46 N	109.82 W	1809	1992–2000	J2007
vpi120	Horton Station, US	CASTNET	37.33 N	80.56 W	920	1987–2000	
pnf126	Cranberry, US	CASTNET	36.11 N	82.05 W	1219	1989–2000	
grc474	Grand Canyon, US	CASTNET	36.06 N	112.18 W	2073	1989–2000	
cha467	Chiricahua, US	CASTNET	32.01 N	109.39 W	1570	1989–2000	
mlo	Mauna Loa, Hawaii	NOAA	19.53 N	155.58 W	3397	1973–2000	K2008, O2006

Table 8: Annual mean concentrations of surface ozone and bias at low altitude background sites (see Tab. 7 for a description of the sites). MNMB is the modified normalized mean bias (eq. 1). IE31(2) denotes the Mace Head data set with a wind filter applied so that only data associated with winds between SW and NNW are used.

station	mean obs./ppbv	mean model/ppbv	bias/ppbv	MNMB
no42	32.88	36.37	3.49	0.0525
brw	26.27	26.61	0.34	0.0119
dena	30.72	32.91	2.19	0.0352
ice	36.88	41.40	4.52	0.0590
de01	30.95	32.88	1.92	0.0393
de09	28.70	40.21	11.51	0.1633
ie31	35.21	38.81	3.60	0.0492
ie31(2)	37.27	39.50	2.22	0.0284
ryo	38.06	51.06	12.99	0.1471
tkb	23.04	44.55	21.51	0.3403
bmw	37.19	52.23	15.04	0.1780
smo	12.56	24.06	11.51	0.3586
bar	20.06	30.74	10.67	0.2109
cgo	23.77	29.51	5.75	0.1058
spo	28.16	28.66	0.50	0.0060

exhibit maximum concentrations in spring when the wind blows from the East, while the model doesn't show any enhancement there. A possible explanation for this discrepancy is a potential underestimation of agricultural waste burning emissions in Eastern Europe. The Ryori results agree reasonably well with the observations in winter (bias 6 ppbv), but the model exhibits a too strong rise in ozone concentrations towards spring. It completely misses the very low values in summer which are related to the monsoon circulation. In Bermuda, the simulated diurnal and seasonal cycles are in qualitative agreement with the measurements (although the seasonal cycle amplitude is lower in the model with 22 ppbv versus 28 ppbv in the observations), and also the wind sector comparison shows no obvious discrepancy. Nevertheless, a large offset of 15 ppbv occurs, for which we don't have a good explanation at present. In Samoa, the situation is similar except that here, the seasonal cycle amplitude of the model is larger (19 ppbv versus 11 ppbv). Also, the Samoa observations exhibit maximum concentrations in SE winds in summer and fall, while the model shows this enhancement also in spring.

4.6.2 Global mountain sites

The model bias at the higher-altitude sites is generally larger than for the low-altitude stations. Except for Zugspitze, where we looked at a relatively short record, the model bias is always greater than 10 ppbv and often more than 20 ppbv (Table 9). *Scheel et al.* (1997) suggest to use only nighttime data in the model evaluation, because of the possible impact of local upslope flows during daytime. In our analysis, we often find that the model bias is actually worse under nighttime conditions. A notable exception is the station Canyonlands, where the bias is reduced from 11 to 6 ppbv. Reducing both data sets to west wind situations generally doesn't improve the bias either. The greatest improvement is seen for Lassen Volcanic Park, where the bias is reduced from 17.4 to 14.5 ppbv. The substantial positive bias seen in this analysis confirms the results obtained from the evaluation with ozone sonde and MOZAIC aircraft data in sections 4.4 and 4.5.

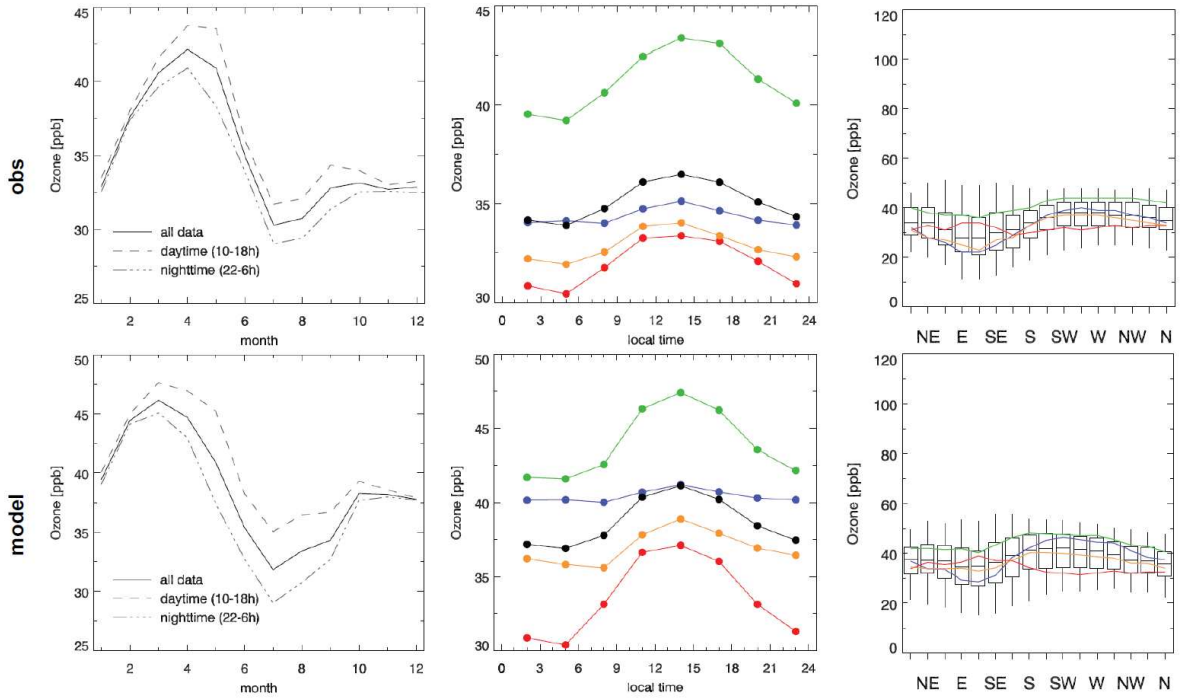

Figure 13: Seasonal cycle, diurnal cycle and wind sector analysis of observed and simulated surface ozone concentrations at Mace Head, Ireland. Black: annual mean, blue: winter (DJF), green: spring (MAM), red: summer (JJA) and orange: fall (SON). In the wind sector plot, the annual data are presented as boxes and whiskers showing the median, central 50% and central 90% of the data.

Table 9: Annual mean concentrations of surface ozone and bias at global mountain sites (see Tab. 7 for a description of the sites). MNMB is the modified normalized mean bias (eq. 1). Bias-night denotes the bias for nighttime data (22–6 h), and bias W denotes the bias for west wind situations (236–303 deg).

station	mean obs./ ppbv	mean model/ ppbv	bias/ ppbv	MNMB	bias-night/ ppbv	bias-W/ ppbv
glr468	25.15	39.13	13.97	0.2230	16.84	14.58
hpb	37.80	54.67	16.87	0.1847	16.57	17.89
jfj	50.92	64.22	13.31	0.1200	13.14	13.67
zug	51.29	61.84	10.54	0.0960	9.96	10.75
yell	38.03	59.21	21.18	0.2209	24.37	20.36
crmo	39.81	54.39	14.58	0.1558	n.a.	13.87
pnd165	46.83	59.16	12.32	0.1180	13.73	12.44
cnt169	49.54	65.81	16.26	0.1420	17.30	16.29
lavo	37.68	55.04	17.36	0.1879	19.63	14.52
romo	42.92	63.71	20.79	0.1967	23.65	19.71
nwr	47.02	66.75	19.73	0.1742	22.13	18.99
gth161	45.67	67.61	21.95	0.1945	26.31	22.50
shn418	46.26	66.72	20.46	0.1883	19.59	19.98
cany	46.21	57.29	11.08	0.1093	5.78	13.63
vpi120	44.84	64.81	19.96	0.1881	19.09	20.39
pnf126	45.30	68.47	23.17	0.2047	24.33	24.08
grc474	47.80	73.45	25.66	0.2104	26.35	27.12
cha467	41.95	70.10	28.15	0.2537	32.46	28.96
mlo	38.05	56.15	18.10	0.1890	15.88	17.02

Table 10: Average annual mean concentrations of surface ozone and biases at rural EMEP and CASTNET sites. Only daytime data were used (10–18 h).

Region	N_{stations}	mean obs.	mean model	bias	MNMB
Central Europe	21	32.83	43.96	11.13	0.1485
Northern Europe	21	32.47	40.52	8.05	0.1153
Western Europe	14	30.30	41.89	11.59	0.1551
Eastern Europe	3	39.11	50.79	11.68	0.1304
Mediterranean	5	37.81	57.85	20.04	0.2250
Mountain sites	13	41.18	57.31	16.13	0.1751
CASTNET	26	42.38	60.93	18.55	0.1730

4.7 EMEP and CASTNET stations

For the comparison with rural stations from the EMEP network, we defined 6 station categories for which we present average values in this paragraph. A detailed analysis of seasonal and diurnal cycles and wind sector patterns is again available on ftp://ftp.retro.enes.org/pub/documents/trend_eval. The EMEP sites were grouped according to geographic location into the classes (1) Central European, (2) Northern European, (3) Western European, (4) Eastern European, (5) Mediterranean, and (6) Mountain sites. CASTNET stations were all treated as one category. Mountain sites are again defined by a station altitude $\geq$ 700 m. Stations already included in the list of global sites were not included in this analysis. Section C.3 contains a complete list of the EMEP stations used in this analysis and their classification.

For most of Europe, the model bias is between 8 and 12 ppbv, about twice as high as the bias obtained for the majority of global low-altitude background stations. The Mediterranean stations exhibit a much larger bias on average consistent with D2006, but Ispra (IT04) and Noya (ES05) behave similar to the rest of Europe. The bias for the EMEP mountain sites is similar to the bias obtained for global mountain stations. The lowest bias is obtained for Oulanka, Finland (bias 2.9 ppbv) and the largest bias is found for Monte Velho, Portugal (bias 28.8 ppbv).

The simulated surface ozone values for the rural CASTNET sites show a larger bias than the values at most of the EMEP sites. Best agreement is obtained for Ashland (bias 6.9 ppbv) and Perkinstown (bias 7.7 ppbv), worst results are for Sumatra (bias 29.3 ppbv) and Beltsville (bias 43.6 ppbv). In the model Beltsville shares the same grid box as Washington, DC and therefore the simulation results for this site cannot be considered to bear a rural signature. Similar problems might be responsible for the poor agreement of the model simulations in Sumatra, Florida. In the coarse resolution model this site may well experience mixed influences from the large refineries of the Houston area, large contributions from biogenic VOC emissions and from other urban sources.

4.8 Analysis of other species from aircraft field campaigns

Regionally averaged vertical profiles from aircraft measurements provide an opportunity to evaluate other species such as PAN, HNO_3, H_2O_2, and hydrocarbons (cf. *Emmons et al.*, 2000). The vertical profiles of two example regions (PEM-West-A and PEM-Tropics-B) are shown in Fig. 5 and Fig. 6. In the polluted PEM-West-A region (Fig. 5), the nitrogen containing species NO, NO_2, HNO_3 and PAN are overestimated by the simulation in particular in the planetary boundary layer. The agreement is better for all species in the remote region PEM-Tropics-B of the Southern Pacific (Fig. 6). The bias is almost independent of the way the model results were sampled except for HNO_3 and PAN in the PEM-West-A. Because these species are secondary species that are primarily formed in the atmosphere and there is only a small difference between

the 10-year monthly mean and the specific monthly mean for their precursors, these differences are more likely caused by the interannual variability in meteorological conditions than by the variation in emissions. Observations and model results for other regions are shown in section C.2.

4.9 OH

We compare the 10-year average (1991–2000) OH concentration from our simulation to the data of *Spivakovsky et al.* (2000), which have been widely used in the literature (Fig. 14). The important features of the global OH distribution are rather similar between the two datasets and the magnitude of the zonal mean OH concentration agrees typically within 20%. In our simulation, the tropical OH maximum is located closer to the surface (900 hPa versus 700 hPa) and the maximum is larger by 15%. The zonal mean values in ECHAM5-MOZ exhibit a second local maximum at about 150 hPa in the outflow regions of tropical convection. This is a zone where polluted air originating from the boundary layer is exposed to intense radiation and photolysis is rather fast. *Jaeglé et al.* (2001) have found that the photolytic destruction of acetone can provide a major source for OH at these altitudes. We find no evidence for a significant overestimation of acetone in the upper troposphere (section C.2).

4.10 Lifetime of methane and methyl chloroform

For i being either methylchloroform or methane, the total atmospheric lifetime is given by

$$\tau_i = B_i/(F_{i+\mathrm{OH}} + F_{i\mathrm{dep}} + F_{i\mathrm{strat}}) \tag{2}$$

where B_i is the model burden of i in the whole atmosphere, $F_{i+\mathrm{OH}}$ is the loss due to reaction of i with tropospheric OH, and $F_{i\mathrm{dep}}$ and $F_{i\mathrm{strat}}$ are losses due to deposition and chemical reaction in the stratosphere, respectively. In the case of methylchloroform, we give the lifetime versus OH, only, as *Prinn et al.* (2001). In the case of methane, we assume a deposition flux at the surface of $F_{\mathrm{soil}} = 30\,\mathrm{Tg/yr}$ and a sink in the stratosphere of $F_{\mathrm{strat}} = 40\,\mathrm{Tg/yr}$ (see *Stevenson et al.*, 2006; *IPCC*, 2001).

We calculated the lifetimes using either the WMO criterion for the definition of the tropopause ("thermal tropopause") or a 150 ppbv ozone threshold criterion ("chemical tropopause"). The resulting differences in τ_i are negligible.

The mean value of the CH_3CCl_3 lifetime between 1980 and 2000 is $5.27 \pm 0.04\,\mathrm{yr}$ with respect to OH, and the CH_4 lifetime is $(7.55 \pm 0.06)\,\mathrm{yr}$. The standard deviation is calculated on the basis of yearly means of the lifetime. The interannual variability is small and no trend was found. Compared to the mean of 25 models for which *Stevenson et al.* (2006) applied the same formula (2), the lifetime is shorter by about 13% but still within the one-σ interval of the results reported there. Compared to the values given by *Prinn et al.* (2001, Table 1), the CH_3CCl_3 lifetime is shorter by 12% and the methane lifetime is shorter by 19%. The relatively high OH concentrations and the shift of the maximum to lower altitudes compared to the climatology of *Spivakovsky et al.* (2000) contribute about equally to the short lifetime. *Spivakovsky et al.* (2000) reports a CH_3CCl_3 lifetime versus OH of 5.7 years that is 8% longer than ours.

4.10.1 Global ozone budget

We diagnosed the chemical production (p), loss (l) and the surface deposition (d) of ozone in the model at each grid box. For the p and l terms, all reactions which lead to the formation or destruction of any member of the $\mathrm{OX} = \mathrm{O_3} + \mathrm{O(^1D)} + \mathrm{NO_2} + \mathrm{NO_3} + 2\mathrm{N_2O_5}$ family (*Horowitz et al.*, 2003) were taken into account. For the ozone production these are all reactions of NO with peroxy radicals. The ozone loss is determined by the reaction of $\mathrm{O(^1D)}$ with water, the reaction of ozone with OH, HO_2 and hydrocarbons, and the reaction of NO_2 with OH, and the hydrolysis of N_2O_5 and NO_3 on sulfate aerosol surfaces. The tropospheric

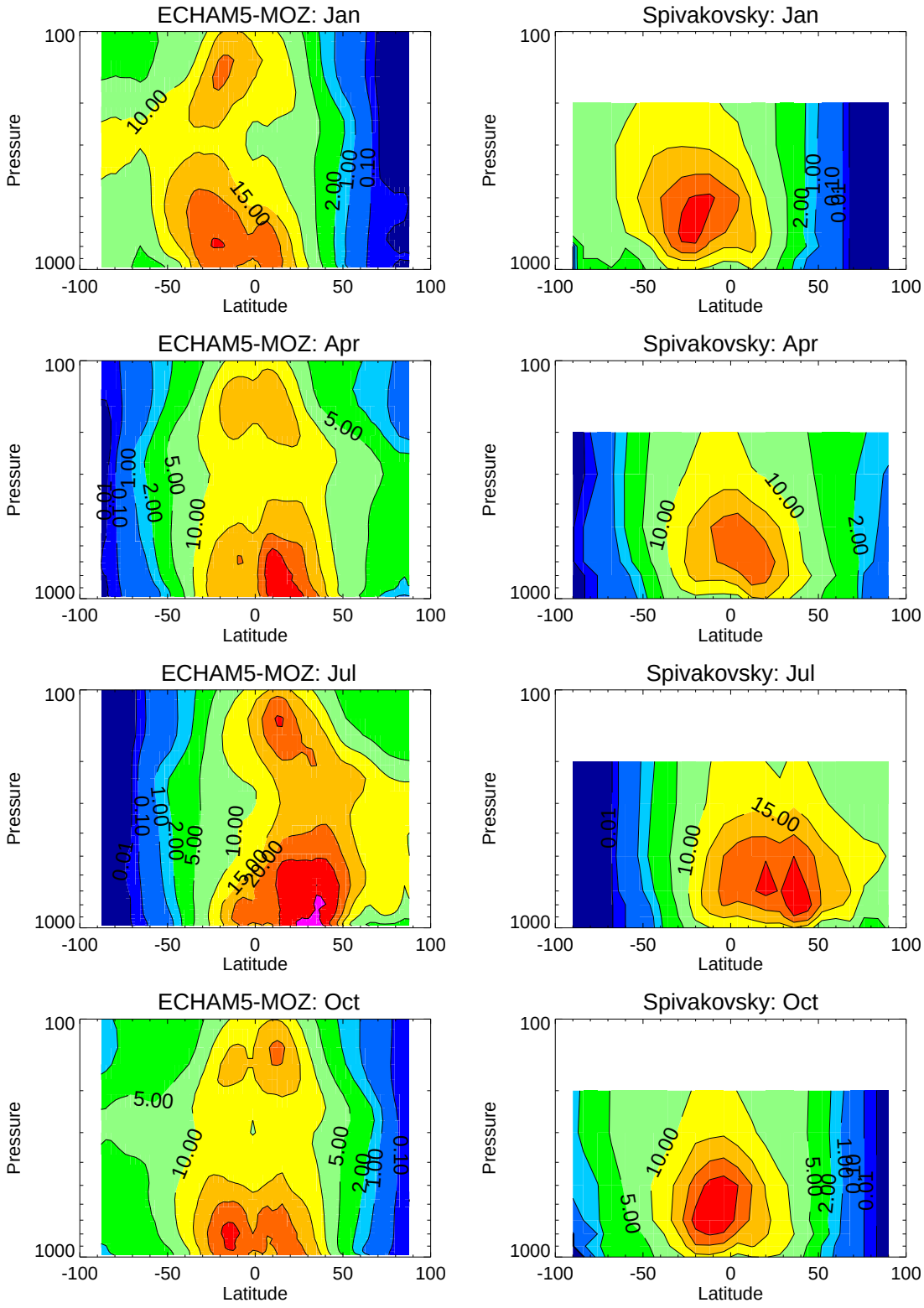

Figure 14: Ten-year (1991-2000) average zonal mean OH concentration from ECHAM5-MOZ in comparison to the results of *Spivakovsky et al.* (2000) in 10^5 molecules/cm^3. Monthly averages are shown for January, April, July and October (top to bottom).

burden B, production P, and loss L, and deposition D are the integrated terms over all grid boxes within the troposphere or over the surface, respectively.

Using the chemical tropopause criterion (150 ppbv O_3 threshold), our tropospheric ozone burden for the year 2000 (398 Tg) is about 16% larger than the mean ozone burden of the year 2000 of all models investigated by *Stevenson et al.* (2006). Our values for tropospheric ozone production (loss) of 6084 Tg/yr (5844 Tg/yr) are about 19% (25%) larger. The relatively large ozone loss leads to a net chemical ozone production of only $P - L \approx 240$ Tg/yr whereas *Stevenson et al.* (2006) found a mean value of about 442 Tg/yr. This means that a relatively low ozone deposition and high influx from the stratosphere are at the origin of the high tropospheric ozone burden. Indeed, the ozone deposition in ECHAM5-MOZ (908 Tg/yr) is about 9% lower than the multimodel mean of *Stevenson et al.* (2006). The variability across the models is large. Nevertheless, given the positive bias of near-surface ozone volume mixing ratios in our model, our global annual ozone deposition flux should be larger than the corresponding flux of the other models provided that the deposition velocities are similar. We conclude that our ozone deposition velocities must be on the low side. The influx of ozone from the stratosphere into the troposphere was calculated annually as the residual term $S_{\text{influx}} = L+D-P$ and is 668 Tg/yr for the year 2000. This is about 21% more than the multimodel mean, but apparently not related to artifacts in the ERA40 data which we used to constrain the meteorology (cf. *van Noije et al.*, 2006b). Another simulation using only prescribed sea surface temperatures as input yielded a residual ozone influx of 671 Tg/yr (mean over five years) (*Stevenson et al.*, 2006).

When we apply the thermal tropopause criterion, the tropospheric ozone burden is higher by 12%. This implies that the thermal tropopause is above the chemical tropopause.

4.11 Summary of model evaluation

ECHAM5-MOZ has been evaluated with CMDL CO measurements, satellite observations of the tropospheric NO_x column, vertical ozone profiles from ozone sondes, aircraft measurements (GTE and MOZAIC), and surface ozone concentrations from various data centers. Although there is a bias of the model towards high ozone concentrations, the phase and often also the amplitude of the seasonal cycle in CO volume mixing ratio, NO_x tropospheric column and ozone volume mixing ratio is successfully simulated. The spatial variability of the NO_x tropospheric column is well represented by the model (high spatial correlation compared to 17 different atmospheric chemistry models). The simulated ozone volume mixing ratio shows the ozone wave one pattern and the correct phase of the seasonal cycle in the free troposphere for most of the ozone sonde stations, but the amplitude is often somewhat too large. The CH_3CCl_3 and CH_4 lifetimes are shorter by 12% and 19% compared to the values reported by *Prinn et al.* (2001); *Stevenson et al.* (2006), respectively. The comparison of the ozone budget with other models reveals a comparatively high chemical ozone production and loss but a low ozone deposition.

5 Variability and trends

5.1 Surface CO

In Fig. 15, we show the CO anomalies of the model (blue) and the NOAA ESRL-GMD measurements for the years 1980 to 2000. Similar to the study of *Koumoutsaris et al.* (2008), the anomalies are calculated with respect to the mean over the time period for which both, measurements and simulated values are available. The thin lines represent monthly median values, the dots are 6-months running mean values based on the monthly medians. The decrease in CO volume mixing ratio at the stations on the northern hemisphere (Barrow, Mace Head, Hungary, to a lesser extent at St. Davids and Ulan Uul) during the 1990s is well reproduced by our simulation. It is caused by decreasing anthropogenic CO emissions in Europe and N-America (*Duncan et al.*,

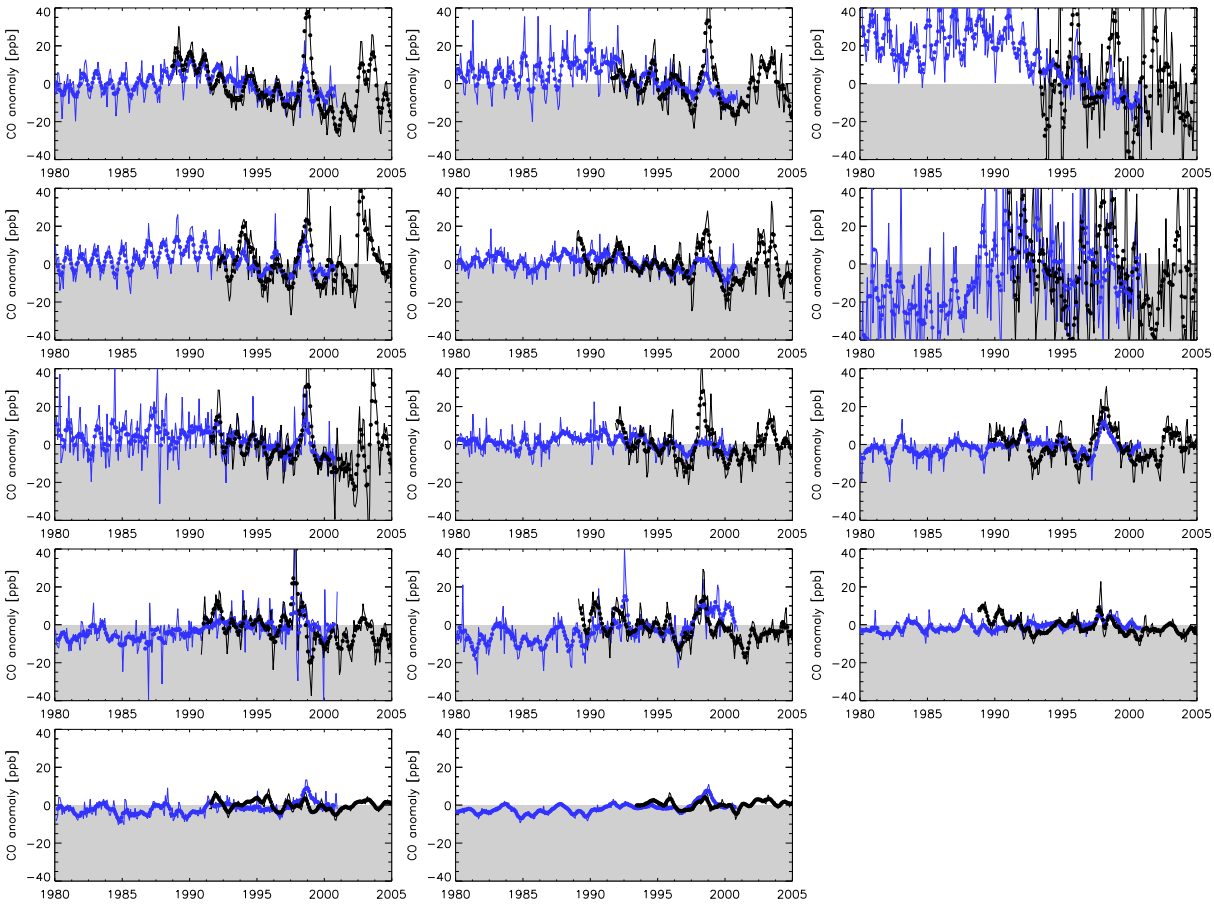

Figure 15: CO anomalies with respect to the time period for which both measurements (black) and simulated values (blue) are available. Thin lines: monthly medians, points: 6-months running means of monthly medians. From top to bottom and left to right: Barrow, Mace Head, Hungary (Hegyhatsal), Ulan Uul, Niwot Ridge, Tae-ahn peninsula, St. Davids Head (Bermuda), Izaña (Tenerife), Mauna Loa, Seychelles, Ascension, Samoa, Cape Grim, South Pole.

2007; *IPCC*, 2001; *Koumoutsaris et al.*, 2008). Varying biomass burning CO emissions are at the origin of the high interannual variability of surface CO volume mixing ratios. The large biomass burning event in the norhern hemisphere 1998 (*Yurganov*, 2004; *Duncan et al.*, 2007) generate the large positive anomaly observed at Barrow, Mace Head, Hungary, Ulan Uul, Niwot Ridge, St. Davids in 1998/1999. This anomaly is well represented in our simulation although its strength is underestimated. Similarly, the large fires in Indonesia following the dry season associated with the El Niño 1997/1998 (*Duncan et al.*, 2003; *Schultz et al.*, 2008a) caused the highly positive CO anomaly at the Seychelles and Samoa measurement stations. It is well captured by our simulation, indicating a good representation of the corresponding CO emissions and the associated transport.

5.2 Tropospheric ozone

The linear trend for the 1990s calculated from monthly mean values is also shown in Fig. 1. It appears to be very high over the biomass burning regions of the southern hemisphere and the south eastern United states (2-4%/year), but consistent with the trends described by *Oltmans et al.* (2006); *IPCC* (2001) for the other regions: There is almost no or a slightly negative trend in Europe and Japan and a positive trend in large parts of the southern hemisphere.

The global average decadal mean tropospheric ozone column increased by 4.1 DU from the

1960s to the 1990s. The NO_x and CO emissions in the 1960s are about 61% and 74% of the emission in the 1990s, respectively. In preindustrial times, Gauss et al. (2006) assume about 32% and 26% of the 1990s NO_x and CO emissions, respectively. They report an increase of 7.9-13.8 DU which is consistent with our value.

Seven years of MOZAIC data that overlap with our simulation period (Fig. 12) show a considerable interannual variability but no obvious trend. E.g., a two peak structure at 250 hPa at Brussels in the early year of 1998 or at 500 hPa at Bangkok during the first months of 1996. Many of these features are also present in our simulation, but the varibility appears to be higher in the measurements.

5.3 Surface ozone

The data set of the station Mace Head at the West coast of Ireland received the attention of various authors, because these data are believed to reflect changes in the hemispheric background concentrations of tropospheric ozone which are supposedly linked to large-scale emission changes (*Simmonds et al.*, 2004; *Carslaw*, 2005; *Oltmans et al.*, 2006; *Derwent et al.*, 2007; *Parrish et al.*, 2009).

All of these studies found a significant increase in the annual mean ozone concentrations at Mace Head ranging from about 0.26 ppbv/yr (*Oltmans et al.*, 2006) to 0.49 ppbv/yr (*Simmonds et al.*, 2004). These differences in the calculated trends are caused by different filtering and statistical processing of the data and by slight differences in the length of the analyzed measurement period. All authors find the largest ozone increases at Mace Head in winter and spring and in prevailing westerly wind conditions. In our analysis of the Mace Head ozone data from 1990 to 2000 (beginning of the data set available on the EMEP data center to end of the RETRO model simulation) we used a simple linear regression on the seasonal or annual mean data to compute the trend and we report the 2-sigma value of the fit as uncertainty estimate. We also experimented with a robust, non-parametric regression method (*Cleveland et al.*, 1990), but the results from this method are not always easy to interpret and the low-frequency trend signal usually agrees well with the linear fit. For simplicity we therefore report only the results from the linear regression. For the Mace Head ozone data we find an annual mean trend of 0.22 ± 0.24 ppbv/yr when all data are considered and 0.31 ± 0.24 ppbv/yr when the data are filtered for westerly winds (wind direction taken from the model simulation). The winter trend for westerly winds is 0.65 ± 0.20 ppbv/yr, in close agreement with the value reported by *Simmonds et al.* (2004), who report a trend of 0.63 ± 0.31 ppbv/yr for the period 1987–2003.

The interannual variability of the annual and seasonal mean ozone concentrations at Mace Head is about 2 ppbv and 2–8 ppbv, respectively (Figure 16, top). The largest variability occurs in the winter data. 1997 is a local minimum for all seasons except winter, where the lowest average concentrations were measured in 1996. In the ECHAM5-MOZ simulation, many features of the interannual variability are captured very well (except in spring), but the model results do not reproduce the trend component. In contrast to the observations, there is no significant trend in any season nor in the annual mean results (Figure 16, bottom). This conclusion remains true even if we filter the model results for westerly winds or select only the daytime values (not shown here, but graphs available at `ftp://ftp.retro.enes.org/pub/documents/trend_eval`).

Jaffe et al. (2007) performed a trend analysis on surface ozone measurements at remote sites in the US and found a significant increase in the background ozone concentrations at seven out of the eleven sites that were investigated. The strongest trend signals were detected for Rocky Mountain National Park (0.51 ppbv/yr), Yellowstone (0.50 ppbv/yr) and Lassen Volcanic Park (0.33 ppbv/yr). These three sites had data from 1987–2004 at the time of the publication. In our linear regression analysis, the observed trends from 1987–2000 are 0.44 ± 0.46, 0.81 ± 0.29 and 0.81 ± 0.27 ppbv/yr, respectively. These trends are larger than those found by *Jaffe et al.* (2007), but in any case they are all strongly positive. In contrast, the model results again show

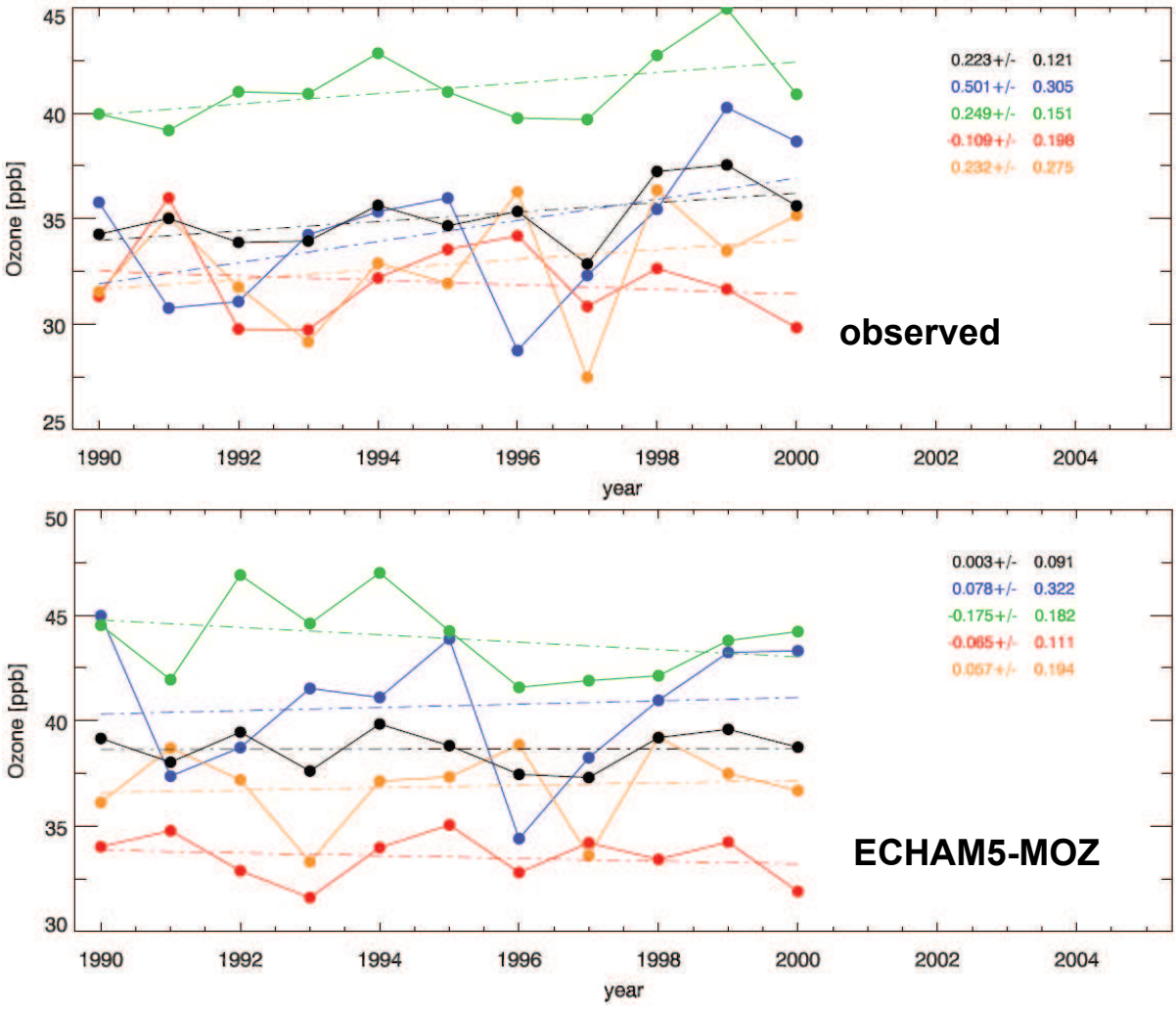

Figure 16: Annual mean and seasonal mean trend and interannual variability of observed (top) and simulated surface ozone concentrations at Mace Head, Ireland. The trend lines were computed with simple linear regression, uncertainties are 1-sigma values. Black: annual mean, blue: winter (DJF), green: spring (MAM), red: summer (JJA) and orange: fall (SON).

no significant trend signal for any of these three stations. The linear regressions yield 0.09 ± 0.18, 0.11 ± 0.17 and 0 ± 0.20 ppbv/yr, respectively. Without showing this here, we note that the model again captures some features of the interannual variability, although the pattern agreement is less good than at Mace Head. In particular, the minimum concentrations observed at Yellowstone and Rocky Mountain National Park in 1989/1990 are only partly reproduced for the first, but not at all for the second of these sites.

In the study of *Jaffe et al.* (2007), there was no trend signal for two stations in Alaska: Barrow and Denali National Park. This is confirmed by our analysis of the observed data. Also the model shows no significant trend at these sites, although the trend for Denali is almost significantly positive.

Figure 17 provides a summary of our evaluation of the annual mean surface ozone trends at several low-altitude and mountain sites around the world. Without going into a detailed discussion here we note that a general pattern emerges which has been found already for the more detailed comparisons described above: while many stations in the mid-latitudes and subtropics show a significant increase in the ozone concentrations during the 1990s, the model captures a significant trend only at the US National Park Service station Craters of the Moon. At most sites, the model underestimates the observed trend, but it yields a larger slope at CASTNET site Cranberry and at Mauna Loa. If we believe in the temporal evolution of the ozone precursor emissions that were used in the model simulations, we must conclude that the model either misses an important aspect of the circulation that would have led to increasing surface ozone concentrations in the 1990s (e.g. changes in the stratosphere-troposphere exchange or tropopause heights (*Koumoutsaris et al.*, 2008)) or it misses some other aspect of the tropospheric ozone chemistry that would have exhibited large changes during the 1990s. An obvious candidate here would be aerosol processes and their interaction with the ozone chemistry through radiation changes, heterogeneous reactions and in-cloud oxidation (*Pozzoli et al.*, 2008a,b). It will be interesting to repeat the long-term simulations with a fully coupled aerosol and gas-phase chemistry model. Another possible explanation for the discrepancy between the observed and simulated trends would be a fundamental flaw of the model in the response to emission changes. These could occur because of unresolved topographic effects and non-linearities in the ozone chemistry (cf. *Wild et al.*, 2006). Since our model does not differ much from other models with respect to the ozone response to large-scale emission changes (*Fiore et al.*, 2009), this would be a problem of all global models. Of course we cannot rule out errors in the time series of the emission data either. In fact, there are some indications that the strong rise in Asian CO and NO_x emissions beginning in the mid-1990s (*Richter et al.*, 2005) is underestimated in the RETRO inventory (see *RETRO-1.6*, 2007). We close this paragraph by noting that other simulations of the 1990s ozone trend also failed to reproduce the observations. Neither the RETRO simulations with the LMDz-INCA and TM4 models (Szopa et al., manuscript in preparation) nor the GEOS-Chem simulations described by *Koumoutsaris et al.* (2008) show any indication of rising background ozone concentrations during the 1990s.

5.4 Global ozone budget

The tropospheric ozone burden (Fig. 18) shows an increase over the period 1960-2000 from about 346 Tg(O_3) to 398 Tg (chemical tropopause criterion). The slightly higher positive slope in the tropospheric ozone burden according to the thermal tropopause for the period 1960 to 2000 shows that the thermal tropopause is either faster increasing in altitude than the chemical tropopause or that there is a significant increase in the ozone concentration between the chemical and thermal tropopause.

The ozone production (loss) increases from about 4848 Tg/yr (4684 Tg/yr) to 6082 Tg/yr (5840 Tg/yr) during the period from 1960 to 2000. Ozone gross production and loss are highly correlated ($R^2 = 1.0$). The interannual variability is rather large and reflects some of the

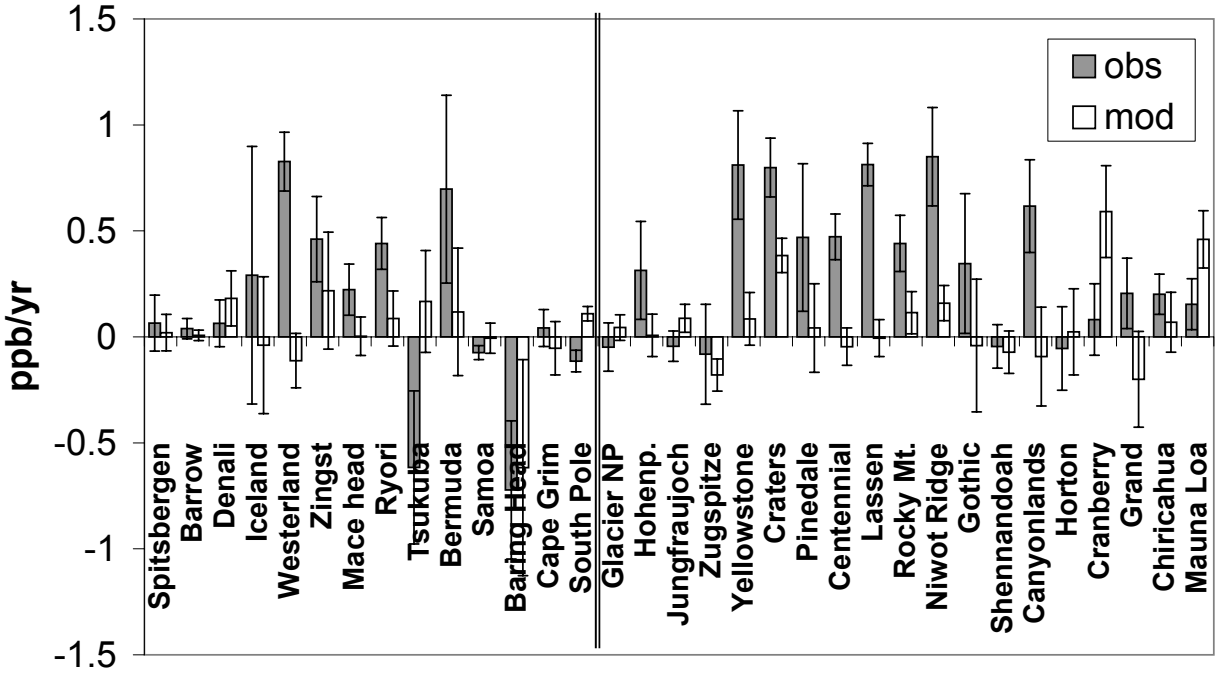

Figure 17: Summary of the linear regression trend analysis of annual mean surface ozone concentrations at several low-altitude (left) and mountain (right) stations around the world. The boxes indicate the slope of the linear regression curves computed from the start of the respective measurements until the end of 2000 or the end of the available data. The error bars show the 1-sigma uncertainty of the linear fits.

variability in the emissions. E.g., there is a local maximum in ozone production and loss during the year 1997 in which particularly high biomass burning emissions occurred. The ozone burden is also highly correlated with the gross ozone production (R^2=0.97).

Ozone deposition and influx from the stratosphere do not show a consistent trend like P and L. From this, we conclude that the change in the ozone burden during the time period of 1960-2000 is primarily caused by larger emissions and not by changes in the dynamics of the atmosphere.

It is unclear if the variability of the stratosphere troposphere exchange flux is real or whether it is related to artefacts in the ERA-40 meteorology (cf. *van Noije et al.*, 2004, 2006b). A comparative simulation driven only by sea surface temperature observations could potentially yield some insight into the issue. Such a simulation has been reported by *Grewe* (2007) using an older version of the ECHAM model with coarser resolution and less detailed emission inventories. They do not report annual stratosphere-troposphere exchange rates, but their analysis of the southern hemisphere ozone influx from the stratosphere shows a periodic pattern with minima around 1965, 1975, 1984 and 1993, which they attribute to the 11-year solar cycle. In our simulation we find minima of the stratosphere-troposphere exchange flux in 1964, 1975, and 1985. The amplitude of these variations is comparable in both studies.

6 Correlation between regional emission and concentration changes

According to the RETRO inventory of ozone precursor emissions (including natural emissions computed interactively by the model), global NO_x emissions increased from 21.2 TgN/yr in 1960 to 40.2 TgN/yr in 1980 and 41.9 TgN/yr in 2000 (see Tab. 1). The modest increase in the second half of this period masks some important regional changes. In particular, NO_x emissions

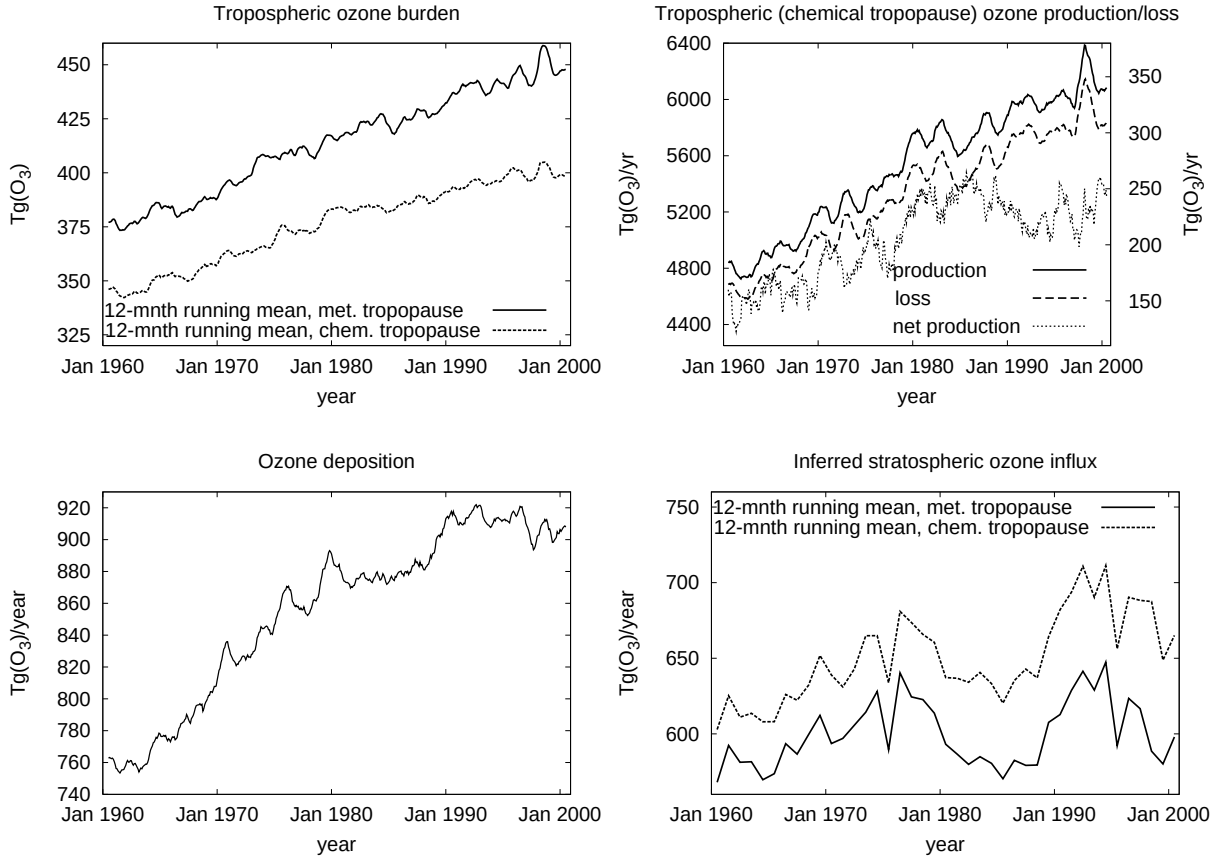

Figure 18: Tropospheric ozone burden (top left), tropospheric chemical production, loss, and net production (right y-axis) of ozone (top right), ozone surface deposition (bottom left) and inferred stratospheric influx (bottom right) for the period 1960-2000. In all cases, 12-month running means are shown. Further explanation in the text.

Table 11: Regional mean values of annual NO_x and CO emissions, emission densities and averaged surface concentrations of NO_x, CO, and Ozone for 1960, 1980 and 2000.

region	NO_x emissions		CO emissions		NO_x	CO	Ozone
	[Tg(N)/yr]	[g(N)/m^2/yr]	[Tg(CO)/yr]	[g(CO)/m^2/yr]	[pptv]	[ppbv]	[ppbv]
			1960				
East Asia	4.3	0.12	69	6.1	208	120	44
Europe	7.5	0.56	47	11.5	732	123	43
N-America	14.4	0.23	110	10.6	332	110	40
			1980				
East Asia	8.4	0.23	95	8.5	357	145	53
Europe	15.4	1.14	65	15.9	1600	155	51
N-America	23.0	0.36	156	8.0	547	132	47
			2000				
East Asia	15.5	0.42	117	10.3	622	151	57
Europe	13.1	0.98	36	8.9	1175	125	52
N-America	21.0	0.33	90	4.6	508	119	48

tended to decrease in the United States and parts of Europe, whereas East Asia and other developing regions showed a strong increase in NO_x emissions in particular after 1980. Global CO emissions were 913 TgCO/yr in 1960, rose to 1179 TgCO/yr in 1980 and showed a small decline afterwards. The year 2000 global CO emission total is 1114 TgCO/yr (see Tab. 2).

In the following we concentrate on the three continental scale regions in the northern hemisphere where most of the ozone precursor emissions occurred. We investigate the relationship between emission changes and the changes in the boundary layer ozone concentration averaged over these regions. We computed regionally averaged annual emissions, normalized them to the respective surface area (in the following labeled as "emission density") and relate them to annual mean surface concentrations of NO_x, CO and ozone. The three regions are: East Asia (consisting of China, Hong Kong, North and South Korea, Macau, Mongolia and Taiwan as in the EDGAR3 inventory; see `http://www.mnp.nl/edgar/documentation`[7]), EC25 Europe (Austria, Belgium, Cyprus, Czech Republic, Denmark, Estonia, Finland, France, Germany, Greece, Hungary, Ireland, Italy, Latvia, Lithuania, Luxembourg, Malta, The Netherlands, Poland, Portugal, Slovakia, Slovenia, Spain, Sweden, United Kingdom) and North America (Canada and the US). Country outlines interpolated to the model grid were used to compute the averages, so that no ocean grid boxes enter the analysis. Table 11 provides an overview on the emissions and concentrations in the respective regions for 1960, 1980, and 2000.

In Figure 19 the relationship between emission density changes and concentration changes is shown. During the first half of the study period, NO_x and CO emission increases are rather linearly correlated in all three regions (correlation coefficients $r^2 \geq 0.93$). After 1980, the increase continued in East Asia (albeit with a slightly smaller slope), while Europe and North America experienced a decrease in both emissions. The decrease in the CO emissions was much stronger than the decrease in NO_x emissions, so that the slope of the correlation is steeper.

As can be expected from the short lifetime of NO_x in the atmosphere, the NO_x emissions and NO_x concentrations correlate very well and the slopes between the emission densities and area-averaged concentrations are similar in the three regions. After 1980, the correlation slightly deteriorates in Europe and North America and in Europe also the slope changes. Apparently this is caused by the strong regional differences in European emission changes (Figure 20). For example, NO_x emissions in Germany and the UK decreased by about 30% between 1980 and 2000, while the emissions increased by 4 and 11% in Italy and Spain, respectively. Different policies regarding the introduction of catalysts and the evolution of heavy duty vehicles versus passenger car traffic lie behind these patterns.

[7]last accessed 2014-05-08

The relationship between the NO_x emission density and the CO concentrations resembles that between NO_x and CO emissions only that CO concentrations in North America do not decrease to levels of 1960 after 1980 as the emissions do. This points to a large-scale rise in the CO background concentration caused by emission changes in Asia and increased photochemical formation from methane and other volatile organic compounds.

Interestingly, the simulated ozone response to the changes in the NO_x emission density varies quite strongly with region and time. While all three regions show a strong positive correlation in the early period ($r^2 \geq 0.88$), the slopes differ strongly. Europe, with the highest density of NO_x emissions, shows the weakest response in average surface ozone concentrations while East Asia, having the lowest density, shows the largest response. In fact, the inverse average NO_x emission density correlates very well with the fitted slope ($r^2 = 0.986$). After 1980, the pattern changes markedly: while in East Asia the positive correlation continues with reduced slope (NO_x emission densities are now similar to North America before 1980, but the slope is only about 1/2), there is practically no ozone response to changing NO_x emissions in Europe and a tendency for higher ozone concentrations under lower NO_x conditions in North America. These results support the finding from the surface ozone trend analysis that emission reductions in Europe and North America have not led to a decrease in the mean ozone concentrations and they strongly suggest that ozone has largely been controlled by other factors in the 1980s and 1990s. Two hypotheses that have been brought forward in the literature are the impact of rising methane concentrations (e.g. *Fiore et al.*, 2002) and changes in the stratospheric and tropospheric circulation (e.g. *Koumoutsaris et al.*, 2008). Without further sensitivity studies and a better model representation of the observed ozone trends, these hypotheses cannot be tested against each other.

7 Conclusions

The newly developed tropospheric chemistry general circulation model ECHAM5-MOZ has been used to simulate the evolution of tropospheric ozone and its precursors from 1960 to 2000. This paper provides a description of the model, the emission data and simulation setup before presenting an in-depth model evaluation with various data sets from surface stations, ozone sondes, aircraft and satellite. The evaluation is mostly limited to the 1990s because of data availability. Based on bias statistics, correlation analysis and comparison to other global chemistry models, we conclude that ECHAM5-MOZ captures many important features of the tropospheric chemical composition (e.g. seasonal cycles, latitudinal gradients, etc.). However, the model exhibits a persistent high bias in ozone which we attribute to excessive influx of ozone from the stratosphere and a relatively low dry deposition flux at the surface. Furthermore, the seasonal cycle of CO shows a severe underestimation of wintertime concentrations in the middle and high latitudes of the northern hemisphere. Global mean OH concentrations are about 15% larger than the average of 25 global models compared recently by *Stevenson et al.* (2006). Methane and methylchloroform lifetimes are about 12% shorter. This is a combined effect of the ozone and CO biases and the location of the tropical maximum of OH which is situated at lower altitudes compared to the multi-model mean.

The interannual variability of regional aggregated tropospheric NO_2 columns is well captured compared to GOME retrievals by KNMI/BIRA. The analysis of surface CO anomalies shows a good correspondence with NOAA-GMD measurements: the model captures the generally decreasing CO trend during the 1990s and reproduces the hemispheric-wide maximum concentrations in 1997 and 1998, albeit with a lower amplitude than the observations (see *Koumoutsaris et al.* (2008) for comparison with results from another model).

The global average decadal mean tropospheric ozone column increased by 4.1 DU from the 1960s to the 1990s consistent with the results of 10 other models reported by Gauss et al. (2006) when our trend is scaled to the emission changes since preindustrial times. Simulated surface

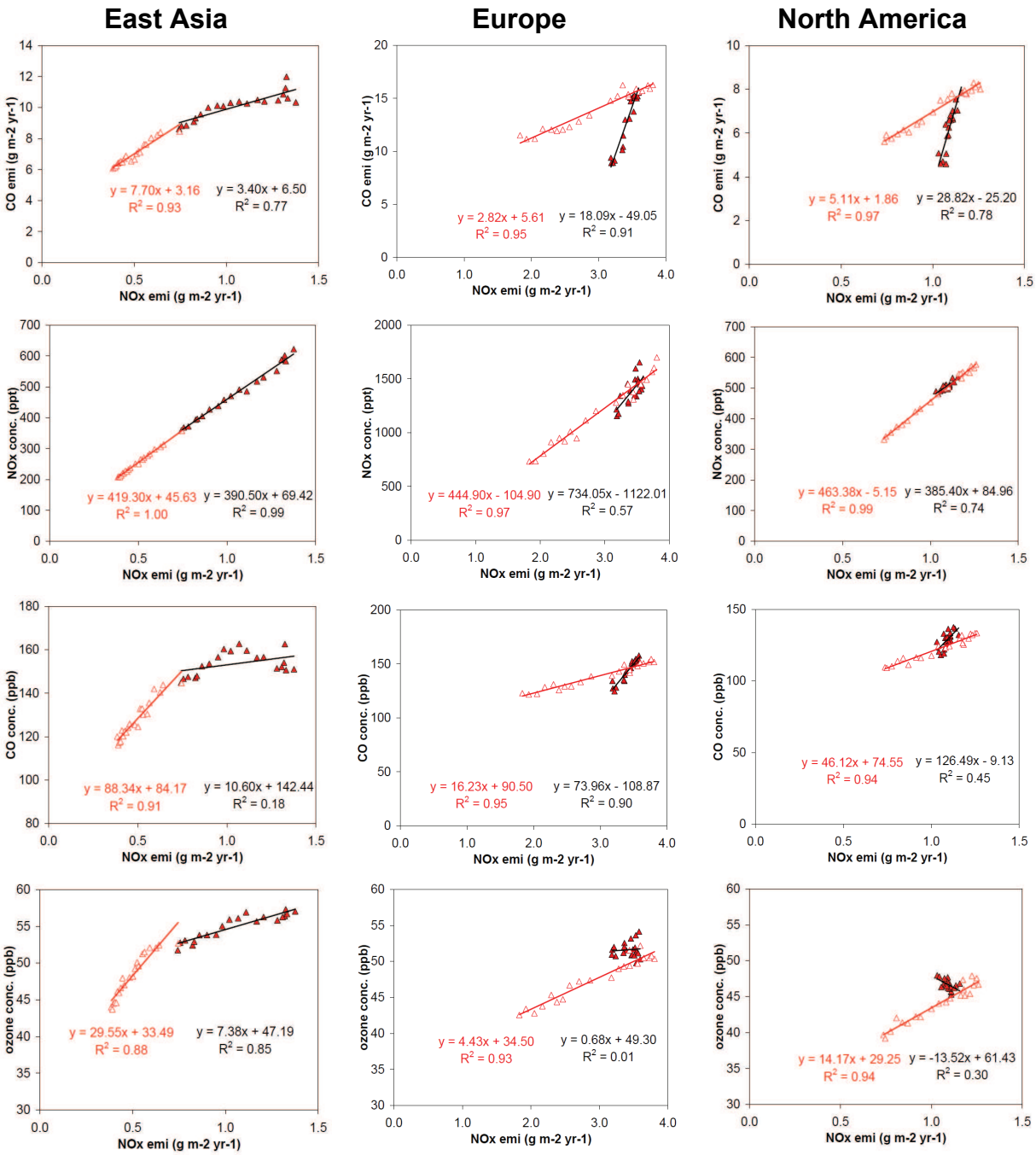

Figure 19: Correlation between regionally averaged ozone precursor emission changes and the concentration changes of NO_x, CO and ozone in East Asia, Europe and North America. The correlations were computed separately for the period 1960–1980 (open symbols and red line) and 1980–2000 (filled symbols and black line), respectively. Emissions were normalized by the land-surface area of each region. The regions were defined based on country outlines mapped onto the model grid. Top row: normalized NO_x emissions versus normalized CO emissions, second row: normalized NO_x emissions versus surface NO_x mixing ratios, third row: normalized NO_x emissions versus surface CO mixing ratios, bottom row: normalized NO_x emissions versus surface ozone mixing ratios.

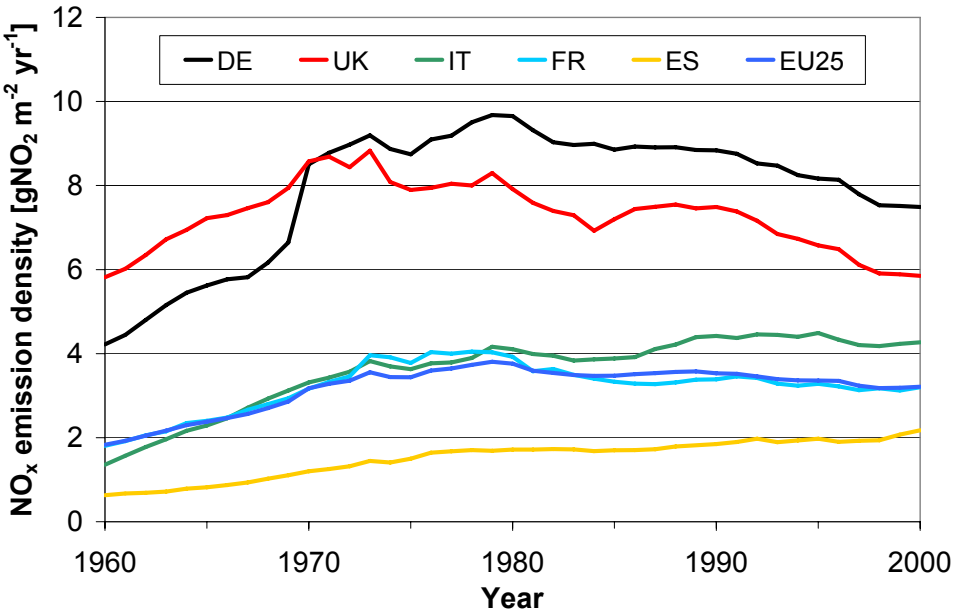

Figure 20: Temporal change of the NO_x emission density in selected European countries (DE: Germany, UK: United Kingdom, IT: Italy, FR: France, ES: Spain).

ozone trends were compared with observations from 33 global background stations, 19 of which were classified as mountain sites. The majority of the observations indicate a significant positive trend in the 1990s, but the model does not capture this. Among the plausible hypotheses for this discrepancy are variations in stratospheric ozone and stratosphere-troposphere exchange that were not captured by our simulation, some aspects of the evolution of surface emissions that we might have missed and possible effects of changing aerosol loads which were not included in our simulation. However, it is also possible that the failure to reproduce the observed surface ozone trends in our simulation indicates a fundamental problem of global models to simulate this quantity which is often strongly impacted by small-scale effects related to the local and regional distribution of emission sources and orography.

Continental-scale precursor emission changes in the northern hemisphere correlate very well with the simulated changes in regionally averaged surface ozone concentrations between 1960 and 1980, but the correlation breaks down afterwards when the rise in NO_x emissions from Europe and North America slows down. Eastern Asia continues to exhibit a significant positive correlation between NO_x emissions and surface ozone concentrations, but the slope changes after 1983. The quantitative relation between the NO_x emission density and the change in surface ozone differs between regions, as a result of the different climatic conditions and regional distributions of emissions.

In spite of the absence of a trend in surface ozone concentrations in our simulation, we find a continuous increase of the global tropospheric ozone burden which follows the gross chemical production and loss. The dry deposition flux increases until the early 1980s and shows a more irregular behavior afterwards. Global net production of ozone increases from about 150 $Tg(O_3)/yr$ in 1960 to 250 $Tg(O_3)/yr$ in 2000 with a mean of 205 $Tg(O_3)/yr$. The net influx of ozone from the stratosphere (diagnosed as residual of the other terms) fluctuates around 650 Tg/yr with an amplitude of 15%.

8 Acknowledgment

The authors would like to thank M. Giorgetta and J. Feichter for helpful discussions. V. Grewe, L. Emmons, the RETRO project team and many other people are acknowledged for providing data, software and analysis tools. The German Climate Computing Centre (DKRZ) and the John von Neumann Institute for Computing (NIC) provided the necessary computing time to perform the multi-annual model simulations. SR and MGS acknowledge funding from the European Commission under contract EVK2-CT-2002-00170 (RETRO) and AMA was funded by the ZEIT foundation. IB acknowledges support by the Swiss National Science Foundation under the grants 2100-067979 and 200020-112231. SR thanks Norbert Noreiks and Bettina Diallo for their help in preparing the figures and printing the manuscript. Finally we thank the reviewers for their commitment and the very helpful comments.

A Detailed model description

The ECHAM5-MOZ coupled Tropospheric Chemistry General Circulation Model (TCGCM) principally consists of the implementation of the chemical scheme of the Model of Ozone and Related Tracers version 2.4 (MOZART2) (*Horowitz et al.*, 2003) into the Atmospheric General Circulation Model (GCM) ECHAM5 (version 5.3.02) (*Roeckner et al.*, 2003). Parameterizations for deposition processes and lightning applied in the MOZART2.4 model were exchanged with other formulations which should be more consistent with the dynamics and physics of the ECHAM5 model.

The model was constructed in a modular fashion so that it is technically easy to replace entire parts of the chemistry and physics by other modules. An aerosol module with seven modes and

five chemical species was described by *Stier et al.* (2005) and has been coupled to the gas-phase chemistry scheme described in this paper (*Pozzoli et al.*, 2008a). The atmosphere model ECHAM5 including its chemistry and aerosol modules can be coupled to an ocean model (MPI-OM) (*Jungclaus et al.*, 2006) and a carbon cycle model and can thus be used in investigations of past climate and future climate scenarios or for the analysis of chemistry-climate feedback processes on longer timescales. In the present version of ECHAM5-MOZ, radiative feedbacks of chemical constituents have not been implemented yet.

In order to achieve a more realistic simulation of specific time intervals the ECHAM5-MOZ model can be constrained by sea surface temperature (SST) and sea ice (SIC) fields derived from other climate simulations or observations. The simulations described in the main part of this paper use a relaxation technique for constraining temperature, vorticity, divergence, and surface pressure (*Jeuken et al.*, 1996; *Machenhauer et al.*, unknown year). Using data from numerical weather prediction models with data assimilation we expect that this technique reproduces large-scale daily weather patterns so that the GCM behaves similar to an offline chemistry transport model (CTM).

This appendix provides a description of the main components of ECHAM5-MOZ. An evaluation of the model is contained in the main text of this paper and in section C of this Appendix. Further comparisons of the model with observations from specific field measurements are reported in (e.g. *Auvray et al.*, 2007; *Aghedo*, 2007; *Pozzoli et al.*, 2008b; *Stier et al.*, 2005).

A.1 Dynamics, physics and tracer transport

A detailed description of the general circulation model ECHAM5 and its sensitivity to model resolution is given by *Roeckner et al.* (2003, 2006); *Hagemann et al.* (2005). The dynamical core of the model solves the prognostic equations for divergence, vorticity, temperature, and the logarithm of the surface pressure in the spectral space. The vertical axis consists of a hybrid coordinate which follows the terrain near the surface of the earth and gradually becomes a pure pressure coordinate near 50hPa. The "midpoint" pressure of the topmost level is 10hPa. Standard vertical resolutions comprise 19 or 31 levels. *Roeckner et al.* (2006) tested the general circulation of ECHAM5 in various combinations of horizontal and vertical resolution and found that for the triangular spectral truncation T42 which we used in our simulations the differences between the 19 and 31 level model are small. We decided to use the 31 level version in order to better resolve vertical tracer gradients. The spectral truncation of T42 corresponds to a grid resolution of about $2.8^\circ \times 2.8^\circ$. Physical and chemical processes are computed on a gaussian grid. The model time step is 20 minutes.

A.2 Operator splitting

The system of advection-diffusion-reaction-convection partial differential equations describing the transport, physical processing and the reactions of chemical species in the atmosphere is solved using an operator splitting technique. Denoting the advection, diffusion, reaction, and convection operators for a single time step Δt by $\mathcal{T}_{\rm a}^{\Delta t}, \mathcal{T}_{\rm d}^{\Delta t}, \mathcal{T}_{\rm r}^{\Delta t}, \mathcal{T}_{\rm c}^{\Delta t}$, respectively, the tracer concentrations $c_{t+\Delta t}$ at time $t + \Delta t$ are calculated from the known tracer concentrations c_t at time t by

$$c_{t+\Delta t} = \mathcal{T}_{\rm c}^{\Delta t}\mathcal{T}_{\rm r}^{\Delta t}\mathcal{T}_{\rm d}^{\Delta t}\mathcal{T}_{\rm a}^{\Delta t}c_t. \tag{3}$$

This operator splitting scheme is computationally more efficient but may be less accurate than the classical Strang splitting (*Lanser et al.*, 1999). Up to now no systematic evaluation of the operator splitting in ECHAM5 (which is similar in many other models) exists to our knowledge.

The advection of the trace gas species is computed with the semi-Lagrangian flux form scheme of *Lin et al.* (1996) which theoretically ensures conservation of tracer mass. However, changes in surface pressure lead to vertical grid changes and the associated numerical interpolation errors may violate this mass conservation. We find that the rate of change in the global tracer mass is generally small compared to the tendencies due to emissions, chemistry, and deposition and constitutes at most 0.1% of the emission term in global budget analyses. Larger errors may occur in simulations including a budget analysis of shorter-lived tracers.

The vertical diffusion equation in ECHAM5 has been extended to account for the net tracer flux at the surface resulting from dry deposition and surface emissions. The transport due to turbulent vertical diffusion is calculated in analogy to the vertical heat diffusion as described by *Roeckner et al.* (2003). Emissions occuring above the surface are inserted as mass tendency into the respective gridboxes. The biomass burning and biogenic emissions are inserted in the respective model grid boxes before the performance of the vertical diffusion computation. The aircraft emissions are released as a source term in the system of chemical kinetic equations. The lightning emissions are calculated after the convection computation and are therefore injected after the convection. A detailed description of the various emissions used in the long-term simulations is given in section 3.

The convective transport of tracers is implemented in the ECHAM5 Tiedke convection scheme including some modifications by Nordeng for penetrating convection (*Tiedke et al.*, 1989; *Nordeng*, 1994; *Roeckner et al.*, 2003). Humidity and chemical tracers are transported with identical parameterizations.

A.3 Dynamical relaxation ("nudging")

The nudged variables temperature, vorticity, divergence, surface pressure and sea surface temperature are provided every 6 hours and interpolation with cubic splines is performed between these times. The variables are nudged at all model levels. The respective relaxation times depend on the variable. We use a relaxation time of 6 hours for the vorticity, 48 hours for the divergence, 24 hours for the temperature and 24 hours for the logarithm of the surface pressure, respectively. These are the default relaxation times in ECHAM5 as they are published by *Guldberg et al.* (2005). An analysis of the effect of this relaxation was performed by *Guldberg et al.* (2005). The inverse relaxation times tend linearly to 0 in the middle of the nudging time interval of 6 hours and increase linearly to the full value towards the next time at which nudging data are available. A more general discussion about the choice of the relaxation times is given by *Machenhauer et al.* (unknown year).

A.4 Chemistry

The chemical species, reactions, kinetic equations, and the solver are those of the MOZART2 tropospheric chemistry model *Horowitz et al.* (2003). The model contains 63 transported species and 168 reactions. The chemical mechanism explicitly includes the oxidation of C_2 and C_3 alkanes and alkenes and defines a surrogate C_4 alkane which represents all alkanes, alkenes and aromatics. Reactions of isoprene and α-pinene as a surrogate for all monoterpenes are included. Several oxigenated volatile organic compounds are included in the mechanism. As in MOZART2, the heterogeneous reaction of N_2O_5 on sulfate aerosols is included using the same aerosol distribution of *Tie et al.* (2001) and a reaction probability $\gamma = 0.04$ (*Tie et al.*, 2003) for all years.

The photolysis rates of ozone, NO_2, CH_2O, etc. are calculated from tabulated values which were derived from the Tropospheric Ultraviolet and Visible radiation model (TUV, version 3.0) (*Madronich et al.*, 1998) including the update of the quantum yield of $O(^1D)$ from the photolysis of ozone as described by *Horowitz et al.* (2003). A cloud correction term is applied as in the original MOZART 2.4 code.

The chemical scheme of ECHAM5-MOZ can be modified easily due to the MOZART2 preprocessor that produces optimized source code for a variety of different computer platforms and architectures (e.g. vector or parallel) from a user-given input file. For most species, an implicit Euler method is applied for the integration of the kinetic nonlinear differential equations. The kinetic equations describing the loss of CO, CH_4, and H_2 are integrated with an explicit method.

A.5 Upper boundary conditions

The upper boundary conditions are similar to those described by *Horowitz et al.* (2003): Above 200 hPa in the extra tropical regions and above 100 hPa in the tropics, the concentrations of O_3, NO_x, HNO_3, and N_2O_5 are relaxed to climatological zonal mean monthly varying values using a relaxation time of 20 days. We also tested a relaxation time of 10 days and found negligible changes for tropospheric concentrations of O_3, NO_x, HNO_3.

A.6 Dry deposition

The uptake of trace gases in each grid box is treated separately for vegetated land surfaces, bare soils, water, and snow/ice using a resistance model following *Wesely* (1989) and *Ganzeveld et al.* (1995). Table 12 lists the Henry constants and reactivity coefficients used in the dry deposition scheme. The total dry deposition flux is imposed as boundary condition in the vertical diffusion equation (see section A.1).

A.7 Wet deposition

Wet deposition is calculated for all water soluble species like HNO_3, H_2O_2 and other polar molecules. For most species a thermodynamic equilibrium between the gas (g) and liquid (l) phase will be reached within the precipitating cloud. Any further uptake occurring in the precipitation below the cloud is neglected except for HNO_3. For this species, the uptake is solely diffusion-limited and below-cloud precipitation scavenging cannot be neglected.

Re-evaporating rain droplets release all dissolved gases into the ambient air, i.e. we don't account for the effect that some drops may just shrink and concentrate the dissolved gases until saturation is reached.

Our parametrization of tracer scavenging is based on the wet deposition module of *Stier et al.* (2005) which was designed for the wet deposition of aerosols. The concentration $c_i^{(l)}$ of a species i in the liquid phase is determined by its partial pressure p_i in the surrounding air according to Henry's law

$$c_i^{(l)} = k_H p_i, \tag{4}$$

where k_H is the effective Henry constant that takes into account the temperature dependance of the solubility and the potential dissociation of species i in the liquid phase. In ECHAM5-MOZ we use constant Henry coefficients because of the large uncertainties associated with these two effects. For simplicity, absorption on snow and ice is treated identically to absorption in water.

The concentration change $\dot{c}_i^{(g)}$ of a gas phase tracer i is given by

$$\dot{c}_i^{(g)} = -c_i^{(l)} \dot{m}^{(l)} / \rho_{H_2O}, \tag{5}$$

where $c_i^{(l)}$ is the tracer concentration in the liquid phase determined by equation (4), $\dot{m}^{(l)}$ is the autoconversion rate (formation rate of precipitation) in kg(water)/(m^3s), and ρ_{H_2O} is the density of liquid water.

The below-cloud scavenging is effective only for HNO_3 and is parameterized according to (*Seinfeld et al.*, 1998, pp. 1003 ff.). The gas phase concentration $c_{HNO_3}^{(l)}$ of HNO_3 after a certain time t of constant rainfall intensity is given by

Table 12: Henry constant $k_{\mathrm{H}}^{\ominus}$ and reactivity coefficient f_{reac} of various species used in the dry and wet deposition. The temperature dependence of the Henry constant is not taken into account. Species without dry deposition do not have a reactivity constant. PAN=Peroxy-acetyl-nitrate, MPAN=Methyl-PAN, MACR=methacrolein.

species	$k_{\mathrm{H}}^{\ominus}$/(mol/atm)	f_{reac}
O_3	1.03×10^{-2}	1.0
CO	9.81×10^{-4}	0.0
NO	1.93×10^{-3}	1.0
NO_2	1.0×10^{-2}	1.0
HNO_3	2×10^{6}	1.0
HO_2NO_2	1.2×10^{4}	1.0
$CH_3COCHO_2CH_2OHNO$	2×10^{6}	0.1
$CH_2CCH_3CHONO_2CH_2OH$	7.51×10^{3}	0.1
$CH_2CHC(CH_3)(OO^{\cdot})CH_2NO_3$	3.23×10^{3}	-
PAN	3.6	0.1
MPAN	1.7	0.1
H_2	7.8×10^{-4}	0.0
H_2O_2	7.73×10^{4}	1.0
CH_4	1.41×10^{-3}	0.0
CH_3OH	2.2×10^{2}	0.0
CH_3OOH	3.0×10^{2}	0.1
CH_2O	3.23×10^{3}	0.1
C_2H_5OH	2×10^{2}	0.0
C_2H5OOH	3.4×10^{2}	0.1
CH_3CHO	1.29×10^{1}	0.0
$HOCH_2CHO$(GLYALD)	4.1×10^{4}	0.0
CH_3COOOH	5.5×10^{2}	1.0
C_3H7OOH	3.0×10^{2}	0.1
CH_3COCH_3	2.81×10^{1}	0.0
CH_3COCH_2OH	3.23×10^{3}	0.1
CH_3COCH_2OOH	3×10^{2}	0.1
CH_3COCHO	3.2×10^{4}	0.1
C_3H_6OHOOH	3×10^{2}	1.0
$CH_2CHCOCH_3$	4.1×10^{1}	-
$CH_3COCHOOHCH_2OH$	2×10^{6}	0.1
$CH_2CHC(OOH)(CH_3)CH_2OH$	2×10^{6}	0.0
$HOCH_2C(CH_3)$=CHCHO	3.23×10^{3}	0.0
MACR	6.5	-
$HOCH_2COOHCH_3CHCHOH$	9.05×10^{1}	0.1

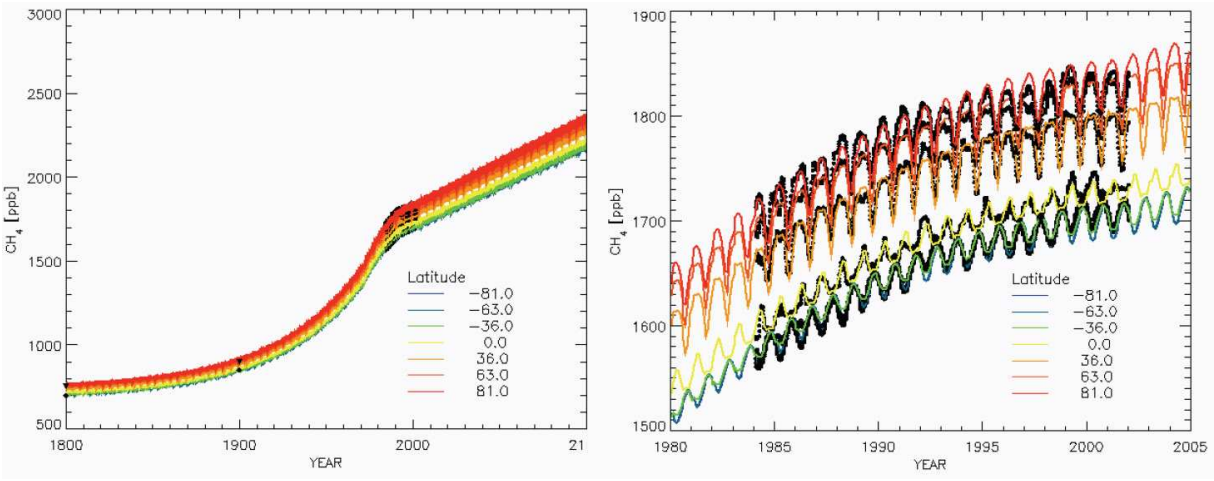

Figure 21: Time series of CH_4 volume mixing ratio for various latitude bands as it is used in the simulation.

$$c^{(g)}_{HNO_3}(t) = c^{(g)}_{HNO_3}(0)\exp(-\Lambda t), \tag{6}$$

where $c^{(g)}_{HNO_3}(0)$ is the HNO_3 concentration at time 0 and Λ is a scavenging coefficient that depends on the rainfall intensity and the rain drop size distribution given in table 20.2 of *Seinfeld et al.* (1998). We fitted the values of Λ as a function of the rainfall intensity r:

$$\Lambda/\Lambda_0 = \alpha(r/r_0)^\beta, \tag{7}$$

with $\Lambda_0 = 1/\text{s}$ and $r_0 = 1\text{mm/s}$. The actual values of Λ_0 and r_0 are arbitrary, but they determine the units of Λ and r. We obtained for the dimensionless fitting parameters $\beta = 0.617$ and $\alpha = 0.0163$. Equation (7) is directly applied to the rainfall rate computed in the convective and large scale cloud modules of ECHAM5.

A.8 Methane boundary condition

Because of the long lifetime of methane in the atmosphere and the difficulties to achieve a balanced global budget of methane sources and sinks in long-term model simulations, methane concentrations were constrained in the planetary boundary layer based on a zonal and monthly mean surface climatology (Figure 21). Surface measurements from the NOAA/ESRL-GMD station network (*GLOBALVIEW-CH4*, 2005; *Dlugokencky et al.*, 1998) were interpolated and extended in time through a combination of fitting procedures. Data for 1800 and 1900 were taken from the IPCC TAR (*IPCC*, 2001). The homogenized time series was constructed by computing a global mean trend in three periods: 1800-1970 (exponential fit); 1970-1998 (second order polynomial fit); 1998-2100 (linear trend with 5 ppb/year increase). Thereafter, the annual mean normalized latitudinal gradient derived from data for 1984-2001 was superimposed and finally the normalized seasonal cycle derived from the same data was applied at each latitude. The model then uses a relaxation approach combining an emission inventory (P. Bergamaschi, personal communication, 2004) with the zonal mean surface concentrations from the climatology (Fig. 21). This approach avoids drifts in the methane concentration and accounts for regional differences at the same time.

B Additional information on emission inventories and parameterizations

Emissions from anthropogenic activities and biomass burning are provided to the model as gridded monthly data files interpolated to the model resolution while biogenic emissions and lightning NO_x are computed online during the model run. Aircraft and biomass burning emissions are injected as mass tendencies into relevant model levels, whereas all other emissions are added as flux term surface boundary condition to the vertical diffusion parametrization.

The inventories of anthropogenic fossil fuel burning and vegetation fire emissions were constructed as part of the RETRO project. They were augmented by existing data sets on international ship traffic emissions, aircraft emissions and natural emissions (*Müller*, 1992; *Grewe et al.*, 2002; *Endresen et al.*, 2003; *Lathière et al.*, 2006). Here we give a general overview about the RETRO emission data sets. More details are contained in the articles of *RETRO-1.6* (2007), *Pulles et al.* (2007) and *Schultz et al.* (2008a).

All RETRO surface emission data files are available on a $0.5° \times 0.5°$ grid through the Global Emissions Inventory Activity (GEIA) web portal `http://www.geiacenter.org`[8] or on the RETRO project web pages `http://retro.enes.org`[9].

B.1 Anthropogenic emissions

Anthropogenic land surface emissions were derived from the TNO Emission Assessment Model (TEAM) (*Pulles et al.*, 2007), which is essentially a database compiling national energy statistics, sectorized activity levels and technology-dependent emission factors for NO_x, CO and non-methane volatile organic compounds (NMVOC). The main developments within RETRO concerned the extension of the database back in time (including extrapolation from the 1970 data to 1960 for countries that did not report before 1970) and the speciation of the NMVOC emissions in 20 different compound classes per sector. The emission data were reported in 10 aggregated sectors corresponding to the sector definition of the regional air quality model LOTOS (*Schaap et al.*, 2008). They are listed in table 13 together with the corresponding emission categories from the UNFCCC common reporting format.

A specific asset of TEAM is the explicit modelling of the time dependent introduction of alternative technologies into the emission inventory. This allows for the generation of consistent "what-if" scenarios related to specific technology changes. For example, in the RETRO project scenarios were generated for power generation (replacing all coal fired power plants by nuclear technology) and for traffic emissions (exploring the effects of catalysts and various European emission standards). These scenarios are described in the RETRO project report D5-5 (*Dalsoren et al.*, 2007).

The emissions $E_i(t)$ of pollutant i at time t were derived by applying the following equation:

$$E_i(t) = \sum_j \sum_n A_j(t) \times P_{n,j}(t) \times EF_{i,n} \tag{8}$$

where $A_j(t)$ is the activity rate of a specific activity j at time t, $P_{n,j}(t)$ is the penetration rate (fraction) of technology n in activity j and $EF_{i,n}$ is the emission factor for pollutant i from technology n.

Data for a selection of fuels were obtained from the International Energy Agency (IEA). These data cover the period of 1960-2000 for the OECD countries and of 1970-2000 for the non-OECD countries. All activity data were converted to Tera Joule using the IEA conversion factors. Solvent use emission data and residential biomass burning activity data were obtained from a global inventory for anthropogenic NMVOC

[8] last accessed 2014-05-08

[9] last accessed 2014-05-08

Table 13: LOTOS emission sectors as used in the TEAM database and their relation to the UNFCCC common reporting format categories.

LOTOS Group	Description	CRF classification
1	Power generation	1.A.1.a; 1.A.1.b; 1.A.1.c
2	Residential, commercial and other combustion	1.A.4.a; 1.A.4.b; 1.A.4.c
3	Industrial combustion	1.A.2.a; 1.A.2.b; 1.A.2.c; 1.A.2.d; 1.A.2.e; 1.A.2.f
4	Industrial processes	2
5	Extraction distribution of fossil fuels	1.B.2.a.ii; 1.B.2.a.iii; 1.B.2.a.iv; 1.B.2.a.v
6	Solvent use	3.A; 3.B; 3.C; 3.D
7	Road transport	1.A.3.b; 1.A.3.b.v
8	Other mobile sources	1.A.3.a; 1.A.3.c; 1.A.3.d; 1.A.3.e
9	Waste treatment and disposal	6.C; 6.D
10	Agriculture and Landuse change	4.E; 5.A

emissions that has been developed at TNO as input for EDGAR 2.0 and GEIA (`http://themasites.pbl.nl/tridion/en/themasites/geia/emissions_data/nmvoc_groups/index-2.html`[10]). Other information was obtained from the European TROTREP project (no reference available). The emission factors are based on several international emission factor collections which were evaluated by the emissions team at TNO. Technologies were identified as unique combinations of emission factors for CO, NOx and NMVOC for a specific year and for specific country groups, mostly OECD and non-OECD for stationary combustion and 'Western' and 'Non-western' for road transport.

The TEAM web page `http://www.air.sk/tno/retro_pictures/index.php`[11] provides access to some inventory data.

The anthropogenic emissions from the RETRO project also include some estimate of the seasonal changes in anthropogenic emissions, specified through sector-specific monthly time profiles applied uniformly across each latitude. The seasonal cycle amplitude was linearly reduced to zero between 15 deg latitude N and S and shifted by 6 months for the southern hemisphere. The seasonal cycle functions were adopted from the LOTOS model.

A comparison of the RETRO emission estimates with other data sets (e.g. EDGAR version 3.2) is given in the main text and in the RETRO project report D1-6. Emission trend estimates from different inventories will be discussed in a forthcoming publication.

B.2 Vegetation fire emissions

Emissions from the open burning of vegetation were compiled based on statistical reports, fire observations from satellite instruments and a prognostic fire model (*Schultz et al.*, 2008a). The RETRO fire inventory used information on the interannual variability of burned area in 13 continental-scale regions in order to derive annual variations of the global emissions from biomass burning. First, carbon emissions were estimated for three aggregate vegetation classes (forest, shrubland and grassland savanna), then the emission factors from *Andreae et al.* (2001) were used to calculate emissions for 21 ozone precursor and aerosol species. Global carbon emissions range from 1410 to 3140 Tg(C) per year, those of carbon monoxide from 216 to 555

[10] last accessed 2014-05-08
[11] last accessed 2014-05-08

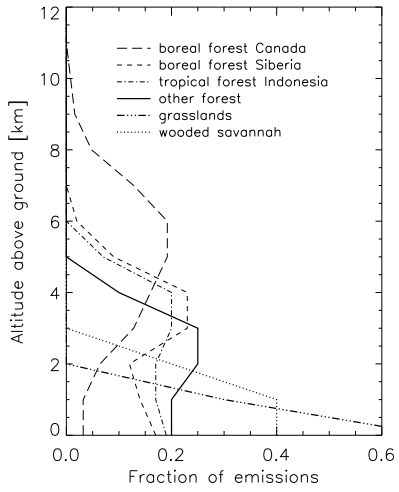

Figure 22: Altitude profile of the fraction of emissions for fires in the different types of ecosystems.

Tg(CO) per year.

The vegetation fire emission estimates for the years 1997–2000 compare well with estimates that were derived from the analysis of Tropical Rainfall Monitoring Mission (TRMM) and Moderate Resolution Imaging Spectrometer (MODIS) satellite data by *van der Werf et al.* (2006) and they are typically within the uncertainties cited by various other studies on regional fire emissions (see paper and supplementary online material of *Schultz et al.* (2008a) for details).

The speciated NMVOC compounds that were used as input data into the ECHAM5-MOZ model simulations (acetaldehyde, acetone, benzene, ethane, ethene, ethyne, formaldehyde, isoprene, methanol, monoterpenes, propane, propene, toluene and xylene, some of these in lumped form) together account for 40–45 % of the total vegetation fire NMVOC emissions found in various field and laboratory measurements (*Andreae et al.*, 2001). Because of the minor role of fire NMVOC emissions compared to biogenic emissions occuring in the same regions no attempt was made to account for the missing fraction.

B.3 Altitude profiles for biomass burning emissions

Smoke plumes from vegetation fires are typically rising to the height of the inversion layer and can in some cases penetrate through the troposphere (e.g. *Folkins et al.*, 1997). For the simulation of emissions from fires this implies that a fraction of these emissions is effectively emitted into higher model levels. For the simulations described in the main text, we extended the ad-hoc parametrization of *Lavoué* (2004) to specify typical vertical injection profiles for fires in various ecosystems. Savanna and grassland fires generally release emissions into the lowest 3-4 km of the atmosphere (some more recent studies even suggest that most plumes are limited to the boundary layer), while forest fires, which may burn with much larger intensity, may inject a fraction of their emissions at altitudes between 5 and 12 km (Figure 22). The altitude profiles are applied independently of season and year. They are prescribed as fractions on a 1 km vertical grid, which are interpolated to the vertical model levels and normalized at each time step.

B.4 Biogenic emissions

Biogenic emissions are calculated interactively using the Model of Emissions of Gases and Aerosols from Nature (MEGAN). We implemented model version 1.0 of MEGAN which is the predecessor of the version described by *Guenther et al.* (2006). Foliage emissions are calculated

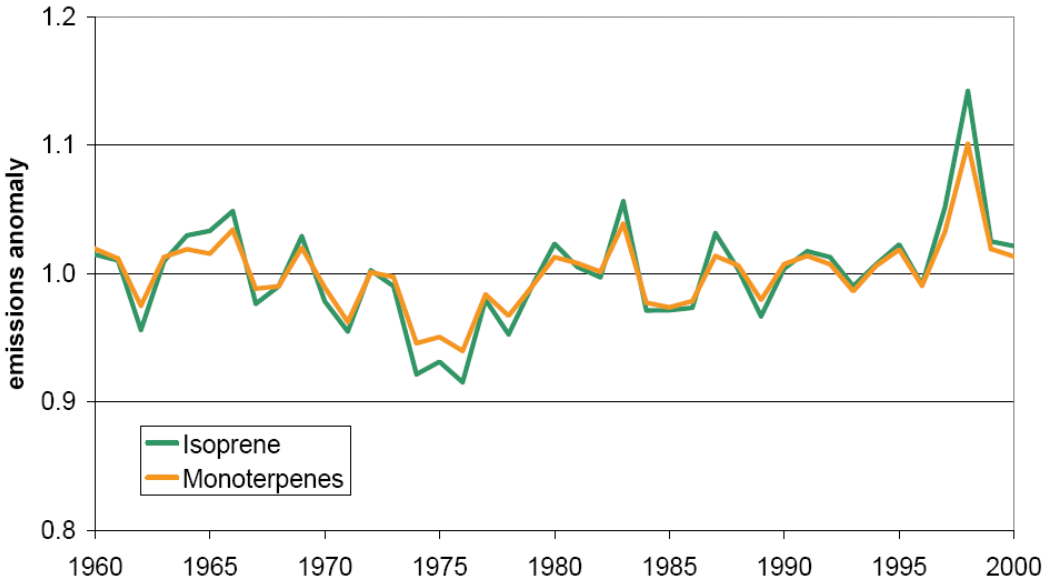

Figure 23: Annual mean emission anomalies of isoprene and terpene calculated with the MEGAN version 1 model by *Guenther et al.* (2006) with respect to the 41-year average.

for isoprene, terpenes and seven other volatile organic compounds (acetone (CH_3COCH_3), acetaldehyde (CH_3CHO), ethane (C_2H_6), ethene (C_2H_4), formaldehyde (CH_2O), propene (C_3H_6), methanol (CH_3OH), as well as for carbon monoxide (CO)). These species yield about 90% of all biogenic volatile organic compound emissions. The emissions depend on the types of vegetation in a grid box which are represented by plant functional types in the model. Six plant functional types (broadleaf trees, fine leaf evergreen trees, fine leaf deciduous trees, shrubs, crops, and grass) were used. The vegetation map was constant for the whole simulation period and is representative for the year 2000.

The emission flux for species i is computed as a function of temperature and incoming shortwave radiation as

$$E_i = \varepsilon_i \times \gamma_i \times \rho_i \tag{9}$$

ε_i denotes a standard emission value for each grid cell which was derived from a more comprehensive modelling study validated by several field experiments (see *Guenther et al.*, 2006). It can be considered as an idealized annual mean of the emissions. The factor γ_i accounts for the seasonal development of the foliage (leaf area index and leaf age) and ρ_i applies an empirical formula to consider the temperature and photosynthetic photon flux (PPF) dependency of biogenic emissions. Note that our γ_i and ρ_i differ from the definition of *Guenther et al.* (2006).

The 41-year average emissions of isoprene and terpenes were 539.1 Tg and 194.7 Tg, respectively. Figure 23 shows the time series of annual mean isoprene and monoterpene emission anomaly.

B.5 Lightning NO_x

Lightning NO_x emissions are parameterized as a function of the average convective updraft velocity w in a model column as proposed by *Grewe et al.* (2001). Starting from the height dependent updraft velocity $w(z)$ in a convective column we calculate $\overline{w}$ as the mean of $w(z)$ over the depth of the cloud d in the column. Following *Grewe et al.* (2001), the flash frequency F can be parameterized as a function of $\overline{w}$ and d:

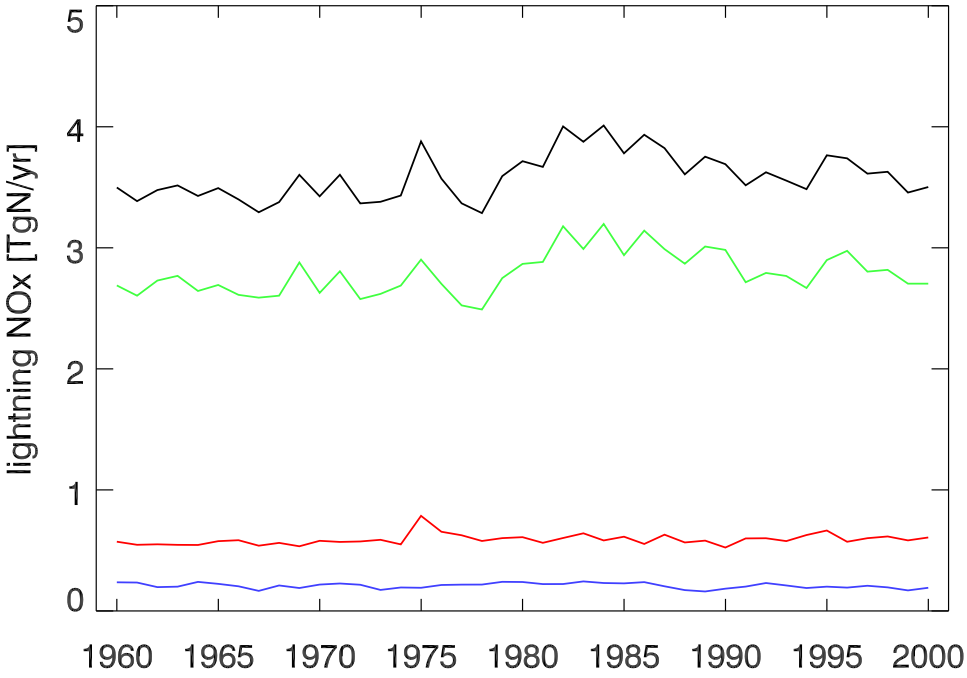

Figure 24: Yearly variation of global and hemispheric lightning emissions from the ECHAM5-MOZ RETRO simulation.

$$F = a(\overline{w}/\overline{w}_0\sqrt{d/d_0})^\beta, \tag{10}$$

with $a = 1.54 \times 10^{-5}$, $\beta = 4.9$, $\overline{w}_0 = 1\,\mathrm{m/s}$, $d_0 = 1\,\mathrm{m}$.

The global average of F depends on $\overline{w}$ and d and therefore on the model resolution. We correct the obtained flash frequency by a uniform factor f, so that the global integral of $F_{\mathrm{eff}} = fF$ is close to observations. For the resolution T42L31, $f = 0.15$.

Lightning emissions are distributed vertically according to the C-shaped emission flux profiles of *Pickering et al.* (1998). The 41-year mean of global lightning NO is $3.4 \pm 0.2\,\mathrm{Tg(N)}$. This is at the low end of the range given in the literature and summarized by *Jacobson et al.* (2009). Figure 24 shows the time series of global and hemispheric lightning NO_x emissions for the simulation described in the main text.

C Additional model evaluation

C.1 Annual anomalies of the tropospheric NO_2 column

The annual anomalies are shown in Fig. 25.

C.2 Vertical profiles from aircraft field campaigns

Carbon monoxide (CO) and hydrocarbons. Observed and simulated vertical CO profiles are shown in Fig. 26.

Observed and simulated profiles of ethane and propane are compared in Fig. 27 and Fig. 28, respectively. These hydrocarbons are emitted from the same combustion sources as CO but have different lifetimes. Observed vertical profiles of ethane are relatively well reproduced in the

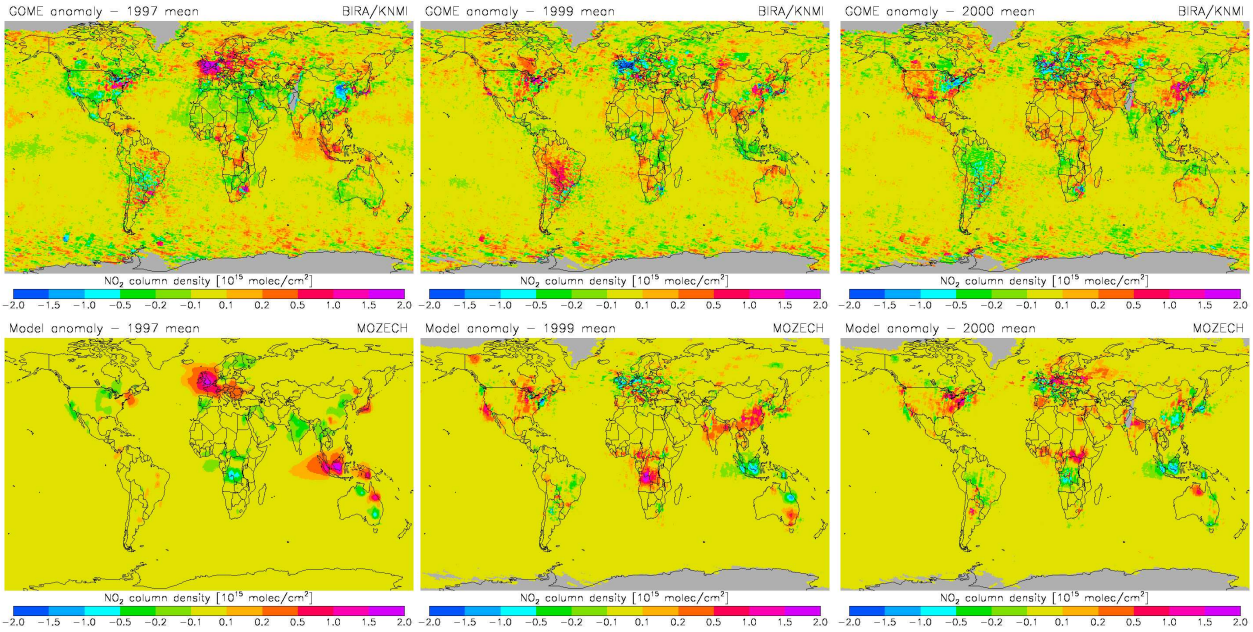

Figure 25: Yearly anomalies for the BIRA/KNMI GOME NO_2 retrieval (top) and the simulation (bottom, ECHAM5-MOZ abbreviated by MOZECH) for the years 1997 (left), 1999 (middle), and 2000 (right). The anomalies are calculated with respect to the average over these years.

Table 14: Definition of the regions for the NO_2 column analysis.

Region	latitudes			longitudes		
Eastern United States	35° N	–	43° N	90° W	–	71° W
Europe	35° N	–	60° N	10° W	–	30° E
Eastern China	30° N	–	40° N	110° E	–	123° E
India	10° N	–	30° N	70° E	–	90° E
South Africa	28° S	–	23° S	26° E	–	31° E
South America	30° S	–	5° S	70° W	–	50° W
Northern Africa	0° N	–	20° N	20° W	–	40° E
Central Africa	20° S	–	0° N	10° E	–	40° E
Indonesia	10° S	–	10° N	100° E	–	120° E
Northern Australia	30° S	–	10° S	120° E	–	150° E

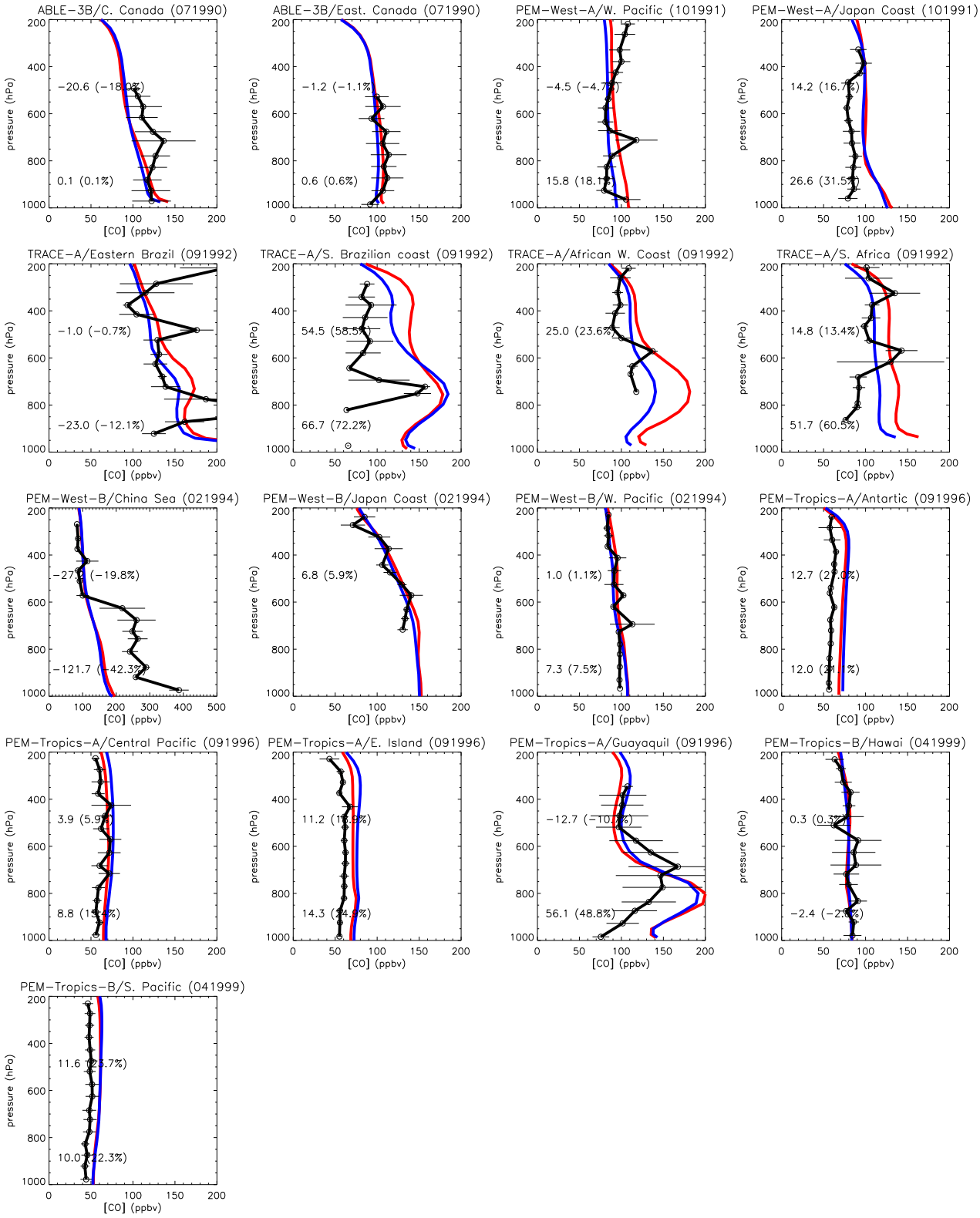

Figure 26: Comparison between observed vertical profiles of CO (open black circles) and simulated monthly mean averaged over the 10-year period 1991-2000 (blue line) and for the specific year of the aircraft campaign (red) over selected areas. The horizontal black bars denote the standard deviation in the observations. The bias of the simulated volume mixing ratios with respect to the measurement is given for the upper (250-750 hPa) and the lower (750 hPa - surface), respectively. Note that different scales are used among the panels.

tropical areas but are underestimated over Canada, near the East Asian coast, and also around Hawaii. In the case of propane, the underestimation in these regions is even stronger.

NO. The comparison between observed and simulated NO vertical profiles (Fig. 29) reveals that NO concentrations tend to be too low in several regions and in particular in the upper troposphere. However, a comparison with the few available NO_2 profiles (not shown here), suggests that the simulated NO_2 concentrations are too high in several places, especially in the tropical oceanic areas and in the polluted boundary layers of the mid and high latitudes of the northern hemisphere.

Peroxyacetylnitrate (PAN). The shape of the observed PAN vertical profile (Fig. 30) is generally well reproduced by the model, e.g. increasing concentrations with altitude and enhanced concentrations in the middle troposphere of regions influenced by biomass burning pollution.

Nitric acid (HNO_3). The measured HNO_3 concentrations (Fig. 31) are often overestimated by the model although the shapes of the observed vertical concentration profiles are usually relatively well reproduced.

Hydrogen peroxide (H_2O_2). As depicted in Fig. 32, the observed vertical profiles of H_2O_2 are relatively well reproduced by the model.

Formaldehyde (HCHO). Formaldehyde (Fig. 33) is directly emitted by biomass burning, anthropogenic, and biogenic sources and it is produced in the atmosphere during oxidation of hydrocarbons, the most important of which is isoprene. The vertical profiles in the tropical region are rather well reproduced by the model.

C.3 Surface ozone

Tables 15 and 16 lists all stations from the EMEP and CASTNET networks which were analyzed in this study.

Table 15: List of EMEP rural stations.

Code	Site name	Data source	Latitude	Longitude	Altitude
Central Europe, altitude < 700 m					
AT02	Illmitz	EMEP	47.77 N	16.77 E	117
AT42	Heidenreichstein	EMEP	48.88 N	15.05 E	570
AT43	Forsthof	EMEP	48.11 N	15.92 E	581
AT45	Dunkelsteinerwald	EMEP	48.37 N	15.55 E	320
AT46	Gänserndorf	EMEP	48.33 N	16.73 E	161
AT47	Stixneusiedl	EMEP	48.05 N	16.68 E	240
BE01	Offagne	EMEP	49.88 N	5.20 E	430
BE32	Eupen	EMEP	50.63 N	6.00 E	295
BE35	Vezin	EMEP	50.50 N	4.99 E	160
CH02	Payerne	EMEP	46.82 N	6.95 E	510
CH03	Tänikon	EMEP	47.48 N	8.90 E	540
CH31	Sion	EMEP	46.22 N	7.33 E	480
DE02	Langenbrügge	EMEP	52.80 N	10.76 E	74
DE04	Deuselbach	EMEP	49.76 N	7.05 E	480
DE07	Neuglobsow	EMEP	53.17 N	13.03 E	62

table continued on next page

Table 15: List of EMEP rural stations — continued.

DE12	Bassum	EMEP	52.85 N	8.70 E	52
DE17	Ansbach	EMEP	49.25 N	10.58 E	481
DE26	Ueckermünde	EMEP	53.75 N	14.07 E	1
DE35	Lückendorf	EMEP	50.83 N	14.77 E	490
NL09	Kollumerwaard	EMEP	53.33 N	6.28 E	1
NL10	Vredepeel	EMEP	51.54 N	5.85 E	28
Northern Europe, altitude < 700 m					
DK31	Ulborg	EMEP	56.28 N	8.43 E	10
DK32	Frederiksborg	EMEP	55.97 N	12.33 E	10
DK41	Lille Valby	EMEP	55.69 N	12.13 E	10
FI09	Utö	EMEP	59.78 N	21.38 E	7
FI17	Virolahti II	EMEP	60.53 N	27.69 E	4
FI22	Oulanka	EMEP	66.32 N	29.40 E	310
NO01	Birkenes	EMEP	58.38 N	8.25 E	190
NO15	Tustervatn	EMEP	65.83 N	13.92 E	439
NO30	Jergul	EMEP	69.45 N	24.60 E	255
NO39	Kårvatn	EMEP	62.78 N	8.88 E	210
NO41	Osen	EMEP	61.25 N	11.78 E	440
NO43	Prestebakke	EMEP	59.00 N	11.53 E	160
NO44	Nordmoen	EMEP	60.27 N	11.10 E	200
NO45	Jeløya	EMEP	59.43 N	10.60 E	5
NO47	Svanvik	EMEP	69.45 N	30.03 E	30
NO48	Voss	EMEP	60.60 N	6.53 E	500
NO49	Valle	EMEP	59.05 N	7.57 E	250
SE02	Rörvik	EMEP	57.42 N	11.93 E	10
SE11	Vavihill	EMEP	56.02 N	13.15 E	175
SE12	Aspvreten	EMEP	58.80 N	17.38 E	20
SE13	Esrange	EMEP	67.88 N	21.07 E	475
SE32	Norra-Kvill	EMEP	57.82 N	15.57 E	261
SE35	Vindeln	EMEP	64.25 N	19.77 E	225
Western Europe, altitude < 700 m					
GB02	Eskdalemuir	EMEP	55.31 N	3.20 W	243
GB06	Lough Navar	EMEP	54.44 N	7.87 W	126
GB13	Yarner Wood	EMEP	50.60 N	3.71 W	119
GB14	High Muffles	EMEP	54.33 N	0.81 W	267
GB15	Strath Vaich Dam	EMEP	57.73 N	4.77 W	270
GB31	Aston Hill	EMEP	52.50 N	3.03 W	370
GB32	Bottesford	EMEP	52.93 N	0.82 W	32
GB33	Bush	EMEP	55.86 N	3.20 W	180
GB34	Glazebury	EMEP	53.46 N	2.47 W	21
GB36	Harwell	EMEP	51.57 N	1.32 W	137
GB37	Ladybower Res.	EMEP	53.40 N	1.75 W	420
GB38	Lullington Heath	EMEP	50.79 N	0.18 E	120
GB39	Sibton	EMEP	52.29 N	1.46 E	46
GB41	Wharleycroft	EMEP	54.60 N	2.47 W	206
Eastern Europe, altitude < 700 m					
CZ01	Svratouch	EMEP	49.73 N	16.03 E	737
CZ03	Kosetice	EMEP	49.58 N	15.08 E	534
LT15	Preila	EMEP	55.35 N	21.07 E	5

table continued on next page

Table 15: List of EMEP rural stations — continued.

SI33	Kovk	EMEP	46.13 N	15.11 E	600
Mediterranean Europe, altitude < 700 m					
ES03	Roquetas	EMEP	40.82 N	0.49 E	44
ES04	Logroño	EMEP	42.46 N	2.50 W	445
ES05	Noya	EMEP	42.73 N	8.92 W	683
IT04	Ispra	EMEP	45.80 N	8.63 E	209
PT04	Monte Velho	EMEP	38.08 N	8.80 W	43
Mountain stations, altitude ≥ 700 m					
AT04	St. Koloman	EMEP	47.65 N	13.20 E	851
AT32	Sulzberg	EMEP	47.53 N	9.93 E	1020
AT33	Stolzalpe bei Murau	EMEP	47.13 N	14.20 E	1302
AT34	Sonnblick	EMEP	47.05 N	12.96 E	3106
AT37	Zillertaler Alpen	EMEP	47.14 N	11.87 E	1970
AT38	Gerlitzen	EMEP	46.69 N	13.91 E	1895
AT41	Haunsberg	EMEP	47.97 N	13.02 E	730
DE03	Schauinsland	EMEP	47.91 N	7.91 E	1205
DE05	Brotjacklriegel	EMEP	48.82 N	13.22 E	1016
DE08	Schmücke	EMEP	50.65 N	10.77 E	937
ES01	San Pablo de los Montes	EMEP	39.55 N	4.35 W	917
GB35	Great Dun Fell	EMEP	54.68 N	2.43 W	847
SI31	Zarodnje	EMEP	46.43 N	15.00 E	770
SI32	Krvavec	EMEP	46.30 N	14.54 E	1740
SK04	Stará Lesná	EMEP	49.15 N	20.28 E	808

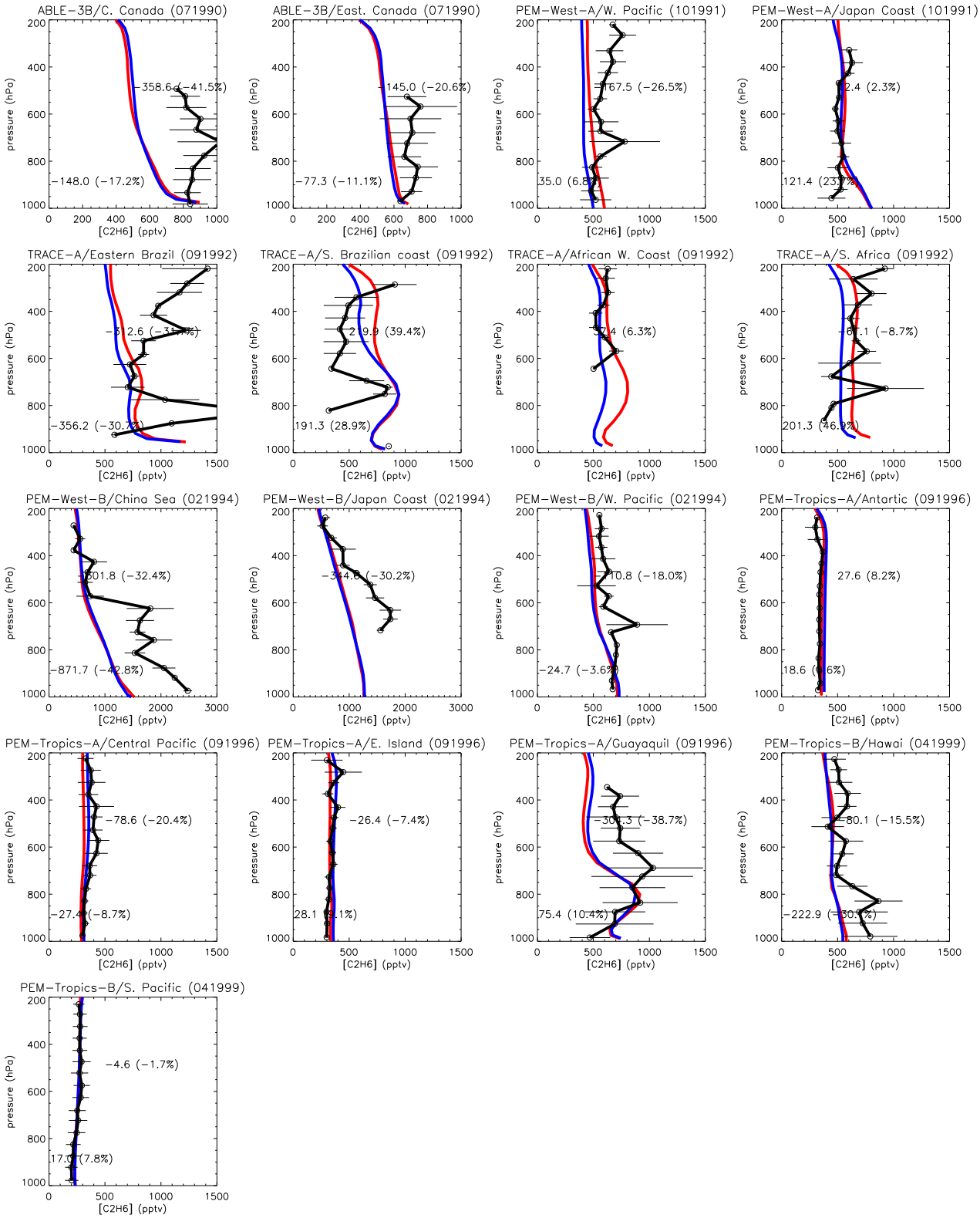

Figure 27: As figure 26 but for ethane (C_2H_6). Note the different scales.

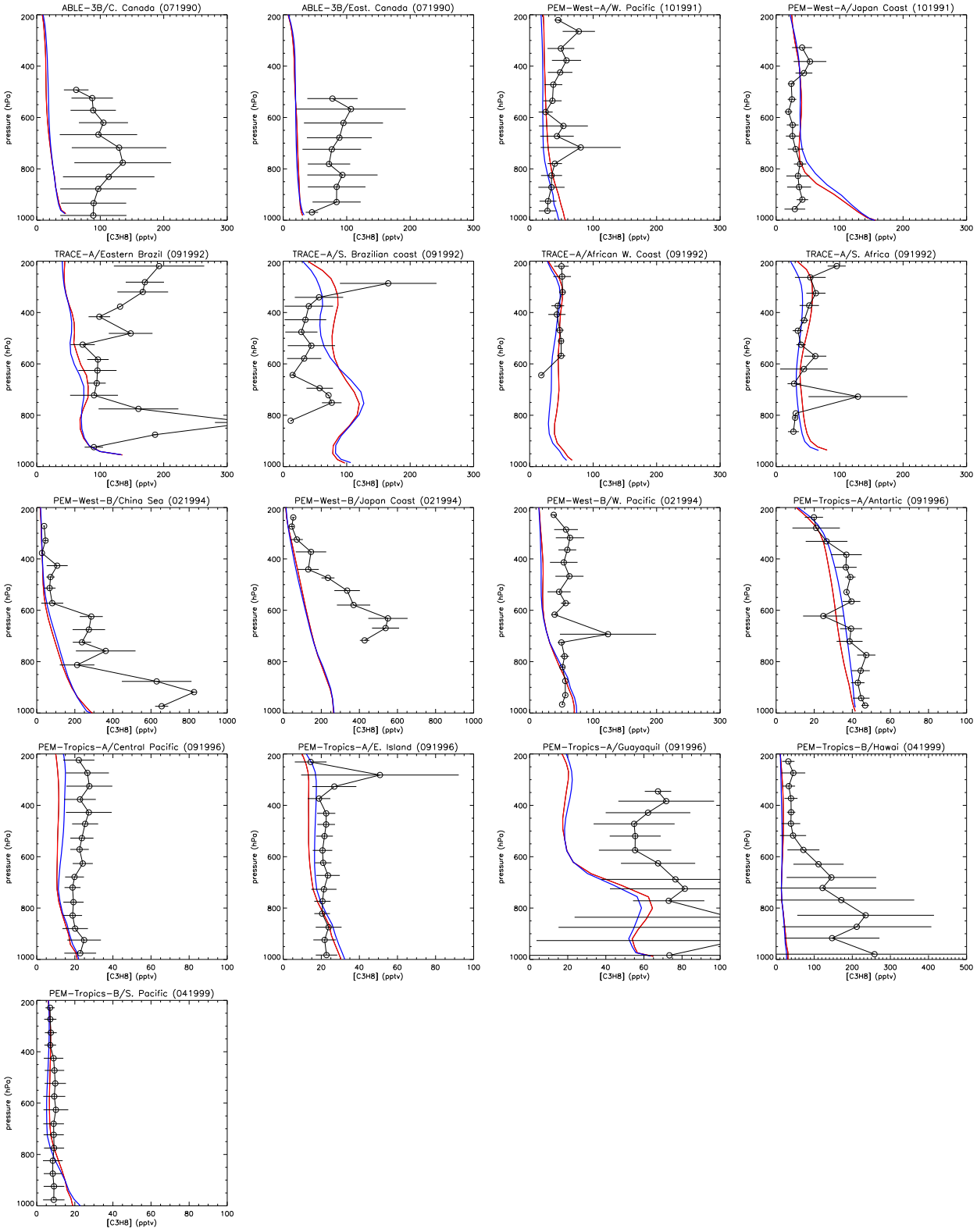

Figure 28: As figure 26 but for propane (C_3H_8). Note the different scales.

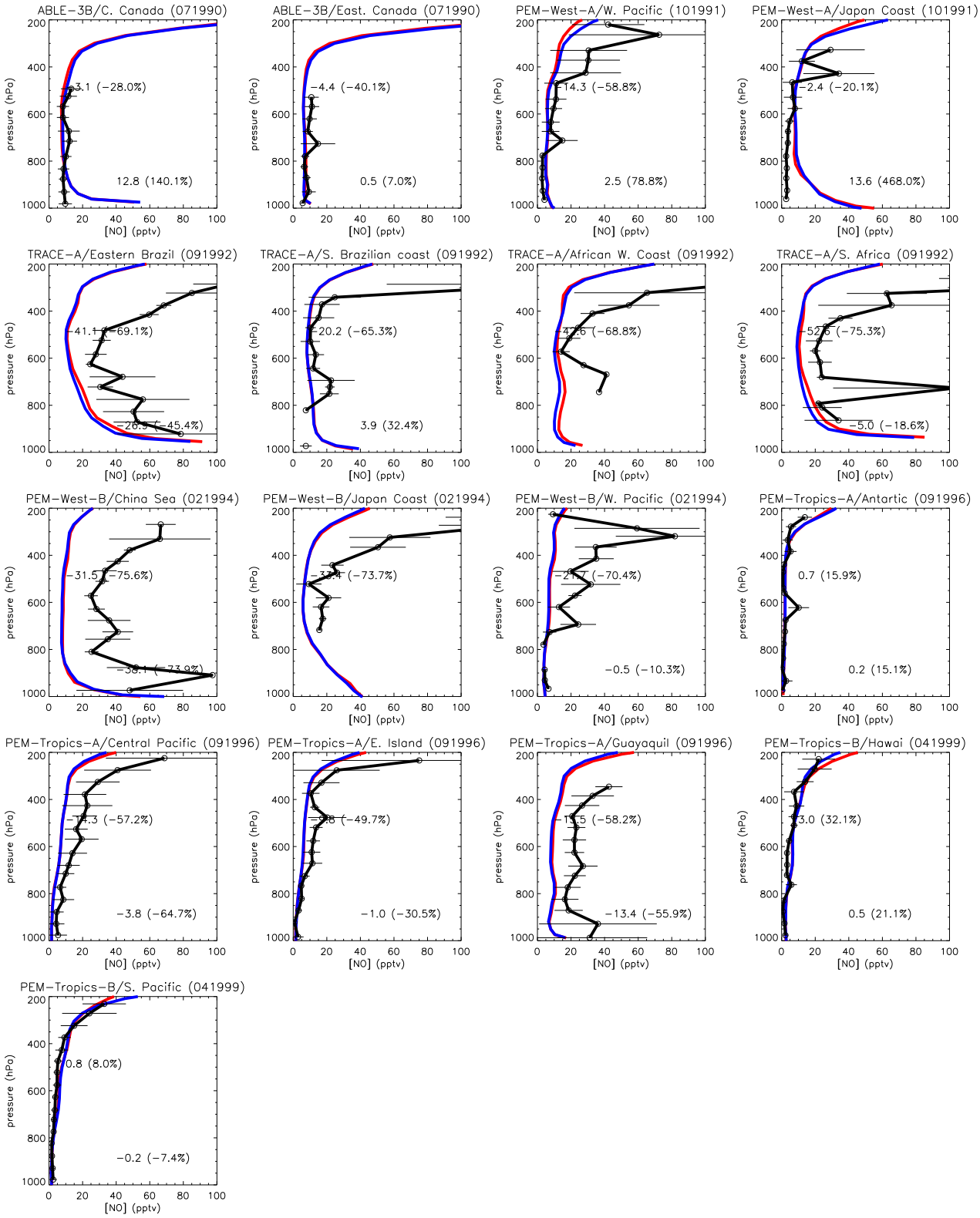

Figure 29: As figure 26 but for nitric oxide (nitrogen monoxide, NO).

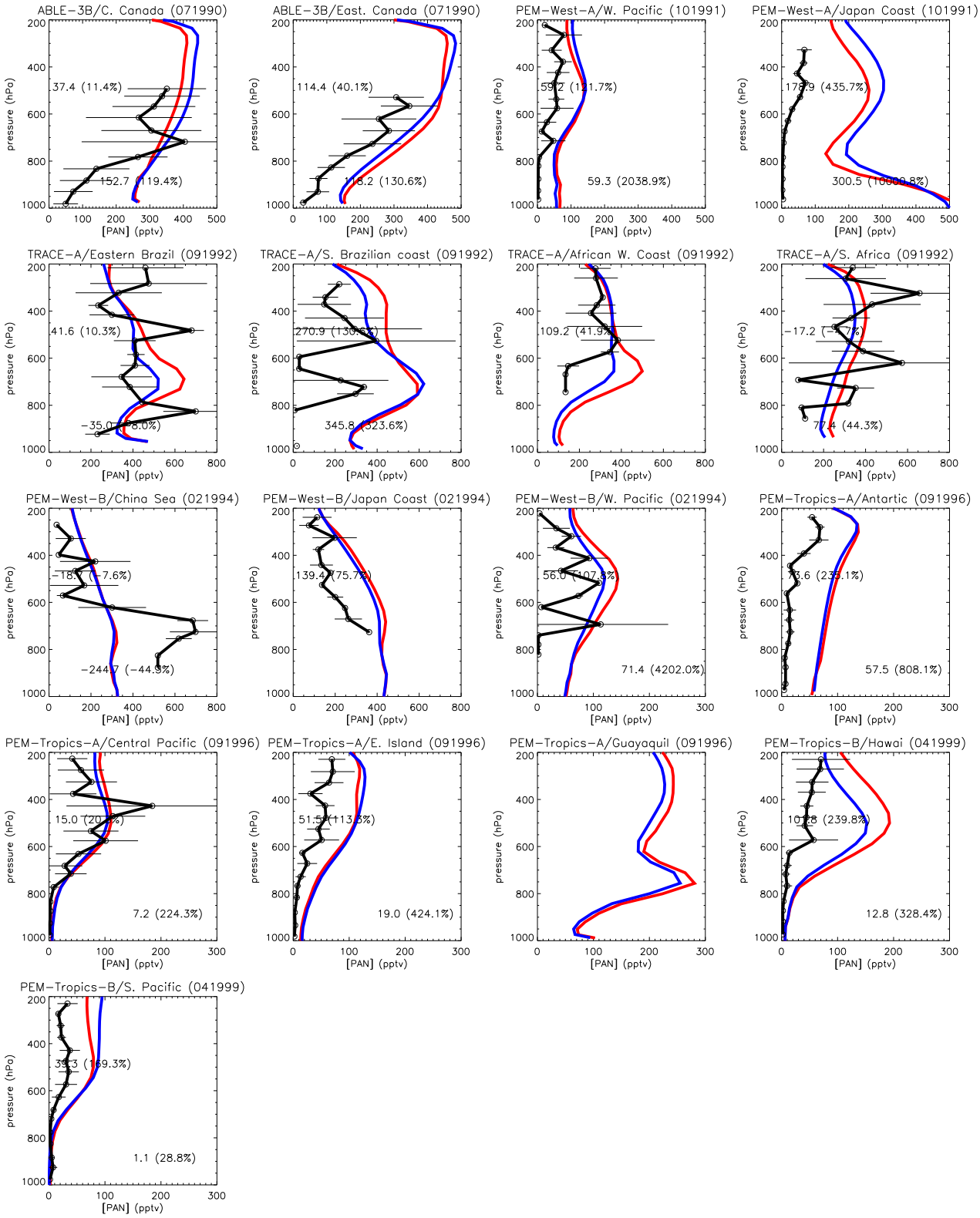

Figure 30: As figure 26 but for peroxyacetyl nitrate (PAN). Note the different scales.

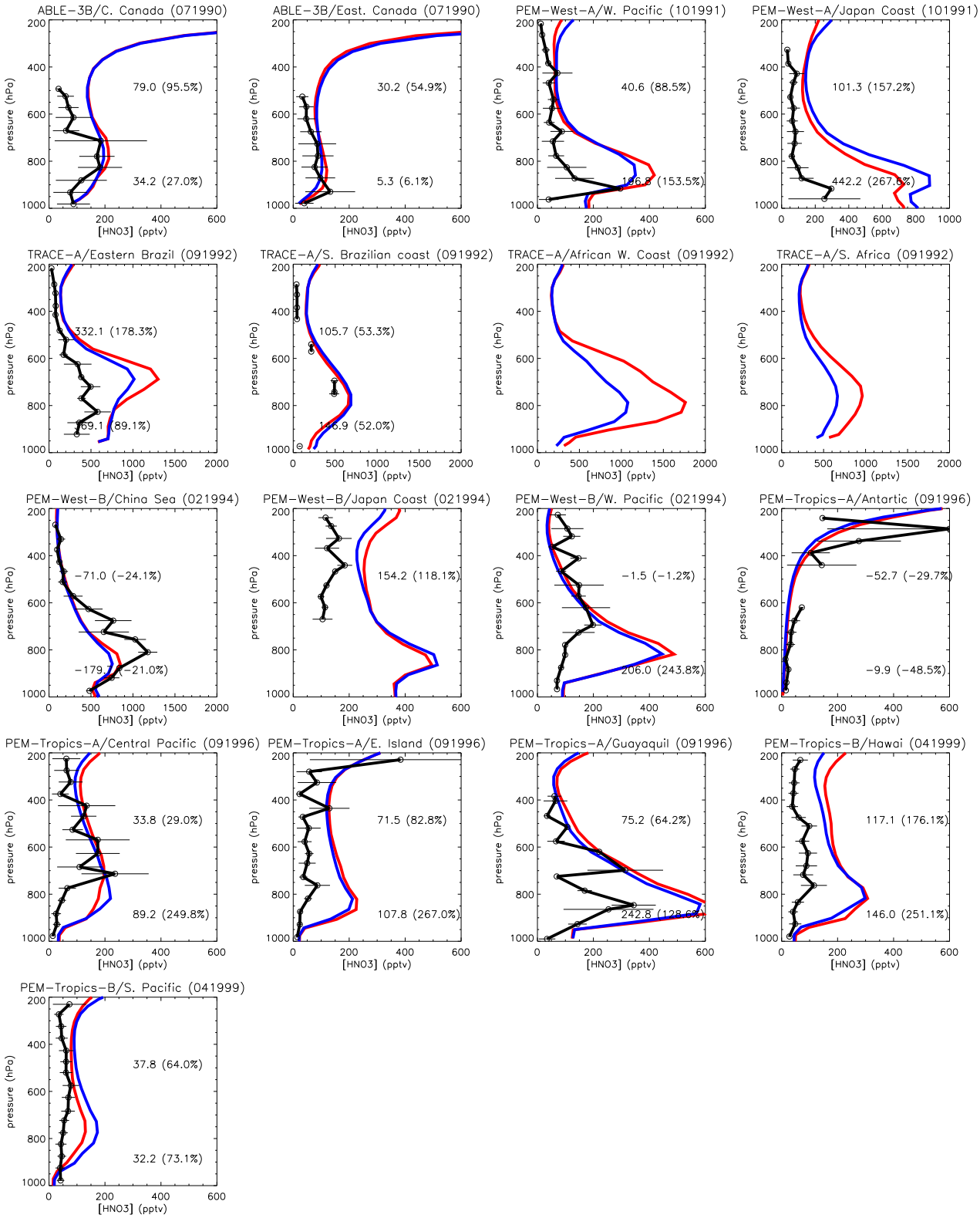

Figure 31: As figure 26 but for nitric acid (HNO_3). Note the different scales.

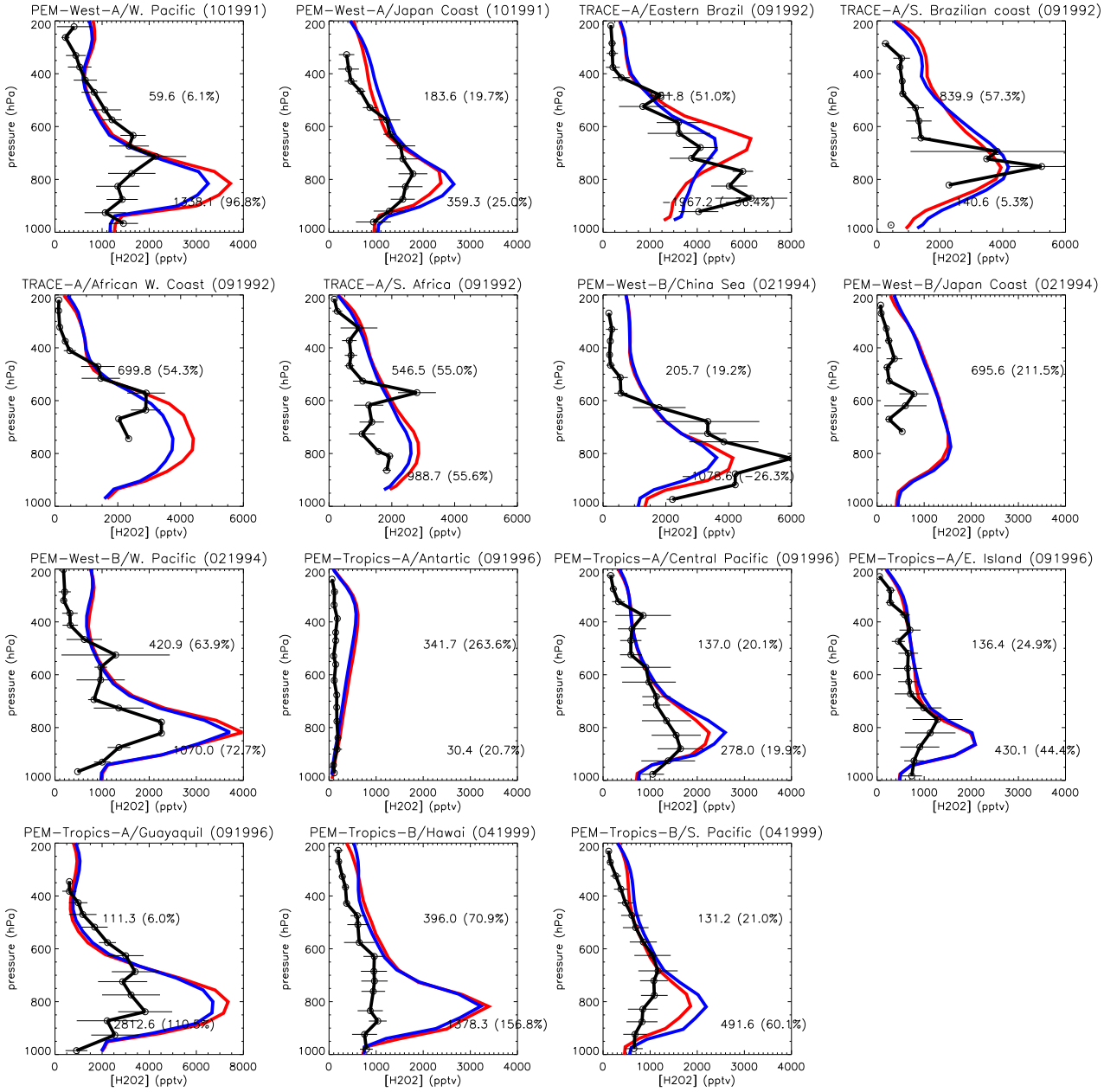

Figure 32: As figure 26 but for hydrogen peroxide (H_2O_2). Note the different scales.

Table 16: List of rural CASTNET stations.

Code	Site name	Data source	Latitude	Longitude	Altitude
ALH157	Alhambra	CASTNET	38.87 N	89.62 W	164
ANA115	Ann Arbor	CASTNET	42.42 N	83.90 W	267
ARE128	Arendtsville	CASTNET	39.92 N	77.31 W	269
ASH135	Ashland	CASTNET	46.60 N	68.41 W	235
BEL116	Beltsville	CASTNET	39.03 N	76.82 W	46
BVL130	Bondville	CASTNET	40.05 N	88.37 W	212
CAD150	Caddo Valley	CASTNET	34.18 N	93.10 W	71
CDR119	Cedar Creek	CASTNET	38.88 N	80.85 W	234
CAD150	Caddo Valley	CASTNET	34.18 N	93.10 W	71
CND125	Candor	CASTNET	35.26 N	79.84 W	198
COW137	Coweeta	CASTNET	35.06 N	83.43 W	686
CTH110	Connecticut Hill	CASTNET	42.40 N	76.65 W	501
CVL151	Coffeeville	CASTNET	34.00 N	89.80 W	134
DCP114	Deer Creek	CASTNET	39.64 N	83.26 W	267
ESP127	Edgar Evins	CASTNET	36.04 N	85.73 W	302
GAS153	Georgia Station	CASTNET	33.18 N	84.41 W	270
KEF112	Kane Exp. Forest	CASTNET	41.60 N	78.77 W	622
LRL117	Laurel Hill	CASTNET	39.99 N	79.25 W	615
LYK123	Lykens	CASTNET	40.92 N	83.00 W	303
MCK131	Mackville	CASTNET	37.70 N	85.05 W	353
MKG113	M.K. Goddard	CASTNET	41.43 N	80.15 W	384
OXF122	Oxford	CASTNET	39.53 N	84.73 W	284
PAR107	Parsons	CASTNET	39.09 N	79.66 W	510
PED108	Prince Edward	CASTNET	37.17 N	78.31 W	150
PRK134	Perkinstown	CASTNET	45.21 N	90.60 W	472
PSU106	Penn State	CASTNET	40.72 N	77.93 W	378
SAL133	Salamonie Reservoir	CASTNET	40.82 N	85.66 W	250
SND152	Sand Mountain	CASTNET	34.29 N	85.97 W	352
SPD111	Speedwell	CASTNET	36.47 N	83.83 W	361
SUM156	Sumatra	CASTNET	30.11 N	84.99 W	14
UVL124	Unionville	CASTNET	43.61 N	83.36 W	201
VIN140	Vincennes	CASTNET	38.74 N	87.49 W	134
WSP144	Wash. Crossing	CASTNET	40.31 N	74.87 W	61
WST109	Woodstock	CASTNET	43.94 N	71.70 W	258

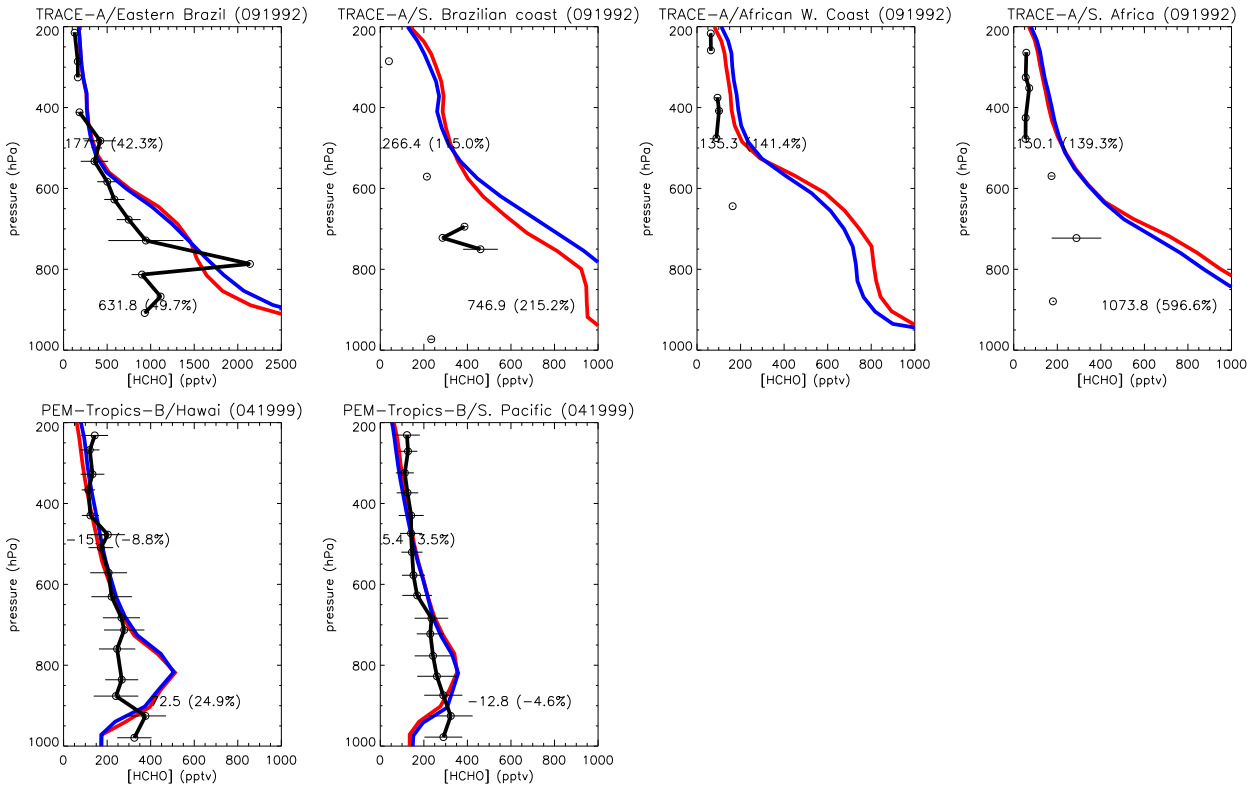

Figure 33: As figure 26 but for formaldehyde (HCHO). Note the different scales.

References

Aghedo,A.M., *The impact of african air pollution: A global chemistry climate model study*, PhD thesis, Universität Hamburg, 2007.

Aghedo, A.M., M.G. Schultz, and S. Rast, The influence of african air pollution on regional and global tropospheric ozone, *Atmos. Chem. Phys.*, 7:1193-1212, 2007.

Akima, H., A New Method of Interpolation and Smooth Curve Fitting Based on Local Procedures, *Journal of the Association for Computing Machinery*, 17(4):589-602, 1970.

Andreae, M.O., and P. Merlet, Emission of trace gases and aerosols from biomass burning *Global Biogeochemical Cycles* 15(4):955-966, 2001.

Auvray, M., I. Bey, E. Llull, M.G. Schultz, and S. Rast, A model investigation of tropospheric ozone chemical tendencies in long-range transported pollution plumes, *J. Geophysical Research*, 112(D5):doi:10.1029/2006JD007137, 2007.

Bey, I., D.J. Jacob, R.M. Yantosca, J.A. Logan, B.D. Field, A.M. Fiore, Q. Li, H.Y. Liu, L.J. Mickley, and M.G. Schultz, Glocal modeling of tropospheric chemistry with assimilated meteorology: Model description and evaluation, *J. Geophysical Research*, 106(D19):23,073-23,095, 2001.

Boucher, O., and M. Pham, History of sulfate aerosol radiative forcings, *Geophys. Res. Lett.*, 29(9):doi:10.1019/2001GL014048, 2002.

Boersma, K.F., H.J. Eskes, and E.J. Brinksma, Error analysis for tropospheric NO_2 retrieval from space, *J. Geophysical Research*, 109(D04311):doi:10.1029/2003JD003962, 2004.

Brasseur, G.P., D.A. Hauglustaine, S. Walters, P.J. Rasch, J.-F. Müller, C. Granier, and X.X. Tie, MOZART, a global chemical transport model for ozone and related chemical tracers 1. model description, *J. Geophysical Research*, 103(D21):28,265-28,289, 1998.

Browell, E.V., M.A. Fenn, C.F. Butler, W.B. Grant, J.T. Merrill, R.E. Newell, J.D. Bradshaw, S.T. Sandholm, B.E. Anderson, A.R. Bandy, A.S. Bachmeier, D.R. Blake, D.D. Davis, G.L. Gregory, B.G. Heikes, Y. Kondo, S.C. Liu, F.S. Rowland, G.W. Sachse, H.B. Singh, R.W. Talbot, and D.C. Thornton, Large-scale air mass characteristics observed over Western Pacific during summertime *J. Geophysical Research*, 101(D1):1691-1712, 1996.

Browell, E.V., M.A. Fenn, C.F. Butler, W.B. Grant, M.B. Clayton, J. Fishman, A.S. Bachmeier, B.E. Anderson, G.L. Gregory, H.E. Fuelberg, J.D. Bradshaw, S.T. Sandholm, D.R. Blake, B.G. Heikes, G.W. Sachse, H.B. Singh, and R.W. Thalbot, Ozone and aerosol distributions and air mass characteristics over the South Atlantic Basin during the burning season *J. Geophysical Research*, 101(D19):24,043-24,068, 1996.

Carslaw, D.C, On the changing seasonal cycles and trends of ozone at Mace Head, Ireland, *Atmos. Chem. Phys.*, 5:3441-3450, 2005.

Chen, Y., L. Craig, and D. Krewski, Air quality risk assessment and management, *J. Toxicolog. Env. Health, Part A*, 71:24-39, 2008.

Cleveland, R.B., W.S. Cleveland, J.E. McRae, and I. Terpenning, STL: A Seasonal-Trend Decomposition Procedure Based on Loess, *J. Official Statistics*, 6(1):3-73, 1990.

Dalsoren, S.B., T. Pulles, D. Panasiuk, M. Schultz, S. Rast, S. Schröder, T. van Noije, and S.Szopa, Analysis of past and present policy response to trends in European air pollution In M. Schultz and S. Rast *RETRO, Work Package 5, Deliverable D5-5*, European Project EVK2-CT-2002-00170 (RETRO), Max Planck Institute for Meteorology, Hamburg, 2007.

Dentener, F., D. Stevenson, K. Ellingsen, T. van Noije, M. Schultz, M. Amann, C. Atherton, N. Bell, D. Bergmann, I. Bey, L. Bouwman, T. Butler, J. Cofala, B.Collins, J. Drevet, R. Doherty, B. Eickhout, H. Eskes, A. Fiore, L. Horowitz, I.S.A. Isaksen, B. Josse, M. Lawrence, M. Krol, J.F. Lamarque, V. Montanaro, J.F. Müller, V.H. Peuch, G. Pitari, J. Pyle, S. Rast, J. Rodriguez, M. Sanderson, N.H. Savage, D. Shindell, S. Strahan, S. Szopa, K. Sudo, R. van Dingenen, O. Wild, and G. Zeng, The global atmospheric environment for the next generation, *Environ. Sci. Technol.*, 40:3586-3594, 2006.

Dentener, F., J. Drevet, J.F. Lamarque, I. Bey, B. Eickhout, A.M. Fiore, D. Hauglustaine, L.W. Horowitz, M. Krol, U.C. Kulshrestha, M. Lawrence, C. Galy-Lacaux, S. Rast, D. Shindell, D. Stevenson, T. van Noije, C. Atherton, N. Bell, D. Bergman, T. Butler, J. Cofala, B. Collins, R. Doherty, K. Ellingsen, J. Galloway, M. Gauss, V. Montanaro, J.F. Müller, G. Pitari, J. Rodriguez, M. Sanderson, F. Solomon, S. Strahan, M. Schultz, K. Sudo, S. Szopa, and O. Wild, Nitrogen and sulfur deposition on regional and global scales: A multimodel evaluation, *Global Biogeochemical Cycles*, 20(GB4003):doi:10.1029/2005GB002672, 2006.

Derwent, R.G., P.G. Simmonds, A.J. Manning, T.G. Spain, Trends over a 20-year period from 1987 to 2007 in surface ozone at the atmospheric research station, Mace Head, Ireland, *Atmospheric Environment* 41:9091-9098, 2007.

Dlugokencky, E.J., K.A. Masarie, P.M. Land, and P.P. Tans, Continuing decline in the growth raste of the atmospheric methane burden, *Nature*, 393(4), 447-450, 1998.

Duncan B.N., I. Bey, M. Chin, L.J. Mickley, T.D. Fairlie, R.V. Martin, H. Matsueda, Indonesian wildfires of 1997: Impact on tropospheric chemistry, *J. Geophys. Res.*, 108 (D15), 4458, doi:10.1029/2002JD003195, 2003.

Duncan B.N., J.A. Logan, I. Bey, I.A. Megretskaia, R.M. Yantosca, P.C. Novelli, N.B. Jones, C.P. Rinsland, Global budget of CO, 1988-1997: Source estimates and validation with a global model, *J. Geophys. Res.*, 112(D22301), doi:10.1029/2007JD008459, 2007.

Emmons, L.K., D.A. Hauglustaine, J.-F. Müller, M.A. Carroll, G.P. Brasseur, D. Brunner, J. Staehelin, V. Touret, and A. Marenco, Data composites of airborne observations of tropospheric ozone and its precursors, *J. Geophysical Research*, 105(D16):20,497-20,538, 2000.

Emmons, L.K., M.N. Deeter, J.C. Gille, D.P. Edwards, J.-L. Attié, J. Warner, D. Ziskin, G. Francis, B. Khattatov, V. Yudin, J.-F. Lamarque, S.-P. Ho, D. Mao, J.S. Chen, J. Drummond, P. Novelli, G. Sachse, M.T. Coffey, J.W. Hannigan, C. Gerbig, S. Kawakami, Y. Kondo, N. Takegawa, H. Schlager, J. Baehr, and H. Ziereis, Validation of measurements of pollution in the troposphere (MOPITT) CO retrievals with aircraft in situ profiles, *J. Geophysical Research*, 109(D03309), doi:10.1029/2003JD004101, 2004.

Endresen, Ø., E. Sørgård, J.K. Sundet, S.B. Dalsøren, I.S.A. Isaksen, T.F. Berglen, and G. Gravir, Emission from international sea transportation and environmental impact, *J. Geophysical Research*, 108(D17):4560, doi:10.1029/2002JD002898, 2003.

Eyring, V., N.R.P. Harris, M. Rex, R.G. Shepherd, D.W. Fahey, G.T. Amanatidis, J. Austin, M.P. Chipperfield, M. Dameris, P.M. De F. Forster, A.Gettelman, H.F. Graf, T. Nagashima, P.A. Newman, S. Paswon, M.J. Prather, J.A. Pyle, R.J. Salawitch, B.D. Santer, and D.W. Waugh, A strategy for process-oriented validation of coupled chemistry-climate models, *Bull. American Meteor. Soc.*, 1117-1133, 2005.

Fenn, M.A., E.V. Browell, C.F. Butler, W.B. Grant, S.A. Kooi, M.B. Clayton, G.L. Gregory, R.E. Newell, Y. Zhu, J.E. Dibb, H.E.Fuelberg, B.E. Anderson, A.R. Bandy, D.R. Blake, J.D. Bradshaw, B.G. Heikes, G.W. Sachse, S.T.Sandholm, H.B.Singh, R.W.Talbot, and

D.C. Thornton, Ozone and aerosol distributions and air mass characteristics over the South Pacific during the burning season *J. Geophysical Research*, 104(D13):16,197-16,212, 1999.

Feichter, J., E. Kjellström, H. Rodhe, F. Dentener, J. Lelieveld, and G.-J. Roelofs, Simulation of the tropopsheric sulfur cycle in a global climate model, *Atmos. Environ.* 30(10/11), 1693-1707, 1996.

Fiore, A.M., D.J. Jacob, B.D. Field, D.G. Streets, S.D. Fernandez, and C. Jang, Linking ozone pollution and climate change: The case for controlling methane, *Geophys. Res. Lett.*, 29(19):1919, doi:10.1029/2002GL015601, 2002.

Fiore, A.M., F.J. Dentener, O. Wild, C. Cuvelier, M.G. Schultz, P. Hess, C. Textor, M. Schulz, R. Doherty, L.W. Horowitz, I.A. MacKenzie, M.G. Sanderson, D.T. Shindell, D.S. Stevenson, S. Szopa , R. Van Dingenen, G. Zeng, C. Atherton, D. Bergmann, I. Bey, G. Carmichael, B.N. Duncan, G. Faluvegi, G. Folberth, M. Gauss, S. Gong, D. Hauglustaine, T. Holloway, I.S.A. Isaksen, D.J. Jacob, J.E. Jonson, J.W. Kaminski, T.J. Keating, A. Lupu, E. Marmer, V. Montanaro, R. Park, G. Pitari, K.J. Pringle, J.A. Pyle, S. Schroeder, M.G. Vivanco, P. Wind, G. Wojcik, S. Wu, A. Zuber, Multi-model estimates of intercontinental source-receptor relationships for ozone pollution, /newblock*J. Geophys. Res.*, 114(D04301), doi:10.1029/2008JD010816, 2009.

Folberth, G., G. Pfister, D. Baumgartner, E. Putz, L. Weissflog, and N.P. Elansky, The annual course of TCA formation in the lower troposphere: a modelling study, *Environmental Pollution*, 124(3):389-405, 2003.

Folberth, G.A., D.A. Hauglustaine, J. Lathière, and F. Brocheton, Interactive chemistry in the Laboratoire de Mètèorologie Dynamique general circulation model: model description and impact analysis of biogenic hydrocarbons on tropospheric chemistry, newblock *Atmos. Chem. Phys.*, 6:2273-2319, 2006.

Folkins, I., R. Chatfield, D. Baumgardner, M. Proffitt, Biomass burning and deep convection in southeastern Asia: Results from ASHOE/MAESA, *J. Geophys. Res.*, 102(11D): 13291-13299, 1997.

Freitas, S.R., K.M. Longo, M.A.F. Silva Dias, P.L. Silva Dias, R. Chatfield, E. Prins, P. Artaxo, G.A. Grell, and F.S. Recuero, Monitoring the Transport of Biomass Burning Emissions in South America, *Environ. Fluid Mechanics*, 5:135-167, 2005.

Fuhrer, J., L. Skärby, and M.R. Ashmore, Critical levels for ozone effects on vegetation in Europe. *Environmental Pollution*, 97(1-2):91-106, 1997.

Ganzeveld, L., and J. Lelieveld, Dry deposition parameterization in a chemistry general circulation model and its influence on the distribution of reactive trace gases, *J. Geophysical Research*, 100(D10):20,999-21,012, 1995.

Gauss, M., G. Myhre, I.S.A. Isaksen, V. Grewe, G. Pitari, O. Wild, W.J. Collins, F.J. Dentener, K. Ellingsen, L.K. Gohar, D.A. Hauglustaine, D. Iachetti, J.-F. Lamarque, E. Mancini, L.J. Mickley, M.J. Prather, J.A. Pyle, M.G. Sanderson, K.P.Shine, D.S. Stevenson, K. Sudo, S. Szopa, G. Zeng, Radiative forcing since preindustrial times due to ozone change in the troposphere and the lower stratosphere, *Atmos. Chem. Phys.*, 6: 575-599, 2006.

GLOBALVIEW-CH4, Cooperative Atmospheric Data Integration Project - Methane. CD-ROM, NOAA CMDL, Boulder, Colorado [Also available on Internet via anonymous FTP to ftp.cmdl.noaa.gov, Path: ccg/ch4/GLOBALVIEW], 2005.

Granier, C., J.F. Müller, G. Pétron, and G. Brasseur, A three-dimensional study of the global CO budget *Chemosphere: Global Change Science* 1, 255-261, 1999.

Grewe, V., D. Brunner, M. Dameris, J.L. Grenfell, R. Hein, D. Shindell, and J. Staehelin, Origin and variability of upper tropospheric nitrogen oxides and ozone at northern mid-latitudes, *Atmospheric Environment*, 35:3421-3433, 2001.

Grewe, V., M. Dameris, Ch. Fichter, and R. Sausen, Impact of aircraft NO_x emissions. Part 1: Interactively coupled climate-chemistry simulations and sensitivities to climate-chemistry feedback, lightning and model resolution, *Meteorolog. Zeitschrift*, 11(3):177-186, 2002.

Grewe, V., Impact of climate variability on troposheric ozone, *Science of the Total Environment*, 374:167-181, 2007.

Guenther, A., T. Karl, P. Harley, C. Wiedinmyer, P.I. Palmer, and C. Geron, Estimates of global terrestrial isoprene emissions using MEGAN (model of emissions of gases and aerosols from nature), *Atmos. Chem. Phys.*, 6:3181-3210, 2006.

Guldberg, A., E. Kaas, M. Déqué, S. Yang, and S. Vester Thorsen, Reduction of systematic errors by empirical model correction: impact on seasonal prediction skill, *Tellus*, 57A:575-588, 2005.

Hagemann, S., K. Arpe, and E. Roeckner. Evaluation of the hydrological cycle in the ECHAM5 model, *J. of Climate*, submitted, 2005.

Hauglustaine, D.A., F. Hourdin, L. Jourdain, M.-A. Filiberti, S. Walters, J.-F. Lamarque, and E.A. Holland, Interactive chemistry in the Laboratoire de Météorologie Dynamique general circulation model: Description and background tropospheric chemistry evaluation, *J. Geophysical Research*, 109(D04314):doi:10.1029/2003JK003957, 2004.

Heimann, M., The global atmospheric tracer model TM2, *Tech. Rep.* 10, Deutsches Klimarechenzentrum, Hamburg, Germany, 1995.

Horowitz, L.W., S. Walters, D.L. Mauzerall, L.K. Emmons, P.J. Rasch, C. Granier, X. Tie, J.-F. Lamarque, M.G. Schultz, G.S. Tyndall, J.J. Orlando, and G.P. Brasseur, A global simulation of tropospheric ozone and related tracers: Description and evaluation of mozart, version2, *J. Geophysical Research*, 108(D24):doi:10.1029/2002JD002853, 2003.

IPCC2001: Ehhalt, D., M. Prather, F. Dentener, E. Dlugokencky, E. Holland, I. Isaksen, J. Katima, V. Kirchhoff, P. Matson, P. Midgley, M. Wang, Atmospheric chemistry and greenhouse gases, in *Climate Change 2001: The Scientific Basis, Contribution of Working Group I to the Third Assessment Report of the Intergovernmental Panel on Climate Change*, edited by J.T. Houghto et al., 239-288, Cambridge Univ. Press, New York, 2001.

IPCC2007: Solomon, S., D. Qin, M. Manning, Z. Chen, M. Marquis, K.B. Averyt, M. Tignor, and H.L. Miller (eds.), Climate change 2007: The physical science basis. Contribution of working group I to the fourth assessment report of the Intergovernmental Panel on Climate Change, *Cambridge University Press*, Cambridge, United Kingdom and New York, NY, USA, 2007.

Jacob, D.J., B.D. Field, E.M. Jin, I. Bey, Q. Li, J.A. Logan, R.M. Yantosca, and H.B. Singh, Atmospheric budget of acetone, *J. Geophys. Res.*, 107 (D10), 4100, doi:10.1029/2001JD000694, 2002.

Jacobson, M.Z., D.G. Streets, Influence of future anthropogenic emissions on climate, natural emissions, and air quality, *J. Geophys. Res.*, 114(D08118):doi:10.1029/2008JD011476, 2009.

Jaeglé, L., D.J. Jacob, W.H. Brune, and P.O. Wennberg. Chemistry of HO_x radicals in the upper troposphere, *Atmos. Environment*, 35:469-489, 2001.

Jaffe, D., and J. Ray, Increase in surface ozone at rural sites in the western US, *Atmos. Environment*, 41:5452-5463, 2007.

Jeuken, A.B.M., P.C. Siegmund, L.C. Heijboer, J. Feichter, and L. Bengtsson, On the potential of assimilating meteorological analyses in a global climate model for the purpose of model validation, *J. Geophysical Research*, 101(D12):16939-16950, 1996.

Jöckel, P., H. Tost, A. Pozzer, C. Brühl, J. Buchholz, L. Ganzeveld, P. Hoor, A. Kerkweg, M.G. Lawrence, R. Sander, B. Steil, G. Stiller, M. Tanarhte, D. Taraborelli, J. van Aardenne, and J. Lelieveld, The atmospheric chemistry general circulation model ECHAM5/MESSy1: consistent simulation of ozone from the surface to the mesosphere *Atmos. Chem. Phys.*, 6, 5067-5104, 2006.

Jungclaus, J.H., M. Botzet, H. Haak, N. Keenlyside, J.-J. Luo, M. Latif, J. Marotzke, U. Mikolajewicz, and E. Roeckner, Ocean circulation and tropical variability in the coupled model ECHAM5/MPI-OM, *J. Climate*, 19(16):3952-3972, 2006.

Kloster, S., K.D. Six, J. Feichter, E. Maier-Reimer, E. Roeckner, P. Wetzel, P. Stier, and M. Esch, Response of dimethylsulfide (DMS) in the ocean and atmosphere to global warming, *J. Geophysical Research*, 112(G03005):doi:10.1029/2006JG000224, 2007.

Koch, D., D. Jacob, I. Tegen, D. Rind, and M. Chin, Tropospheric sulfur simulation and sulfate direct radiative forcing in the Goddard Institute for Space Studies general circulation model, *J. Geophysical Research*, 104(D19):23,799-23,822, 1999.

Koumoutsaris, S., I. Bey, S. Generoso, and V. Thouret, Influence of El Niño-Southern Oscillation on the interannual variability of tropospheric ozone in the northern midlatitudes, *J.Geophysical Research*, 113(D19301), doi:10.1029/2007JD009753, 2008.

Lamarque, J.-F.), T.C. Bond, V. Eyring, C. Granier, A. Heil, Z. Klimont, D. Lee, C. Liousse, A. Mieville, B. Owen, M.G. Schultz, D. Shindell, S.J. Smith, E. Stehfest, J. Van Aardenne, O.R. Cooper, M. Kainuma, N. Mahowald, J.R. McConnell, V. Naik, K. Riahi, and D.P. van Vuuren, Historical (1850-2000) gridded anthropogenic and biomass burning emissions of reactive gases and aerosols: methodology and application, *Atmos. Chem. Phys.*, 10(15), 7017-7039, 2010.

Lanser, D., and J.G. Verwer, Analsysis of operator splitting for advection-diffusion-reaction problems from air pollution modelling, *J. Comput. Appl. Mathematics*, 111:201-216, 1999.

Lathière, J., *personal communication*, 2002.

Lathière, J., D.A. Hauglustaine, A.D. Friend, N. De Noblet-Ducoudré, N. Viovy, and G.A. Folberth, Impact of climate variability and land use changes on global biogenic volatile organic compound emissions *Atmos. Chem. Phys.*, 6, 2129-2146, 2006.

Lavoué, D., *personal communication*, 2004.

Liao, H., P.J. Adams, S.H. Chung, J.H. Seinfeld, L.J. Mickley, and D.J. Jacob, Interactions between tropospheric chemistry and aerosols in a unified general circulation model, *J. Geophysical Research*, 108(D1), doi:10.1029/2001JD001260, 2003.

Lin, S.-J., and R.B. Rood, Multidimensional flux-form semi-lagrangian transport schemes, *Monthly Weather Review*, 124:2046-2070, 1996.

Machenhauer, B., and I. Kirchner, Diagnosis of systematic initial tendency errors in the ECHAM AGCM using slow normal mode data-assimilation of ECMWF reanalysis data, accessible through: *http://web.dmi.dk/pub/POTENTIALS/Final/Appendix-1.PDF* (last accessed October 19th, 2008).

Madronich, S., and S. Flocke, The role of solar radiation in atmospheric chemistry. In P. Boule, editor, *Handbook of Environmental Chemistry*, Springer-Verlag, 1998.

Marenco, A., V. Thouret, Ph. Nédélec, H. Smit, M. Helten, D. Kley, F. Karcher, P. Simon, K. Law, J. Pyle, G. Poschmann, R. Von Wrede, Ch. Hume, and T. Cook, Measurement of ozone and water vaport by Airbus in-service aircraft: The MOZAIC airborne program, An overview, *J. Geophysical Research*, 103(D19):25,631-25,542, 1998.

Martin, R.V., D.J. Jacob, K. Chance, Th.P. Kurosu, P.I. Palmer, and M.J. Evans, Global inventory of nitrogen oxide emissions constrained by space-based observations of NO_2 columns. *J. Geophysical Research*, 108(D17):doi:10.1029/2003JD003453, 2003.

Mickley, L.J., P.P. Murti, D.J. Jacob, J.A. Logan, D.M. Koch, and D. Rind, Radiative forcing from tropospheric ozone calculated with a unified chemistry-climate model, *J. Geophysical Research*, 104(D23):30,153-30,172, 1999.

Müller, J.-F., Geographical distribution and seasonal variation of surface emissions and deposition velocities of atmospheric trace gases, *J. Geophys. Res.*, 97(D4): 3787-2804, 1992.

Nordeng., T.-E., Extended versions of the convection parametrization scheme at ECMWF and their impact upon the mean climate and transient activity of the model in the tropics, Research Dept Technical Memorandum No. 206, ECMWF, Shinfield Park, Reading RG2 9AX, United Kingdom, 1994.

Novelli, P.C., K.A. Masarie, and P.M. Lang, Distributions and recent changes of carbon monoxide in the lower troposphere, *J. Geophys. Res.*, 103(D15):19,015-19,033, 1998.

Novelli, P.C., P.M. Lang, K.A. Masarie, D.F. Hurst, R. Myers, J.W. Elkins, newblock Molecular hydrogen in the troposphere: Global distribution and budget, J. Geophys. Res., 104(D23): 20,427-30,444, 1999.

Olivier, J., J.J.M. Berdowski, J.A.H.W. Peters, J. Bakker, A.J.H. Visschedijk, J.J. Bloos, Applications of EDGAR including a description of EDGAR V3.0, *NRP report 410200 051 / RIVM report 773301 001*, RIVM, Bilthoven, 2000.

Oltmans, S.J., A.S. Lefohn, J.M. Harris, I. Galbally, H.E. Scheel, G. Bodeker, E. Brunke, H. Claude, D. Tarasick, B.J. Johnson, P. Simmonds, D. Shadwick, K. Anlauf, K. Hayden, F.Schmidlin, T. Fujimoto, K. Akagi, C. Meyer, S. Nichol, J. Davies, A. Redondas, and E.Cuevas, Long-term changes in tropospheric ozone, *Atmos. Env.*, 40: 3156-3173, 2006.

Parrish, D.D., D.B. Millet, and A.H. Goldstein, Increasing ozone in marine boundary layer inflow at the west coasts of North America and Europe, *Atmos. Chem. Phys.*, 9:1303-1323, 2009.

Parrish, D.D., K.S. Law, J. Staehelin, R. Derwent, O.R. Cooper, H. Tanimoto, A. Volz-Thomas, S. Gilge, H.-E. Scheel, M. Steinbacher, and E. Chan, Long-term changes in lower tropospheric baseline ozone concentrations at northern mid-latitudes, *Atmos. Chem. Phys.*, 12:11485-11504, 2012.

Parrish, D.D., K.S. Law, J. Staehelin, R. Derwent, O.R. Cooper, H. Tanimoto, A. Volz-Thomas, S. Gilge, H.-E. Scheel, M. Steinbacher, and E. Chan, Lower tropospheric ozone at northern midlatitudes: Changing seasonal cycle, *Geophys. Res. Lett.*, 40:1631-1636, 2013.

Pickering, K.E., Y. Wang, W.-K. Tao, C. Price, and J.-F. Müller, Vertical distributions of lightning NO_x for use in regional and global chemical transport models, *J. Geophysical Research*, 103(D23):31,203-31,216, 1998.

Pozzoli, L., I. Bey, S. Rast, M.G. Schultz, P. Stier, and J. Feichter, Trace gas and aerosol interactions in the fully coupled model of aerosol-chemistry-climate ECHAM5-HAMMOZ, PART I: Model description and insights from the spring 2001 TRACE-P experiment, *J. Geophysical Research*, 113(D07308):doi:10.1029/2007JD009007, 2008.

Pozzoli, L., I. Bey, S. Rast, M.G. Schultz, P. Stier, and J. Feichter, Trace gas and aerosol interactions in the fully coupled model of aerosol-chemistry-climate ECHAM5-HAMMOZ, PART II: Impact of heterogeneous chemistry on the global aerosol distributions, *J. Geophysical Research*, 113(D07309):doi:10.1029/2007JD009008, 2008.

Price, C., and D. Rind, A simple lightning parameterization for calculating global lightning distributions, *J. Geophysical Research*, 97(D9):99219-9933, 1992.

Prinn, R.G., J. Huang, R.F. Weiss, D.M. Cunnold, P.J. Fraser, P.G. Simmonds, A. McCulloch, C. Harth, P. Salameh, S. O'Doherty, R.H.J. Wang, L. Porter, and B.R. Miller, Evidence for Substantial Variations of Atmospheric Hydroxyl Radicals in the Past Two Decades *Science*, 292, 1882-1888, 2001.

Pulles, T., M. van het Bolscher, R. Brand, and A. Visschedijk, Assessment of global emissions from fuel combustion in the final decades of the 20^{th} century. Application of the emission inventory model TEAM, Report 2007-a-r0132/b, Netherlands Organisation for Applied Scientific Research (TNO), 2007.

Rasch, Ph.J., M.C. Barth, J.T. Kiehl, S.E. Schwartz, and C.M. Benkovitz, A description of the global sulfur cycle and its controlling processes in the National Center for Atmospheric Research Community Climate Model, Version 3, *J. Geophysical Research*, 105(D1):1367-1385, 2000.

RETRO-1.6, M. van het Bolscher, T. Pulles, R. Brand, J. Pereira, A. Spessa, S. Dalsoren, T. van Noije, and S. Szopa, Emission data sets and methodologies for estimating emissions, In M. Schultz and S. Rast *RETRO, Work Package 1, Deliverable D1-6*, European Project EVK2-CT-2002-00170 (RETRO), Max Planck Institute for Meteorology, Hamburg, 2007.

Richter, A., and J.P. Burrows, Tropospheric NO_2 from GOME measurements, *Adv. Space Res.*, 29(11):1673-1683, 2002.

Richter, A., J.P. Burrows, H. Nüß, C. Granier, and U. Niemeier, Increase in tropospheric nitrogen dioxide over china observed from space, *Nature*, 437(7055):129-132, 2005.

Roeckner, E., G. Bäuml, L. Bonaventura, R. Brokopf, M. Esch, M. Giorgetta, S. Hagemann, I. Kirchner, L. Kornblueh, E. Manzini, A. Rhodin, U. Schulzweida, and A. Tompkins, The atmospheric general circulation model ECHAM5, part I: Model description, Report 349, Max Planck Institute for Meteorology, Hamburg, 2003.

Roeckner, E., R. Brokopf, M. Esch, M. Giorgetta, S. Hagemann, L. Kornblueh, E. Manzini, U. Schlese, and U. Schulzweida, Sensitivity of simulated climate to horizontal and vertical resolution in the ECHAM5 atmosphere model, *J. of Climate*, pages 3771-3791, 2006.

Roelofs, G.-J., and J. Lelieveld, Model study of the influence of cross-tropopause O_3 transports on tropospheric O_3 levels, *Tellus*, 49B:38-55, 1997.

Schaap M., R.M.A. Timmermans, M. Roemer, G.A.C. Boersen, P.J.H. Builtjes, F.J. Sauter, G.J.M.Velders, J.P. Beck, The LOTOS-EUROS model: description, validation and latest developments, *Int. J. OF Environment & Pollution*, 32(2): 270-290, 2008.

Scheel H.E., H. Areskoug, H. Geiß, B. Gomiscek, K. Granby, L. Haszpra, L. Klasinc, D. Kley, T. Laurila, A. Lindskog, M. Roemer, R. Schmitt, P. Simmonds, S. Solberg, and G. Toupance, On the spatial distribution and seasonal variation of lower-troposphere ozone over Europe, *J. Atmos. Chem.*, 28: 11-28, 1997.

Schmidt, H., G.P. Brasseur, M. Charron, E. Manzini, M.A. Giorgetta, T. Diehl, V.I. Fomichev, D. Kinnison, D. Marsh, and S. Walters, The HAMMONIA chemistry climate model: Sensitivity of the mesopause region to the 11-year solar cycle and CO_2 doubling, *J. of Climate*, 19:3903-3931, 2006.

Schultz, M.G., L. Backman, Y. Balkanski, S. Bjoerndalsaeter, R. Brand, J.P. Burrows, S. Dalsoeren, M. de Vasconcelos, B. Grodtmann, D.A. Hauglustaine, A. Heil, J.J. Hoelzemann, I.S.A. Isaksen, J. Kaurola, W. Knorr, A. Ladstaetter-Weißenmayer, B. Mota, D. Oom, J. Pacyma, D. Panasiuk, J.M.C. Pereira, T. Pulles, J. Pyle, S. Rast, A. Richter, N. Savage, C. Schnadt, M. Schulz, A. Spessa, J. Staehelin, J.K. Sundet, S. Szopa, K. Thonike, M. van het Bolscher, T. van Noije, P. van Velthoven, A.F. Vik, and F. Wittrock, Reanalysis of the tropospheric chemical composition over the past 40 years (RETRO) – a long-term global modeling study of tropospheric chemistry, final project report of EU project EVK2-CT-2002-00170 (RETRO), report no. 48/2007 of "Reports on Earth System Science", Max Planck Institute for Meteorology, Hamburg, Germany, ISSN 1614-1199, 2007.

Schultz, M.G., A. Heil, J.J. Hoelzemann, A. Spessa, K. Thonicke, J. Goldammer, A. Held, J.M.C. Pereira, and M. van het Bolscher, Global wildland fire emissions from 1960 to 2000, *Global Biogeochem. Cycles*, 22(2), doi:10.1029/2007GB003031, 2008.

Schultz, M.G. and V. Thouret (eds.), Second tropospheric ozone workshop, Tropospheric ozone changes: Observations, state of understanding and model performances, GAW Report No. 199, World Meteorological Organization, 2011.

Seinfeld, J.H., and S.N. Pandis, *Atmospheric Chemistry and Physics. From Air Pollution to Climate Change*, John Wiley & Sons, Inc., New York, 1998.

Shindell, D.T., J.L. Grenfell, D. Rind, and V. Grewe, Chemistry-climate interactions in the Goddard Institute for Space Studies general circulation model — 1. Tropospheric chemistry model description and evaluation, *J. Geophysical Research*, 106(D8):8047-8075, 2001.

Shindell, D.T., G.A. Schmidt, R.L. Miller, and D. Rind, Northern Hemisphere winter climate response to greenhouse gas, ozone, solar, and volcanic, *J. Geophysical Research*, 106(D7):7193-7210, 2001.

Shindell, D.T., G. Faluvegi, D.S. Stevenson, M.C. Krol, L.K. Emmons, J.F. Lamarque, G. Petron, F.J. Dentener, K. Ellingsen, M.G. Schultz, O. Wild, M. Amann, C.S. Atherton, D.J. Bergmann, I. Bey, T. Butler, J. Cofala, W.J. Collins, R.G. Derwent, R.M. Doherty, J. Drevet, H.J. Eskes, A.M. Fiore, M. Gauss, D.A. Hauglustaine, L.W. Horowitz, I.S.A. Isaksen, M.G. Lawrence, V. Montanaro, J.F. Müller, G. Pitari, M.J. Prather, J.A. Pyle, S. Rast, J.M. Rodriguez, M.G. Sanderson, N.H. Savage, S.E. Strahan, K. Sudo, S. Szopa, N. Unger, T.P.C. van Noije, and G. Zeng, Multimodel simulations of carbon monoxide: Comparison with observations and projected near-future changes, *J. Geophysical Research*, 111(D19):doi:10.1029/2006JD007100, 2006.

Simmonds, P.G., R.G. Derwent, A.L. Manning, G. Spain, Significant growth in surface ozone at Mace Head, Ireland, 1987-2003, *Atmospheric Environment*, 38:4769-4778, 2004.

Spivakovsky, C.M., J.A. Logan, S.A. Montzka, Y.J. Balkanski, M. Foreman-Fowler, D.B.A. Jones, L.W. Horowitz, A.C. Fusco, C.A.M. Brenninkmeijer, M.J. Prather, S.C. Wofsy, and M.B. McElroy, Three-dimensional climatological distribution of tropospheric OH: Update and evaluation, *J. Geophysical Research*, 105(D7):8931-8980, 2000.

Steil, B., C.Brühl, E. Manzini, P.J. Crutzen, J. Lelieveld, P.J. Rasch, E. Roeckner, and K. Krüger, A new interactive chemistry-climate model: 1. Present-day climatology and interannual variability of the middle atmosphere using the model and 9 years of HALOE/UARS data *J. Geophysical Research*, 108(D9), 4290, doi:10.1029/2002JD002971, 2003.

Stevenson, D.S., F.J. Dentener, M.G. Schultz, K. Ellingsen, T.P.C. van Noije, O. Wild, G. Zeng, M. Amann, C.S. Atherton, N. Bell, D.J. Bergmann, I. Bey, T. Butler, J. Cofala, W.J. Collins, R.G. Derwent, R.M. Doherty, J. Drevet, H.J. Eskes, A.M. Fiore, M. Gauss, D.A. Hauglustaine, L.W. Horowitz, I.S.A. Isaksen, M.C. Krol, J.-F. Lamarque, M.G. Lawrence, V. Montanaro, J.-F. Müller, G. Pitari, M.J. Prather, J.A. Pyle, S. Rast, J.M. Rodriguez, M.G. Sanderson, N.H. Savage, D.T. Shindell, S.E. Strahan, K. Sudo, and S. Szopa, Multimodel ensemble simulations of present-day and near-future tropospheric ozone, *J. Geophysical Research*, 111(D08301), doi:10.1029/2005JD006338, 2006.

Stier, P., J. Feichter, S. Kinne, S. Kloster, E. Vignati, J. Wilson, L. Ganzeveld, I. Tegen, M. Werner, Y. Balkanski, M. Schulz, O. Boucher, A. Minikin, and A. Petzold, The aerosol-climate model ECHAM5-HAM, *Atmos. Chem. Phys.*, 5:1125-1156, 2005.

Thompson, A.M., J.C. Witte, R.D. McPeters, S.J. Oltmans, F.J. Schmidlin, J.A. Logan, M.Fujiwara, V.W.J.H. Kirchhoff, F. Posny, G.J.R. Coetzee, B. Hoegger, S. Kawakami, T. Ogawa, B.J. Johnson, H. Vömel and G. Labow, Southern Hemisphere Additional Ozonesondes (SHADOZ) 1998-2000 tropical ozone climatology 1. Comparison with Total Ozone Mapping Spectrometer (TOMS) and ground-based measurements, *J. Geophys. Res.*, 108(D28238), doi: 10.1029/2001JD000967, 2003.

Thompson, A.M., J.C. Witte, S.J. Oltmans, F.J. Schmidlin, J.A. Logan, M. Fujiwara, V.W.J.H. Kirchhoff, F. Posny, G.J.R. Coetzee, B. Hoegger, S. Kawakami, T. Ogawa, J.P.F. Fortuin, and H.M. Kelder, Southern Hemisphere Additional Ozonesondes (SHADOZ) 1998-2000 tropical ozone climatology 2. Tropospheric variability and the zonal wave-one, *J. Geophys. Res.*, 108 (D28241), doi: 10.1029/2002JD002241, 2003.

Tie, X., G. Brasseur, L. Emmons, L. Horowitz, and D. Kinnison, Effects of aerosols on tropospheric oxidants: A global model study, *J. Geophysical Research*, 106(D19):22,931-22,964, 2001.

Tie, X., L. Emmons, L. Horowitz, G. Brasseur, B. Ridley, E. Atlas, C. Stround, P. Hess, A. Klonecki, S. Madronich, R. Talbot, and J. Dibb, Effect of sulfate aerosol on tropospheric NO_x and ozone budgets: Model simulations and TOPSE evidence, *J. Geophysical Research*, 108(D4):doi:10.1029/2001JD001508, 2003.

Tiedke, M., A comprehensive mass flux scheme for cumulus parameterization in large-scale models, *Monthly Weather Review*, 117:1779-1800, 1989.

Uppala, S.M., P.W. Kållberg, A.J. Simmons, U. Andrae, V. Da Costa Bechtold, M. Fiorino, J.K. Gibson, J. Haseler, A. Hernandez, G.A. Kelly, X. Li, K. Onogi, S. Saarinen, N. Sokka, R.P.Allan, E. Andersson, K. Arpe, M.A. Balmaseda, A.C.M. Beljaars, L. Van de Berg, J. Bidlot, N. Bormann, S. Caires, F. Chevallier, A. Dethof, M. Dragosavac, M. Fisher,

M. Fuentes, S. Hagemann, E. Hólm, B.J. Hoskins, L. Isaksen, P.A.E.M. Janssen, R. Jenne, A.P.McNally, J.-F. Mahfouf, J.-J. Morcrette, N.A. Rayner, R.W. Saunders, P. Simon, A. Sterl, K.E. Trenberth, A. Untch, D. Vasiljevic, P. Viterbo, and J. Woollen, The ERA-40 re-analysis, *Q. J. R. Meteorol. Soc.*, 131:2961-3012, 2005.

van der Werf, G.R., J.T. Randerson, G.J. Collatz, and L.Giglio. Carbon emissions from fires in tropical and subtropical ecosystems, *Global Change Biology*, 9:547-562, 2003.

van der Werf, G.R., J.T. Randerson, L. Giglio, G.J. Collatz, P.S. Kasibhatla, and A.F. Arellano Jr., Interannual variability in global biomass burning emissions from 1997 to 2004, *Atmos. Chem. Phys.*,6:3423-3441, 2006.

van het Bolscher, M., T. Pulles, R. Brand, J. Pereira, B. Mota, A. Spessa, S. Dalsoren, T. van Noije, and S. Szopa, Emission data sets and methodologies for estimating emissions, EU-Contract No. EVK2-CT-2002-00170, Workpackage 1, Deliverable D1-6, Retro — A long-term modelling study of tropospheric chemistry funded under the 5^{th} EU framework programme, 2007.

van Noije, T.P.C., H.J. Eskes, M. van Weele, and P.F.J. van Velthoven, Implications of the enhanced Brewer-Dobson circulation in European Centre for Medium-Range Weather Forecasts reanalysis ERA-40 for the stratosphere exchange of ozone in global chemistry transport models, *J. Geophysical Research*, 109(D19308):doi:10.1029/2004JD004586, 2004.

van Noije, T.P.C., H.J. Eskes, F.J. Dentener, D.S. Stevenson, K. Ellingson, M.G. Schultz, O. Wild, M. Amann, C.S. Atherton, D.J. Bergmann, I. Bey, K.F. Boersma, T. Butler, J. Cofala, J. Drevet, A.M. Fiore, M. Gauss, D.A. Hauglustaine, L.W. Horowitz, I.S.A. Isaksen, M.C. Krol, J.-F. Lamarque, M.G. Lawrence, R.V. Martin, V. Montanaro, J.-F. Müller, G. Pitari, M.J. Prather, J.A. Pyle, A. Richter, J.M. Rodriguez, N.H. Savage, S.E. Strahan, K. Sudo, S. Szopa, and M. van Roozendael, Multi-model ensemble simulations of tropospheric NO_2 compared with GOME retrievals for the year 2000, *ACP*, 6:2943-2979, 2006.

van Noije, T.P.C. , A.J. Segers, and P.F.J. van Velthoven, Time series of the stratosphere-troposphere exchange of ozone simulated with renalyzed and operational forecast data, *J. Geophysical Research*, 111(D03301):doi:10.1029/2005JD006081, 2006.

Wang, Y., D.J. Jacob, and J.A. Logan. Global simulation of tropospheric O_3-NO_x-hydrocarbon chemistry 3. Origin of tropospheric ozone and effects of nonmethane hydrocarbons, *J. Geophysical Research*, 103(D9):10,757-10,767, 1998.

Wang, X., and D.L. Mauzerall, Characterizing distributions of surface ozone and its impact on grain production in China, Japan and South Korea: 1990 and 2020, *Atmospheric Environment*, 38:4383-4402, 2004.

Wesely, M.L., Parametrization of surface resistances to gaseous dry deposition in regional-scale numerical models, *Atmos. Env.*, 23(6):1293-1304, 1989.

Wild, O., M.J. Prather, Global tropospheric ozone modeling: Quantifying errors due to grid resolution *J. Geophys. Res.*, 111(D11305):doi:10.1029/2005JD006605, 2006.

Wild, O., Modelling the global tropospheric ozone budget: exploring the variability in current models Atmos. Chem. Phys., 7(10): 2643-2660, 2007.

Wu, S., L.J. Mickley, D.J. Jacob, J.A. Logan, R.M. Yantosca, D. Rind, Why are there large differences between models in global budgets of tropospheric ozone?, *J. Geophys. Res.*, 112(D05302), doi:10.1029/2006JD007801, (2007).

Yurganov L.N., T. Blumenstock, E.I. Grechko, F. Hase, E.J. Hyer, E.S. Kasischke, M. Koike, Y. Kondo, I. Kramer, F.-Y. Leung, E. Mahieu, J. Mellqvist, J. Notholt, P.C. Novelli, C.P. Rinsland, H.E. Scheel, A. Schulz, A. Strandberg, R. Sussmann, H. Tanimoto, V. Velazco, R. Zander, and Y. Zhao, A quantitative assessment of the 1998 carbon monoxide emission anomaly in the Northern Hemisphere based on total column and surface concentration measurements, *J. Geophys. Res.*, 109(D15305), doi:10.1029/2004JD004559, 2004.

Die gesamten Veröffentlichungen in der Publikationsreihe des MPI-M
„Berichte zur Erdsystemforschung“,
„Reports on Earth System Science“,
ISSN 1614-1199

sind über die Internetseiten des Max-Planck-Instituts für Meteorologie erhältlich:

http://www.mpimet.mpg.de/wissenschaft/publikationen.html



ISSN 1614-1199